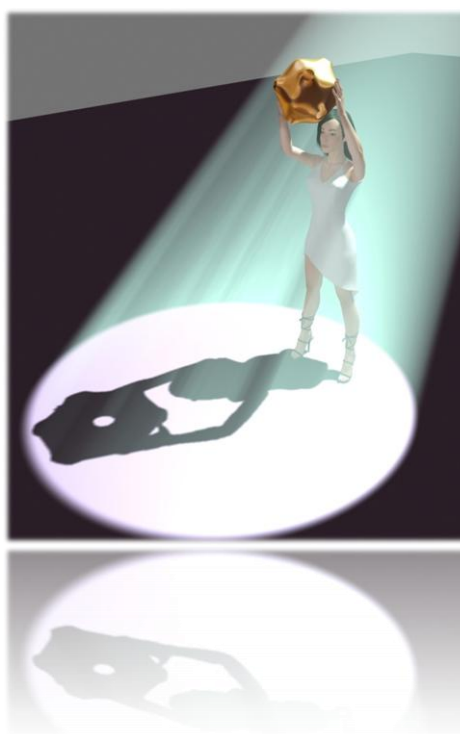

Electronic structure of bulk and low dimensional systems analyzed by Angle-Resolved Photoemission Spectroscopy



Memoria presentada por
Victor Joco
para optar al grado de
Doctor en Ciencias Físicas
Departamento de Física de la Materia Condensada
Universidad Autónoma de Madrid

Tesis dirigida por:
Enrique García Michel
Octubre de 2007

Contents

Resumen	3
1. Introduction	7
2. Angle Resolved Ultra-Violet Photoelectron Spectroscopy	11
2.1. The basic ARUPS experiment	12
2.2. Electronic states in solids.....	16
2.3. Free electron model	17
2.4. Nearly free electron model. Three step photoemission process.	18
2.5. System dimensionality and ARUPS	20
2.5.1. Zero dimension	20
2.5.2. One dimensional systems	23
2.5.3. Two dimensional systems.....	26
2.5.4. Three dimensional electronic systems	28
2.6. ARUPS experimental setups and sample preparation	30
3. Extension of a Tight Binding Model	33
3.1. Slater Koster tight binding method	34
3.2. Computer analytical solutions of the Slater Koster Hamiltonian matrix elements.....	37
3.3. Constant energy surfaces	39
3.4. Marching Cubes and Advanced Marching Cubes algorithm	40
3.5. The radial projected surface method.....	45
3.6. Spherical cuts of constant energy surfaces	47
3.7. Theoretical band dispersion	50
3.8. Projected band gaps	54
3.9. Initial and final state width effects.....	57
3.10. Implementation.....	58
3.11. Results, discussion, experimental proof and conclusions	60
4. Phase transitions and surface electronic structure of Pb/Cu(100).....	69
4.1. Surface phase transitions of Pb/Cu(100) system	71
4.2. Projected band gaps of the Cu(100) surface	76
4.3. Filling of a surface electronic band.....	78
4.4. Electronic structure of the c(4×4) phase. Surface states and/or surface Umklapps.....	83

4.5. Electronic structure of the $c(5\sqrt{2}\times\sqrt{2})R45^\circ$, $c(2\times 2)$ and split $c(2\times 2)$ phases and the role of the electronic structure in the $c(5\sqrt{2}\times\sqrt{2})R45^\circ$ to split $c(2\times 2)$ phase transition	90
4.6. Conclusions.....	95
5. Electronic structure of clean and halogenated Pt(110) surface.....	97
5.1. Electronic structure of the clean Pt(110) surface	99
5.2. The electronic structure of platinum. Calculated electronic structure.	100
5.2.1. Fermi surfaces and band dispersion of Pt(110)	104
5.2.2. Surface states of Pt(110)- (1×2) surface	108
5.3. Electronic structure of Br/Pt(110) system	116
5.4. Conclusions.....	120
Conclusiones generales.....	121
Bibliography.....	123

Resumen

La estructura electrónica de los materiales desempeña un papel muy importante en la ciencia de superficies. Por otra parte, una información clara sobre las propiedades electrónicas de un sustrato es fundamental a la hora de analizar y entender la estructura electrónica de su superficie. Los primeros cálculos cuantitativos de los estados electrónicos en sólidos cristalinos fueron realizados por Wigner y Seitz en 1930, y desde entonces se ha realizado una gran cantidad de trabajo que ha resultado en un desarrollo importante en ese campo, proporcionando una descripción precisa sobre la estructura electrónica de los sólidos. La fotoemisión resuelta en ángulo ha experimentado un gran avance instrumental en los últimos años. Se trata de un método que proporciona una relación casi directa entre el experimento y la estructura electrónica de bandas. Uno de los objetivos que se plantearon fue extender e implementar un método teórico de cálculo de la estructura electrónica que permitiera entender y analizar los datos obtenidos con la técnica de la fotoemisión resuelta en ángulo de manera rápida, incluso simultánea con los experimentos. El modelo teórico de tipo “tight binding” proporciona las soluciones de la estructura electrónica de una manera rápida con una precisión que se adapta a los datos experimentales de la fotoemisión resuelta en ángulo. Es uno de los modelos más sencillos y rápidos de cálculo de estructura electrónica, pero incluso así, este método está sólo al alcance de los investigadores teóricos.

Se han investigado las propiedades de dos superficies de metales nobles que presentan efectos de baja dimensionalidad. En primer lugar, la superficie de Cu(100) presenta algunas regiones del espacio recíproco donde no existen bandas de volumen, lo que le confiere en esas regiones un carácter similar al de un semiconductor. Estas regiones corresponden a las zonas prohibidas (gaps) del cristal, y por razones de simetría pueden contener estados de superficie. La presencia de adsorbatos en la superficie de Cu(100) da lugar a la formación de superestructuras, cuya estabilización

puede tener varios orígenes. Los estados de superficie que aparecen y su comportamiento en función del recubrimiento y temperatura se pueden explicar en general teniendo en cuenta la estructura electrónica del sustrato y del adsorbato. En el caso del sistema Pb/Cu(001), la gran diferencia que existe entre los parámetros de red de Pb y Cu hace que aparezcan una amplia gama de superestructuras. Varias reconstrucciones experimentan transiciones de fase cuyos orígenes se pueden interpretar analizando sus estructuras electrónicas, ya que el balance entre las diferentes formas de energía en un sistema puede favorecer una estructura frente a otra. Así, en algunos casos cabe esperar la aparición de estructuras “forzadas” teniendo en cuenta su energía elástica, pero que se ven favorecidas por un decremento en la energía electrónica.

Otra cuestión de interés que se ha planteado es de qué modo una gran anisotropía estructural en la superficie afecta a las propiedades electrónicas. La superficie de Pt(110) ha servido como sistema modelo cuya estructura electrónica se ha intentado comprender. También se han investigado los efectos de depositar un halógeno en esta superficie, teniendo en cuenta las hipótesis existentes que relacionan la estructura cristalina de la superficie con la estructura electrónica. El objetivo ha sido una investigación cuidadosa de los datos de fotoemisión resuelta en ángulo para esta superficie con el fin de confirmar o descartar estas ideas.

La tesis contiene dos partes principales. La primera parte explica la implementación y la extensión que se ha hecho de un modelo teórico de cálculo de estructura electrónica. La segunda parte consiste en el estudio experimental de dos sistemas de superficie. La herramienta teórica descrita en la primera parte ha sido de gran importancia para realizar y entender el trabajo experimental. El método de “tight binding” se ha implementado de una manera muy cuidada, orientándose desde el principio a transformar su implementación en una herramienta útil para los investigadores experimentales. En la implementación, se ha hecho uso de una potente herramienta para cálculos simbólicos (Wolfram Mathematica) y se han tenido en cuenta optimizaciones basadas en simetría. También se ha hecho uso de librerías rápidas, específicas de los procesadores que se han utilizado.

En el estudio experimental de sistemas Pb/Cu(100), Pt(110) y Br/Pt(110) se ha intentado entender la estructura electrónica obtenida mediante fotoemisión resuelta en ángulo y asimismo se ha analizado la importancia de la estructura electrónica en la

formación de las superestructuras observadas. En la técnica de fotoemisión resuelta en ángulo, la muestra se introduce en un sistema de ultra alto vacío, y la estructura electrónica se obtiene de una forma casi directa mediante el análisis de la distribución energética de los electrones fotoemitidos usando un analizador de electrones. La fotoemisión se lleva a cabo iluminando la muestra con radiación ultravioleta obtenida de una lámpara de He o en una instalación de radiación sincrotrón, en la que es posible obtener mejores resultados debido al alto flujo de fotones y su mayor rango de energía, que permite seleccionar el valor de la energía del fotón.

**CHAPTER
ONE**

1. Introduction

The purpose of this research was to investigate the electronic structure of bulk and low dimensional materials by means of angle resolved photoemission spectroscopy. The class of low dimensional materials refers to systems whose structure or some properties extend to less than three dimensions. Besides the fundamental significance of understanding the properties of these materials, a clear comprehension of their physical properties may lead to a deeper insight for potential applications. The information provided by the electronic structure of a physical system is crucial to understand its behaviour and any process taking place in the system.

Since the theoretical work of Peierls, who showed that the structure of a metallic linear chain would lose its stability in 1D, low dimensional metals have attracted a great interest. The basic assumption in solid state physics saying that the periodicity of the crystal lattice determines the electronic structure was reformulated; the electronic structure also can reshape the crystal periodicity. In systems showing Peierls distortions, a loss of stability due to an increase of elastic energy is compensated by a decrease of the electronic energy. Typically, these systems show a temperature dependence phase transition separating the non-distorted state at high temperatures from the modulated phase at low temperatures.

Low dimensional systems are not only theoretical abstractions. With the development of surface science, it became practically possible to develop structures of confined dimensionality. The progress of surface science is strongly correlated with the advances done in the field of Ultra High Vacuum (UHV) techniques. Extremely low pressures are required to keep the surfaces clean during preparation and measurements.

A valuable tool which gives information about the occupied electronic structure of materials is photoemission spectroscopy (PES). The principle of PES is the photoelectric effect, where an electron occupying a certain energy level in an atom,

molecule or solid is emitted after the absorption of a photon of appropriate energy. In angular resolved PES, the momentum resolved energy distribution of the photoemitted electrons is measured. Following simple assumptions as energy and momentum conservation of the emitted electrons, the initial band structure of the solid can be rebuilt from an ARUPS experiment. The major technical requisites required to perform an ARUPS experiment are based in the development of high intensity ultraviolet tunable light sources together with high-resolution and sensitivity angle resolved electrostatic electron analyzers. A part of this thesis was devoted to the study of the electronic structure of several surface systems, as an effort to understand the role of the electronic energy in stabilizing surface structures.

Clear information about the electronic properties of the crystal substrate is crucial for predicting and analyzing the surface electronic structure. The first quantitative calculation of electronic states in crystalline solids is related with the work of Wigner and Seitz in 1930. A rich work followed after, resulting in the development of a lot of methods providing a precise description of the solid electronic structure. From the surface science experimentalist point of view, the theoretical results are a great help for predicting and explaining electronic properties of surfaces. But like in other cases, theoretical calculations adhere to standards of developing more and more precise models, while giving little weight to experiments. A part of this work was devoted to build a tool that directly connects theoretical calculations of band structures with the typical observations of an ARUPS experiment. With a tool like this, a fast comparison of theoretical result with the experiment is becoming possible. A computer code has been written, generating also complementary plots of great aid in understanding, predicting and guiding a work dealing with electronic structure features.

The work presented in this thesis is enclosed in the frame of the points outlined above. It is organized in four main sections:

- **Angle Resolved Ultra-violet Photoelectron Spectroscopy (ARUPS).** The photoemission process is the fundamental phenomenon used in this work. The second chapter is dedicated to a survey of theoretical and experimental aspects of photoemission spectroscopy, in particular to ARUPS, a direct tool in obtaining the occupied electronic structure from the valence band of a solid and its surfaces.
- **Extension of a tight binding model.** A tight binding model provides the electronic energy solutions of a crystal for a given momentum

value. The parameters involved in tight binding approximation (TBA) models are adjustable constants obtained by fitting results of more complicated electronic structure calculations (e.g. first-principles). The precision obtained is of comparable accuracy with the fitted model, but orders of magnitude faster. The third chapter deals with the description of an interface used to provide a simple and intuitive connection between a TBA model of a 3D crystal and the ARUPS data. Beside this, several types of plots can be obtained in order to guide and analyze an ARUPS experiment. The face centered cubic structure has served as an illustrating example and it has received special considerations, since the substrates used in this thesis belong to this structure.

- **Phase transitions and electronic structure of Pb/Cu(100).**

Surface phase transitions in ultrathin films provide insight in the physical phenomena typical of low dimensional materials. The large lattice mismatch of Pb and Cu is responsible for a large number of superstructures, undergoing several phase transitions. The novel electronic properties of this system are described in the fifth chapter. The measured and calculated band structure and the Fermi surfaces are analyzed and discussed.

- **Electronic structure of Pt(110) and Br/Pt(110).** The (110) face of a Pt crystal is a good model system to investigate and understand electronic effects related to a structural anisotropy. It is also a good candidate for obtaining low dimensional surface structures by depositing an adsorbate. The structure of halogens adsorbed on Pt(110) exhibits a rich behaviour, with several surface reconstructions, depending on coverage and temperature. As first step, a detailed analysis of the clean Pt(110) surface makes possible a detailed comparison with theoretical calculations and also to establish the surface vs. bulk nature of the bands found. On the other hand, it has been proposed that the quasi-1D character of the Br/Pt(110)-(3×1) surface gives rise to the stabilization of a Surface Charge Density Wave (SCDW) from the Br/Pt(110)-c(2×2) phase. However, the role of the SCDW in the origin and the nature of the transition is unclear. The third chapter brings a new insight on the origin of these phases after a full characterization of their electronic band structure with ARPES and by comparison with the Pt(110)-(1×2) results. Special attention is focused in the region close to the Fermi level where effects related with surface stability and SCDW are observed.

**CHAPTER
TWO**

2. Angle Resolved Ultra-Violet Photoelectron Spectroscopy

Photoemission spectroscopy (PES) is a fundamental technique in the study of the electronic structure of atoms, molecules or solids. It is based on the photoelectric effect, a quantum phenomenon in which electrons are emitted from matter after the absorption of a quantum of energy from electromagnetic radiation. A historical development of PES as a general technique has received an ample attention in a recent review (1), therefore it is omitted and special consideration is given to the particular case of Angle Resolved Ultra-Violet Photoelectron Spectroscopy (ARUPS) as it is the main technique used in this thesis.

ARUPS represents a particular case of photoemission spectroscopy. The distinctive features of ARUPS come from the requirement of angular resolving power for the electron analyzer and a highly monochromatic ultra-violet (UV) radiation as excitation source. The need of angular resolving power is due to the relationship between the direction of the photoemitted electrons and their initial momentum inside the crystal. The choice of ultraviolet radiation with photon energy in range of approximated 5 to 100 eV is related with several facts. First of all, the photon energy should be larger than the work function of the material, normally having a value around 5 eV. Second, increasing the photon energy is resulting in a decrease of the angular and energetic resolution of the technique. Moreover, photon energies higher than 100 eV are not typical for the technique since most of the features related with the valence band structure can be solved in the mentioned range.

ARUPS is a direct experimental tool for probing the momentum resolved electronic structure of many kinds of materials and their surfaces. Examples are metals (2), semiconductors (3), ordered alloys (3), superconductors (4) (5) and magnetic materials (6). In this chapter, a short description of the electronic structure in solids and ARUPS as technique is presented.

2.1. The basic ARUPS experiment

In order to study the electronic bandstructure of a solid, good resolution in reciprocal space and in energy is required. Both can be realized by using UV photons for the photoelectron emission (1).

The most important expression applying to all solid state photoemission spectroscopies is given by the energy conservation rule:

$$E_{kin} = h\nu - |E_B| - \Phi. \quad (2.1)$$

The energy E_{kin} of the photoemitted electron is given by the photon energy less the material work function Φ required for the electron to escape in the vacuum and the initial binding energy E_B of the electron inside the material.

In an Angle-Resolved UPS (ARUPS) experiment one measures the kinetic energy E_{kin} of an electron for a given polar angle θ_{ext} with respect to the surface normal and an azimuthal angle ϕ_{ext} . A schematic setup is shown in Figure 2.1.

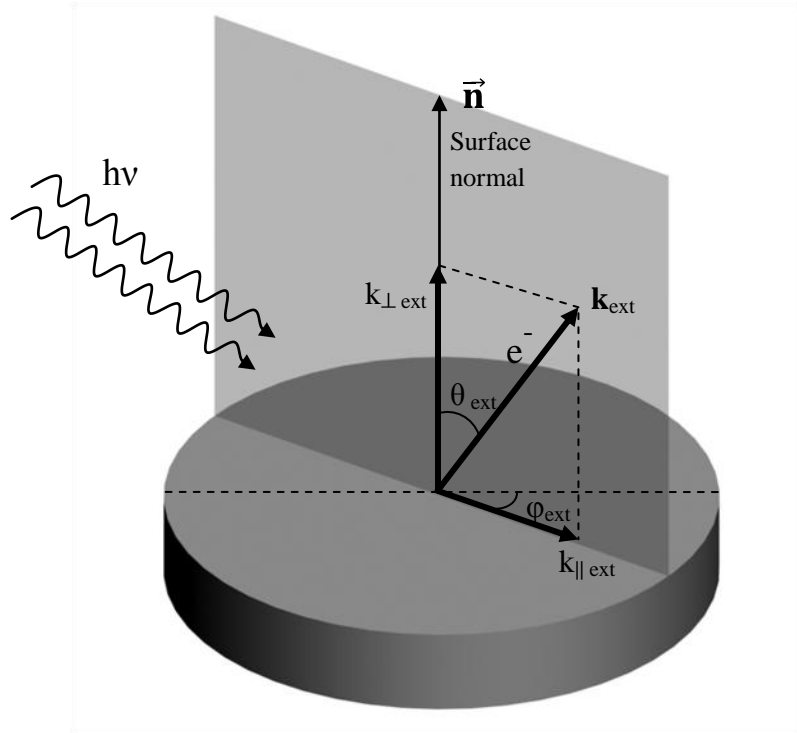


Figure 2.1 Schematic setup for angle resolved photoelectron detection.

For a basic understanding on how the initial state $E_i(k_i)$ can be determined with the measured quantities θ_{ext} and ϕ_{ext} the following relations are required. Assuming free

electron final states both in solid after the photon absorption and in the vacuum, one has:

$$E_f(\mathbf{k}_f) = \frac{\hbar^2}{2m} \mathbf{k}_f^2 \quad E_{kin}^{vac} = \frac{\hbar^2}{2m} \mathbf{k}_{vac}^2 \quad (2.2)$$

where E_f and \mathbf{k}_f describe the final state in the solid to which the electron has been excited by a photon of energy $h\nu$. Energy and momentum conservation rules lead to the following expressions:

$$\begin{aligned} E_f(\mathbf{k}_f) &= E_i(\mathbf{k}_i) + h\nu \\ \mathbf{k}_f &= \mathbf{k}_i + \mathbf{k}_{h\nu} + \mathbf{G} \end{aligned} \quad (2.3)$$

The photon momentum in the ultraviolet range ($\mathbf{k}_{h\nu}$) can be neglected compared with the electron momentum of similar energy. \mathbf{G} is a reciprocal lattice vector which is also influencing the electron emission into the vacuum.

The emission into the vacuum is affected by a potential energy step at the surface barrier which originates from the Coulomb and exchange interactions in the solid that can be modelled as a mean attractive potential V_0 (the inner potential) giving rise to a force perpendicular to the surface. It is not influencing the parallel component of the initial momentum which can be calculated as (7):

$$k_{||} = \sqrt{(2m/\hbar^2)} \sqrt{h\nu - \Phi - E_B} \sin(\theta_{ext}) \quad (2.4)$$

The determination of the perpendicular value of the initial momentum requires the knowledge of the inner potential, assuming a free-electron like final states and a step-like surface barrier it is given by:

$$k_{\perp} = \sqrt{(2m/\hbar^2)} \sqrt{h\nu - \Phi - E_B + V_0} \cos(\theta) \quad (2.5)$$

where θ refers to the polar angle in the solid. The relation between the electron propagation inside and outside the solid is given by:

$$\sin(\theta) = \frac{\sqrt{h\nu - \Phi - E_B}}{\sqrt{h\nu - \Phi - E_B + V_0}} \sin(\theta_{ext}) \quad (2.6)$$

In the most basic ARUPS experiment, one measures a single spectrum of the intensity of the photoemitted current versus the electron kinetic energy at a single fixed direction and a single fixed photon energy. This spectrum is usually called Energy Distribution Curve (EDC), and it is illustrated in Figure 2.2.

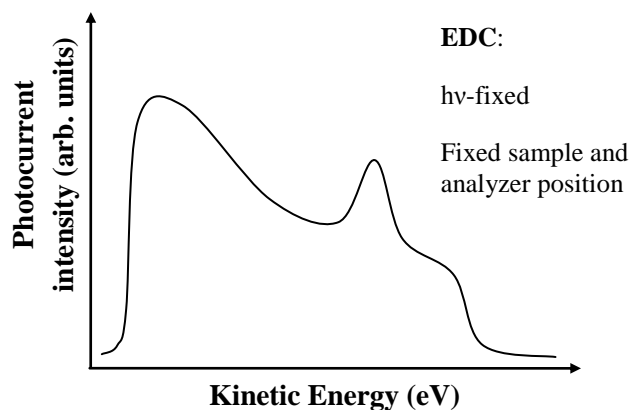


Figure 2.2 An EDC consists in a plot of the photocurrent intensity versus the photoelectron kinetic energy at a fixed sample and analyzer position and at a fixed photon energy.

Multiple EDCs can be acquired at different angles between the sample surface normal and the analyzer position. Joining several EDCs along a specific direction gives rise to a band dispersion plot along that specific direction, which can be referred to the corresponding sample crystallographic directions. This situation is illustrated in Figure 2.3. There are two possibilities to display the data. A waterfall like plot as shown in the left side of Figure 2.3 has each EDC intensity shifted a specific amount in order to separate the spectra from each other. The second way of displaying the data makes use of a color scale to display the photoelectron intensity, as shown in the right side of Figure 2.3.

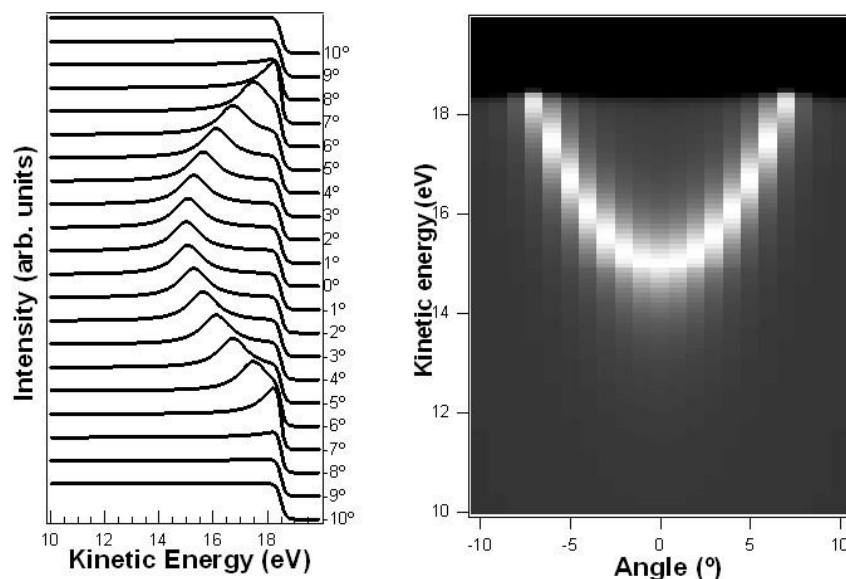


Figure 2.3 Left: waterfall plot made by joining shifted EDCs measured at different angles. Right: Color scale representation of EDCs intensity, the abscissa is the measured angle in degrees while the ordinate is the photoelectron kinetic energy in eV.

The abscissa of a grayscale plot from Figure 2.3 can be translated in a k parallel direction making use of the expression 2.4.

Other useful measurements that can be performed are constant energy mappings obtained by recording the angular (hence k_{\parallel}) distribution of the photoemitted electrons from a small energy window centered at a certain binding energy value. A particular case of interest is the Fermi surface mapping which corresponds to zero binding energy. In the left side of Figure 2.4 it is shown how points of emission angle (θ_{ext} and ϕ_{ext}) can be chosen in order to obtain a Fermi surface mapping. The right side of Figure 2.4 shows a grayscale linear plot of the Fermi surface mapping translated in k_{\parallel} components (k_x and k_y) for a Cu(111) surface measured with a photon energy $h\nu=21.2$ eV.

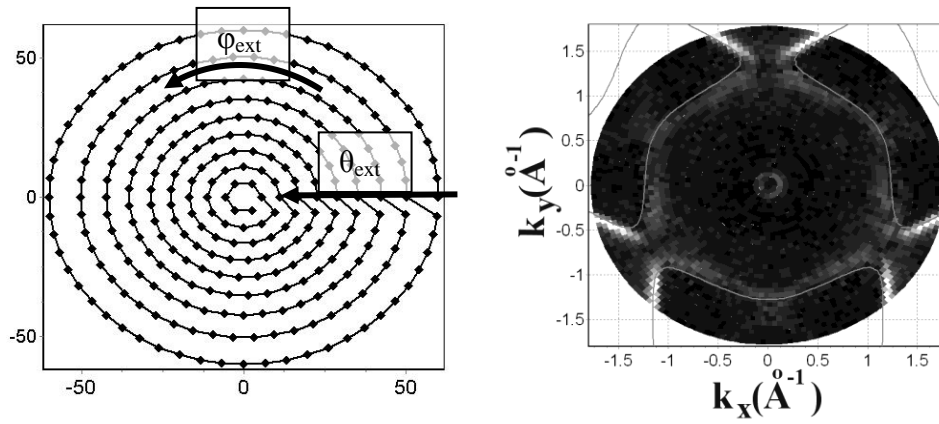


Figure 2.4 Left: arbitrary chosen points (θ_{ext} and ϕ_{ext}) for recording a constant energy. Right: Fermi surface mapping of Cu(111) surface measured with a photon energy $h\nu=21.2$ eV. Lines on top of the experimental data are the theoretical cuts for the given surface and photon energy.

2.2. Electronic states in solids

The electronic structure is one of the most important properties of a solid, as it determines such important features, as electrical or thermal conductivity and magnetic ordering, among others.

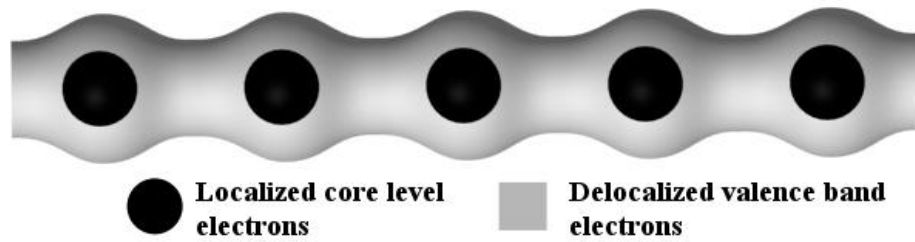


Figure 2.5 Illustration of electronic state localization for a 1D metallic chain.

The electronic states in bound solids can be classified in two main groups. The first category corresponds to electronic states which are spatially localized close to the nucleus of the atoms forming the solid. The electronic states occupied by these electrons are called “core levels”. These electrons are tightly bound to the nucleus. The binding energies of the core level electrons are in the range of 10^1 - 10^4 eV. The second category includes the electronic states of the shared electrons participating in covalent or metallic bonds. The electronic states of these electrons receive the name of “valence band”. The binding energies of the valence band electrons are much lower, typically less than 10 eV.

From the spatial point of view, an important difference between the core level states and the valence band states is the degree of localization, as exemplified for a 1D metallic chain in Figure 2.5. An electron in a core level state is a bound electron, strongly localized near the nuclei core. In contrast, the electrons from the valence band do not belong to single atoms, they form a large delocalized electron gas. In consequence, the description of these two kind of electronic states is different. For the core level electrons, due to their localization, a momentum dependent description is unnecessary. The energy of the valence band states depends on the momentum of the electron occupying that state, and thus the valence band states can only be described using an energy-momentum dispersion relationship.

2.3. Free electron model

The simplest model to describe the behaviour of valence electrons in a solid is given by the free electron gas model (8). It is based on the assumption that the valence electrons are completely detached from their ions ("electron gas") and as in an ideal gas, electron-electron interactions are completely neglected. Inside the solid the electrons are moving in a constant zero potential, while outside the solid the potential is infinite.

These assumptions are leading to a simple well known parabolic dispersion relationship between an electron energy E and its momentum \mathbf{k} (8) given by:

$$E = \frac{\hbar^2 \mathbf{k}^2}{2m_e} \quad (2.7)$$

where \hbar represents the reduced Planck's constant and m_e is the electron mass.

The dispersion relationship of the free electron gas provides only an intuitive description of the valence band electrons. Moreover, it can not even give a qualitative description of the photoemission phenomena, due to the impossibility of optical absorption of such a system.

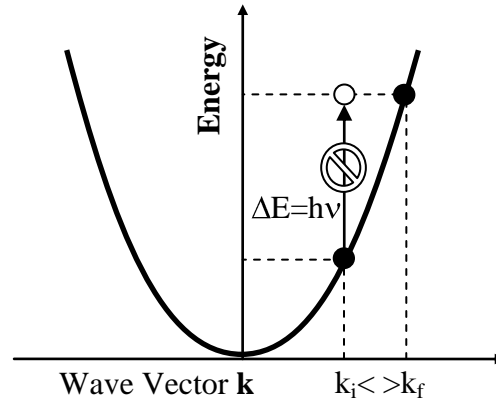


Figure 2.6 Forbidden vertical transitions of the free electron gas.

The photon momentum in the ultra-violet range can be neglected compared with the electron momentum. Then, the momentum conservation rule demands that the electron momentum in the final state k_f after photon absorption to be equal with the initial momentum k_i before absorption. As illustrated in Figure 2.6, this situation would lead to a final state not lying on the distribution curve. Concluding, no photon absorption is possible for free electrons, since a gain in energy $\Delta E = \hbar v$ would lead to a non existing final state. In other words, vertical transitions are forbidden for the free electron gas and without an optical absorption, the photoemission process is resulting impossible.

2.4. Nearly free electron model. Three step photoemission process.

A more realistic model describing the delocalized electron gas in a solid is the nearly free electron gas (8), a modification of the free electron gas model, which includes a weak periodic potential perturbation meant to model the interaction between the conduction electrons and the ions in a crystal. Introducing this weak perturbation has important effects on the solution of the dispersion relationship, most significantly consisting in its degeneracy. For a single value of momentum, several values of energies are possible. Another important effect is the appearance of forbidden zones of energy solutions, also called band gaps.

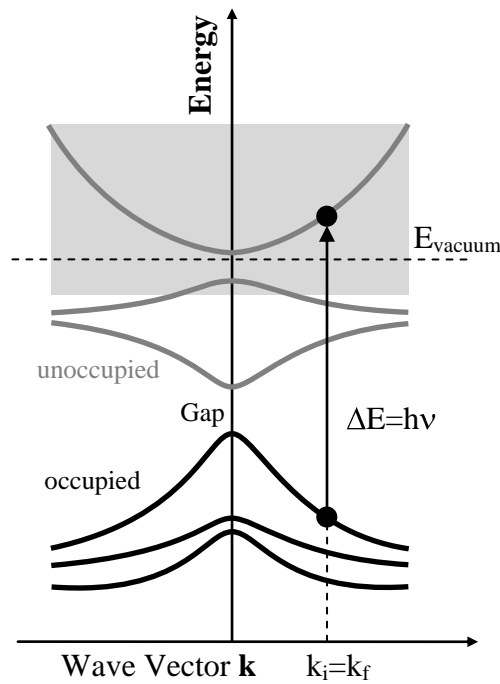


Figure 2.7 Allowed vertical transitions of the nearly free electron gas.

Optical transitions are possible since more than one energy state with the same momentum exists, thus photon absorption is made possible by taking into account the crystal lattice effects on the electron gas. The photon absorption results in the expulsion of an electron from an occupied initial state and placing it into a final unoccupied state (Figure 2.7). If the energy of the final state is bigger than the energy needed to bring a free electron into vacuum, the excited electron can be emitted from the crystal. The first requirement of the photoemission process is accomplished.

A simple and intuitive time scale description of the photoemission phenomena has received the name of “three step model” (9). In this model the photoemission event is separated in three independent steps: optical excitation between the initial and the final energy states, travel of the excited electron to the surface and the transmission of the electron through the surface barrier into the vacuum. The first step of this model contains information about the intrinsic electronic structure of the material. The primary assumption done, called the sudden approximation, is that an electron removal from the N electrons system is so fast, that the remaining $N-1$ electrons are not contributing with any further interaction to the process. To rebuild the electronic structure, information about the final state is required. A great simplifying case is occurring if the final state is assumed to be a free electron final state (FEFS). Since the energy of the final state is given by a free electron dispersion, the initial band structure is deduced in a relatively easy way from the angle resolved kinetic energy distributions, knowing the value of the inner potential (V_0). A large number of experimental results (10) indicate that the FEFS model can be applied for a range of photon energies extending from work function value to hundreds of eV.

2.5. System dimensionality and ARUPS

ARUPS was originally used for investigating the electronic structure of three dimensional solids (1). In practice, all solids extend in three dimensions, but their electronic structure can be referred to some extent in less than three dimensions. In the following subchapters, each particular case of dimensionality is going to be analysed in the prism of the electronic structure and angle resolved photoemission properties.

2.5.1. Zero dimension

A zero dimension (0D) electronic system contains bounded electrons of certain energy E_B confined in all the three dimensions of the real space in a region of width comparable with the electron wavelength. The average momentum of an electron from a 0D system has to be zero in order to lead to a spatial localization, as shown in Figure 2.8. The surface on which the system is lying is drawn for illustrating the real space directions. It helps for choosing k_{\parallel} directions in an imaginary ARUPS experiment.

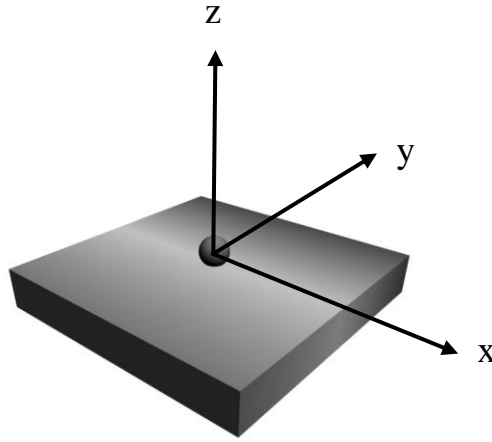


Figure 2.8 Zero dimensional situation of an electron system localization in the real space. The small sphere represents a possible localization of the electron wave function.

The mathematical expression giving the zero average momentum can be written as:

$$\int_{t=0}^T \mathbf{k} dt = 0 \quad (2.8)$$

where the integral over time t should give zero in a integration interval to a relatively small time T .

In a generalized case of a 0D system, the temporal dependence of the momentum is unknown. This situation leads to a delocalization of the electron momentum in the k -space. Any point in the k -space can be occupied, as illustrated with grey dots in Figure 2.9.

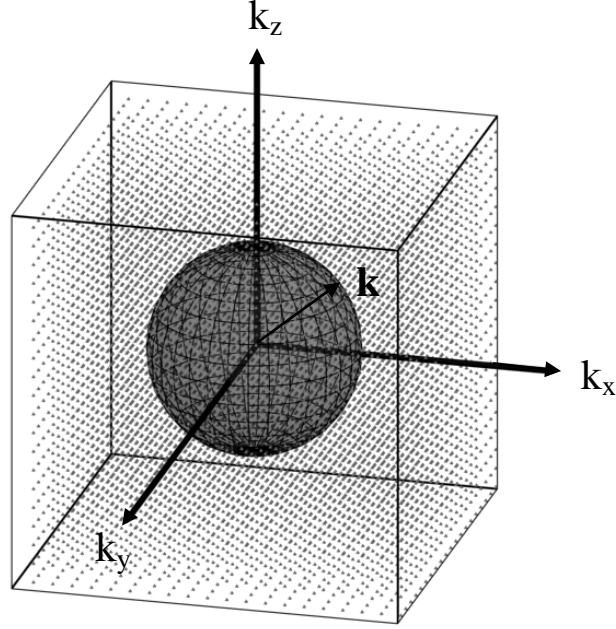


Figure 2.9 Electron delocalization in the k -space represented with grey dots. The wireframe gray sphere represents a free electron final state of momentum \mathbf{k} .

The cube in Figure 2.9 has only the illustrative value of showing the extension in three dimensions of the electron delocalization in the k -space.

From the mathematical point of view, the delocalization comes from the fact that the electron energy is not dependent on the \mathbf{k} value:

$$E(\mathbf{k}) = E_B \quad (2.9)$$

The energy conservation in a possible photoemission process demands that the energy of the final state is:

$$E_f = E_B + h\nu \quad (2.10)$$

where E_f is the electron energy in the final state after the absorption of a photon of energy $h\nu$.

If the final state of the electron after the photon absorption is an unbounded state, the simplest approximation would be to consider it free electron like. Even if this approximation is not the most exact one for the real situation, it is leading to correct conclusions from the photoemission point of view.

A free electron like final state has the energy momentum relationship:

$$E_f = \frac{\hbar^2}{2m} \mathbf{k}_f^2 = \frac{\hbar^2}{2m} (k_{fx}^2 + k_{fy}^2 + k_{fz}^2) \quad (2.11)$$

According with the expression 2.11, a constant energy surface of the free electron state can be represented in the k-space as a sphere with the radius:

$$k = \sqrt{\frac{2m}{\hbar^2} E_f} \quad (2.12)$$

The momentum conservation rule demands that from the delocalized initial electrons filling all the k-space, only the ones with the same values of the final state can participate in the photon absorption process. Geometrically, the momentum conservation rule can be seen as the intersection of the full k-space momentum of the initial electrons with a sphere determined by the final state momentum. Evidently, the result of this intersection is the sphere.

The energy conservation rule sets the radius \mathbf{k} of this sphere, since the final energy is given by the expression 2.10.

$$\mathbf{k} = \sqrt{\frac{2m}{\hbar^2} (E_B + h\nu)} \quad (2.13)$$

The sphere of radius k was represented in Figure 2.9 with grey color in a wireframe manner.

The question that arises is how the band structure of a 0D system would look like in an ARUPS experiment. In a typically $E(k_{\parallel})$ ARUPS experiment, one expects that the binding energy of the state to be at the same level as represented in Figure 2.10 with the dotted bold line. The definition of k_{\parallel} for a 0D system is quite ambiguous since the system extends in less than 2 dimensions. Choosing the reference system like Figure 2.9, Figure 2.10 shows the possibility of optical transitions in a 0D system choosing for example k_x as k_{\parallel} direction and measuring in a k_{xz} plane. An optical transition from the initial delocalized momentum state of energy E_B is requiring a final unoccupied state of same momentum but with an energy $E_B + h\nu$. When performing an ARUPS experiment, one plots usually the binding energy of the state versus the k parallel value, ignoring the perpendicular value, which is unknown unless an approximation is being done, as described in Chapter 2.1. Choosing a free electron like final state, one can observe in Figure 2.10 that unoccupied states of same momentum from the dot plotted circle correspond to a final state covering all the line in k parallel value.

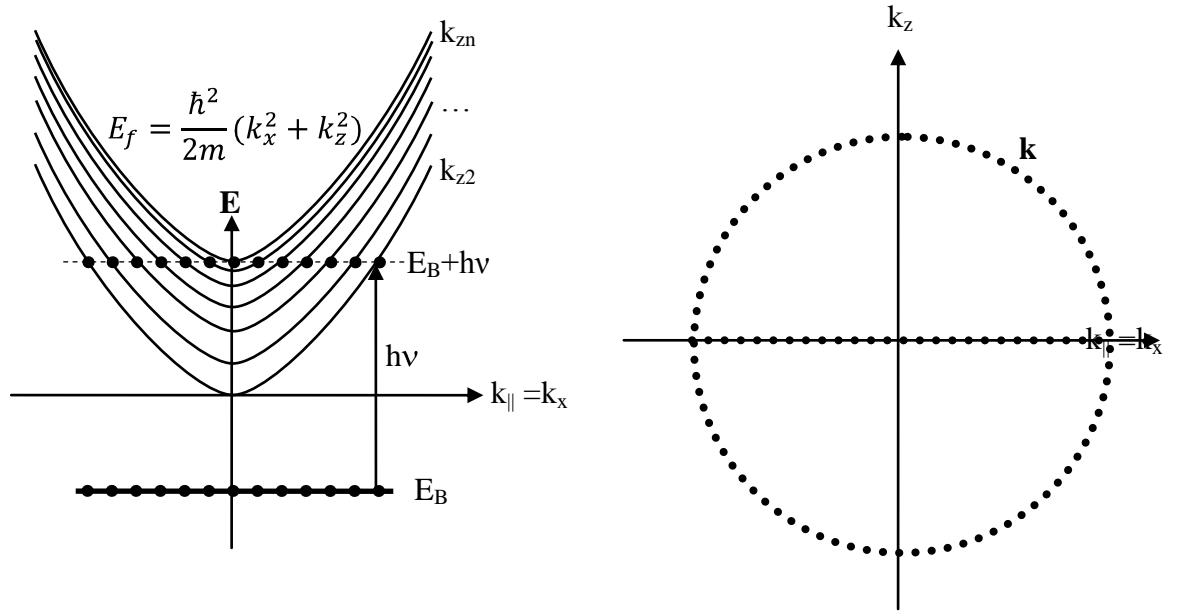


Figure 2.10 Optical transitions in a 0D system, choosing k_x as k_{\parallel} direction and measuring in a k_{xz} plane.

To each initial state from the line at an energy E_B vs k_{\parallel} , an occupied state exists at an energy $E_B + h\nu$, but at different values of k_z and in the photoemission spectra the state appears at the same binding energy independently of spatial direction of the measurement. In other words, the energy of the level is independent of the momentum, which is not a good quantum number, and it behaves like an atomic-like level.

2.5.2. One dimensional systems

In the range of increasing dimensionality, the case of one dimensional systems is the first one where the dispersion is required to describe the system. A 1D electronic system contains electrons confined along a line or contour of width comparable with the electron wavelength. The spatial localization is illustrated in Figure 2.11. The reference system has been chosen taking into account a possible surface of a truncated crystal. The electrons are arbitrarily chosen to move free along the x direction and confined along the y and z direction. In order to discuss about this system, a free electron behaviour along the x axis is going to be taken in account. Anyway, a bounded state in a crystal requires the dispersion relationship to be shifted to lower energies so that the electron is not escaping into the vacuum. The amount of this shifting compared to a completely free electron state is arbitrarily chosen as E_B .

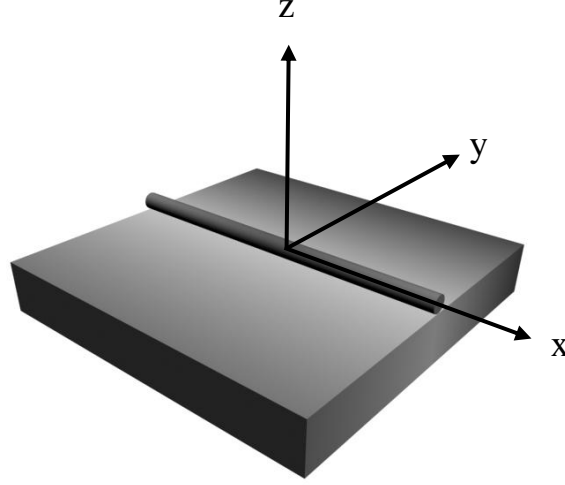


Figure 2.11 Illustration of a one dimensional electronic system in the real space. The small cylinder shows the electron confinement along the arbitrarily chosen x axis.

The dispersion relationship can be written as:

$$E = E(\mathbf{k}) = E_B + \frac{\hbar^2}{2m} k_x^2 \quad (2.14)$$

A consequence of the expression 2.14 is a constrain of the electron delocalization in the momentum space. The possible values of the momentum are independent of k_z and k_y , but for a given value of energy, these values depend on k_x . Solving k_x from the expression 2.14, we have:

$$k_x = \pm \sqrt{\frac{2m}{\hbar^2} (E - E_B)} \quad (2.15)$$

The geometrical representation in the k -space of the expression 2.15 is given by a set of two planes of value k_x , illustrated by two vertical planes in Figure 2.12.

The possible absorption of a photon, as in the 0D case, is going to be treated in the following. Considering a free electron final state and an initial given energy $E(k_x)$, the energy conservation rule demands that the final state energy after the absorption is:

$$E_f = E_i + h\nu = \frac{\hbar^2}{2m} k_f^2 \quad (2.16)$$

corresponding to a geometrical representation of the final state momentum given by a sphere. The momentum conservation rule can be seen as the geometrical intersection between the two planes given by the initial state and the sphere of the free final electronic state. The result of this intersection is two circles as shown in Figure 2.12.

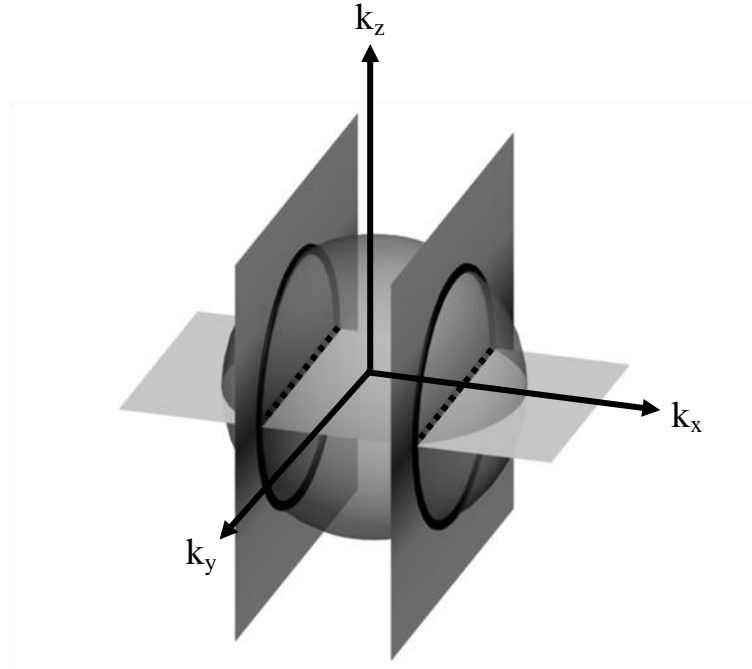


Figure 2.12 k -space representation of the free initial state for a given energy (vertical planes) and the final state (sphere) for a 1D electronic system.

As visible in Figure 2.12, the photon absorption of an electron having an initial energy E is possible only along two lines (dotted lines) in the plane given by k_x and k_y . Choosing a different binding energy, the distance between these lines and the axes origin is changing according to the expression 2.15. Replacing the z -axis of the representation from Figure 2.12 with the electron energy, it is leading to a parabolic dispersion representation parallel to the chain (x -axis), and no dispersion perpendicular to the chain (Figure 2.13).

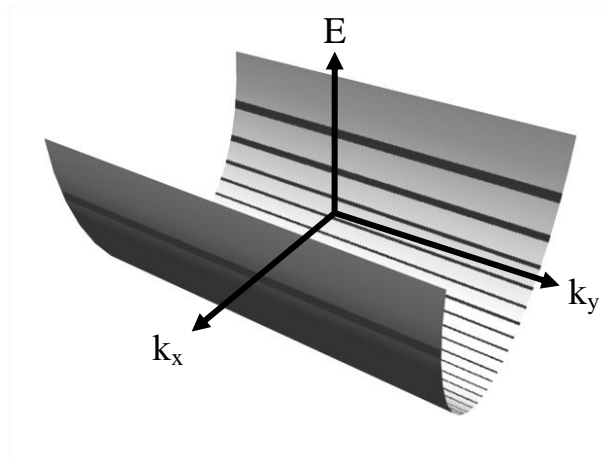


Figure 2.13 Perpendicular dispersion parallel to the chain (k_x) and no dispersion along the chain (k_y) for a 1D electronic system.

The position of the dotted line from Figure 2.12 is not changing the value if the radius of the sphere is changed. Therefore, the photon energy which dictates the sphere radius is not changing the position of the $E(k_{||})$ relationship.

Concluding, ARUPS would identify a 1D system from a non dispersing band in directions perpendicular to the confinement direction, and parabolic dispersion along the confinement direction, independently of the photon energy used.

2.5.3. Two dimensional systems

A two dimensional (2D) electronic system resembles a thin sheet of confined electrons (Fig 2.14). From the three directions of the space, the electrons are free to move on a surface.

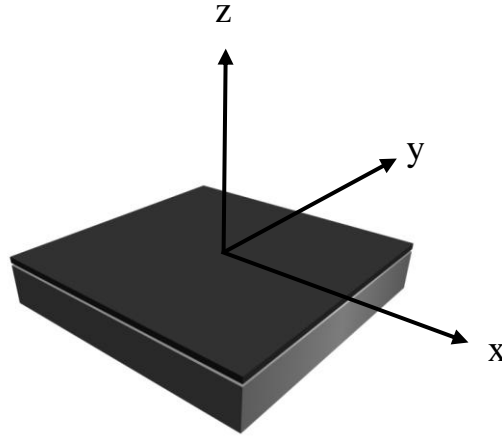


Figure 2.14 Illustration of a two dimensional system localization in the real space. The dark colored plane shows the electron confinement along the arbitrarily chosen xy plane.

A similar expression as in the 1D case but in two dimensions is chosen to describe the dispersion relationship:

$$E = E(\mathbf{k}) = E_B + \frac{\hbar^2}{2m} (k_x^2 + k_y^2) \quad (2.17)$$

The electron delocalization in the k-space exists now only along the z direction. Solving the k value from the expression 2.17 we have:

$$k_C = \sqrt{k_x^2 + k_y^2} = \sqrt{\frac{2m}{\hbar^2} (E - E_B)} \quad (2.18)$$

For a given energy E, the expression 2.18 describes geometrically in the k-space a cylinder of radius k_C .

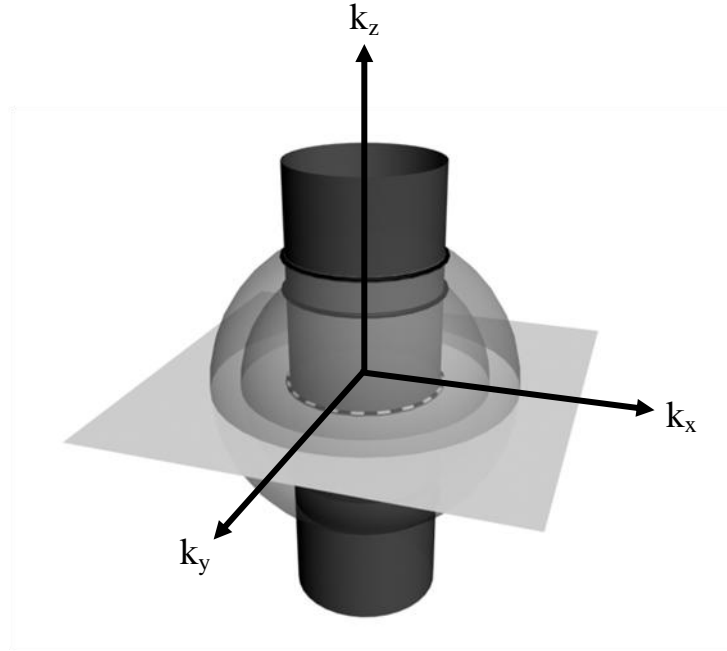


Figure 2.15 k-space localization of a 2D electronic state (dark grey cylinder). The intersection with the momentum sphere of a free electron-like state leads to a projected cut at the same k_{par} values independently of the photon energy (each sphere corresponds to a $h\nu$ value).

Considering a free electron final state described by the expression 2.11, the momentum conservation rule allows optical absorption for the electrons having the momentum where the sphere of the final state intersects the cylinder of initial state. In Figure 2.15, two spheres corresponding to two photon energies have been drawn. Independently of the photon energy, the projection in the $k_x k_y$ plane (dotted circle in Figure 2.15) is located at the same values of k .

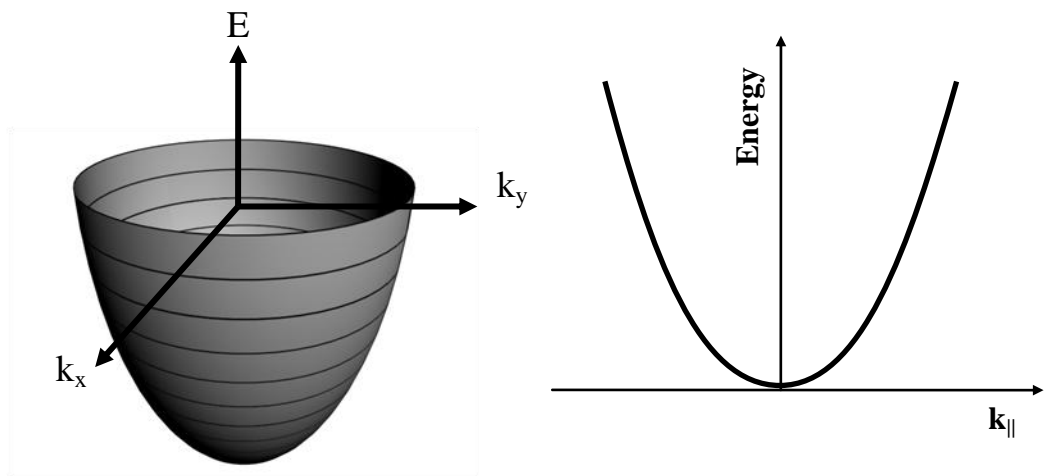


Figure 2.16 Parabolic dispersion example of a 2D electronic system.

A graphical representation of a 2D electronic dispersion replacing the k_z axis with an energy axis is given in Figure 2.16. Each circle from a plane parallel with the $k_x k_y$ plane corresponds to a different energy, given by the expression 2.18. The dispersion along any $k_{||}$ direction from the $k_x k_y$ plane is parabolic as represented in the right side of Figure 2.16.

In conclusion, ARUPS would identify a 2D electronic system as a parabolic dispersion along any direction parallel to the surface at values of binding energies, independently of the photon energy used.

2.5.4. Three dimensional electronic systems

A three dimensional electronic system can be modelled as a weakly bound electron gas confined in a solid. The electrons are almost free to move with a certain freedom in any direction. Numerous theoretical models have been developed to describe the band structure of a 3D solid. In order to illustrate the consequences of considering a three dimensional electronic system, it is enough to choose a nearly free electron gas model which outlines most of the important features recorded in an ARUPS experiment. Optical absorption is treated here by considering the repeated zone scheme of the band structure.

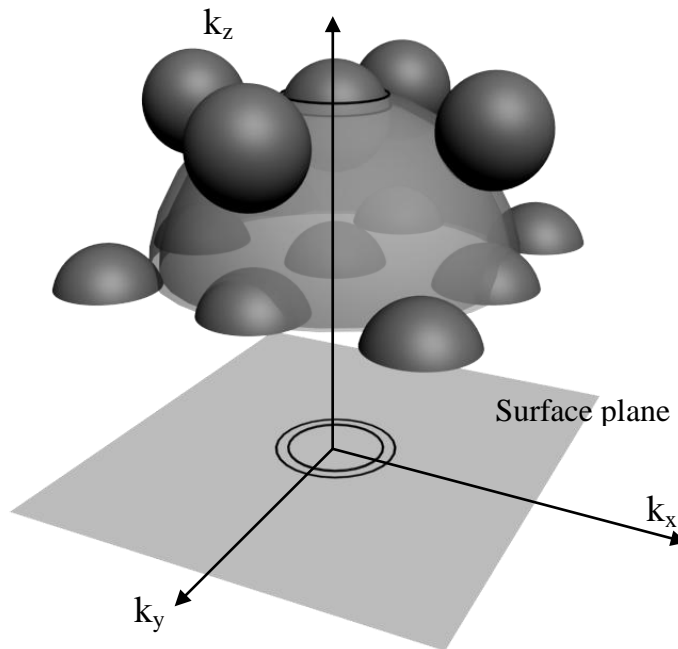


Figure 2.17 k -space localization of a 3D constant energy surface (opaque spheres). Two transparent spheres corresponding to two final states for two different photon energies are drawn. Part of the intersection is projected onto the (001) surface plane.

A general dispersion relationship for a 3D system has the form:

$$E = E(\mathbf{k}) = E(k_x, k_y, k_z) \quad (2.19)$$

For illustrative reasons, a particular situation of a nearly free initial electron state is treated in the following. For this particular situation and taking in account the repeated zone scheme of the band structure, the dispersion relationship of a certain band of the band structure in a narrow energy range can be written as:

$$E(\mathbf{k}) = E_B + \frac{\hbar^2}{2m} (k_x^2 + k_y^2 + k_z^2) \quad (2.20)$$

$$E(\mathbf{k} + n \mathbf{G}) = E(\mathbf{k}) \quad (2.21)$$

where \mathbf{G} represents a vector defining the first Brillouin zone for a given direction, and n is an integer positive number.

From the geometrical point of view, the relations 2.20 and 2.21 describes for a fixed energy an infinite periodical array of spheres having the periodicity \mathbf{G} determined by the crystal structure (Figure 2.17).

The momentum conservation rule taking into account a free electron final state given by the expression 2.13, imposes that only the electrons from an initial state having the momentum

$$k = \sqrt{\frac{\hbar^2}{2m} (E + V_0 - E_B)} \quad (2.22)$$

can go into an excited state of energy $E_f = E_i + \hbar\nu$.

As an intuitive picture, this situation can be viewed geometrically as the intersection of the array of spheres of the initial state given by the expression 2.20 and 2.21 with a sphere of the final state given by the expression 2.22. The result of this intersection is a rather complex contour in the three dimensional momentum space, part of it being illustrated with a bold line in Figure 2.17. Since in the photoemission experiments of solids, only the parallel momentum of the electrons is conserved when the electrons escape from the solid into the vacuum, a k parallel projection in the surface plane is available in the experiment (viewed in Figure 2.17 as the bold line from the surface plane). For every binding energy, the initial state array of spheres and the final state sphere radius is changing, giving raise to a rather complicated picture. Changing the value of the photon energy is leading to another radius of the final state sphere, resulting in a different intersection object. It would be possible to rebuild an entire solid Fermi surface by joining cuts measured with enough photon energies that cover at least

the size of a Brillouin zone. More details related with the electronic structure of three dimensional electronic systems and their relationship with the ARUPS experiments are part of the topic of the third chapter of this thesis, therefore an extended discussion is presented there.

2.6. ARUPS experimental setups and sample preparation

The experiments presented in this thesis were performed using two different electron energy analyzers. Most of the data for Pb/Cu(100) experiments and the Fermi surfaces of Pt(110) has been recorded with a Scienta SES2002 analyzer at APE beamline from Elettra synchrotron, Italy. High temperature data for Pb/Cu(100) and band dispersion for Pt(110) and Br/Pt(110) has been acquired using a VG-ARUPS10 electron spectrometer in our home laboratory and BL33 from MaxLab synchrotron, Sweden. Both analyzers are of electrostatic type. VG-ARUPS10 electron spectrometer has a mean radius of the hemisphere of 75 mm. An electrostatic lens system in front of the hemispheres enables to use different focus and angular resolution properties. The electrons that pass through the hemispherical energy analyzer are detected by a channeltron. The spectrometer is rotatable on a two-axis goniometer. VG-ARUPS10 achieves an actual energy resolution of 50 meV and an angular resolution of 1°. Scienta SES2002 analyzer is not movable, but due to its multi channel plate detector offers better angular and energy resolution (0.1° and 1.8 meV respectively) than VG-ARUPS10. During the time of the thesis, the ARUPS equipment from the home laboratory has experienced several important upgrades that are shortly presented in the following. The first major upgrade was the installation of a new excitation source, consisting in a high flux microwave Gammadata He lamp with monochromator. This UV lamp generates “clean” UV radiation overcoming disadvantages of classical He discharge lamp, as for example satellite radiation and low flux beam. The second important upgrade of the experimental setup was the installation of a new manipulator (PREVAC) that besides precise sample positioning features allows also sample cooling during measurements. The third main upgrade consisted in the implementation of a new data acquisition system and measurements automatization. The new system consist in a microcontroller (ATMEGA16, Atmel) based implementation, communicating with the computer via the serial port (COM). The microcontroller tasks are setting the DAC (Digital-to-Analog Converter) voltage, setting six measurement settings relays, reading

the pulses from the channeltron electronics and driving two stepped motors. As part of this thesis work, I designed and implemented the circuit electronics, including the stepped motor drivers, and also I wrote the code required for the system to work, both microcontroller side (CVAVR) and PC side (Delphi). The final applications are performing automatic band dispersion measurements and Fermi surfaces in a very user friendly manner (“one button click”).

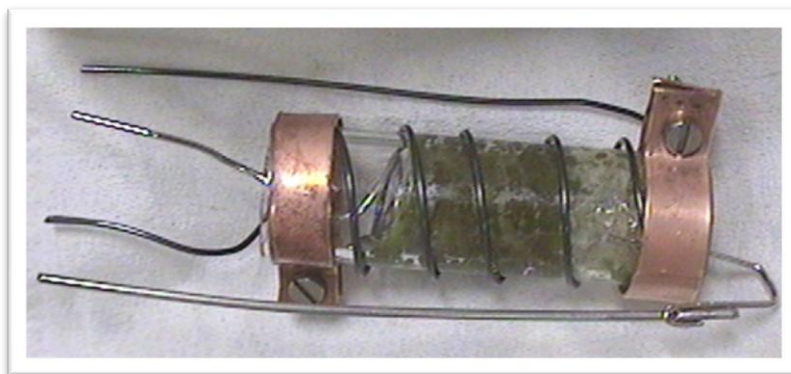


Figure 2.18 Picture of the UHV home made Br evaporator. Two wires are used for heating the electrolyte while the other two are used for applying the required voltage for the electrolysis.

The clean Cu(100) surface preparation was performed by typical Ar^+ sputtering and annealing cycles. The annealing temperature of the Cu crystal was 800 K and the partial pressure of Ar was in the range of 10^{-6} mbar. Pt(110) surface was prepared in a similar manner with the difference that it was also annealed at 900 K in a 5×10^{-8} mbar O_2 atmosphere for several minutes in order to remove C traces from the surface. A subsequent sample annealing was performed at a temperature higher than 1300 K. Pb was deposited from a homemade solid state evaporator (Knudsen cell). Br has been dosed from an electrolytic homemade cell using heated AgBr as electrolyte and Pt as electrodes (11). AgBr was initially melted into the quartz tube by heating the tube using a resistive wire. A picture of the evaporator is shown in Figure 2.18. Typically, 6 A were passed through the W filament that surrounds the cell in order to heat the AgBr to a temperature of around 400 K. Evaporation rates of 1 ML/min were achieved by polarizing the cell with 3 V at a current of 1 mA.

**CHAPTER
THREE**

3. Extension of a Tight Binding Model

The ultimate aim of an electronic structure calculation is to determine the properties of a system from only the knowledge of the constituent atoms. When done without explicit recourse to experimental data (with the exception of the use of fundamental constants and comparison with experimental results), these can be termed *ab initio* calculations. Most properties of interest can be related to changes in energy of the system of interest.

Angular resolved photoemission spectroscopy is the most direct method linked to the dispersion relationship $E(k)$ of the electronic structure. A relatively simple comparison between a theoretical model providing $E(k)$ relationship and the ARUPS data is possible only by making use of an approximation of the final state after the photon absorption. For a 3D solid, the comparison theory-experiment implies advanced analytical geometry processing of the data provided by the theoretical model. The goal of this part of the thesis was to create a link between tight binding electronic structure calculations and the ARUPS experiments. A tight binding model has been chosen due to the computational speed and the availability of the parameters of this model (12). The main assumption done to plot the ARUPS features was to consider a free electron final state in the photoemission process. Initial or final state properties were calculated making use of fast converging algorithms, resulting in a real-time and user friendly final interface. The advantage of a simplified LCAO tight binding method consists in the relative simplicity of obtaining the $E(k)$ solution. From the computational point of view, this simplicity is translated in speed, if properly implemented. The tight binding model proposed originally by Slater and Koster (13) consist in a modified linear combination of atomic orbitals (LCAO) method to interpolate the results of first-principles electronic

structure calculations. As they noted, it was computationally impossible to directly evaluate the large number of integrals occurring in the LCAO method. However, since this approach correctly shows all of the symmetry properties of the energy bands as well as providing solutions of the Schrödinger equation at arbitrary points in the Brillouin zone, they suggested that these integrals can be considered as adjustable constants determined from the results of other, more efficient, calculations or even experiments (14). The precision of the results in the frame of LCAO method are of comparable accuracy to first-principles calculations and three orders of magnitude faster (15).

3.1. Slater Koster tight binding method

Traditionally electronic structure calculations, using methods such as the wavefunction based Hartree-Fock method (16), are finding the energy of a system by solving the time-independent Schrödinger equation:

$$\left[\sum_{i=1}^N -\frac{\hbar^2}{2m_i} \nabla_i^2 + V(r_1, \dots, r_N) \right] \psi(r_1, \dots, r_N) = E \psi(r_1, \dots, r_N) \quad 3.1$$

where N is the number of particles (electrons and nuclei) with position vectors r_i . Symbolically, it can be written:

$$H(r_1, \dots, r_N) \psi(r_1, \dots, r_N) = E \psi(r_1, \dots, r_N) \quad 3.2$$

where H is the Hamiltonian given by:

$$H(r_1, \dots, r_N) = \sum_{i=1}^N -\frac{\hbar^2}{2m_i} \nabla_i^2 + V(r_1, \dots, r_N) \quad 3.3$$

However, the numerical solution of Schrödinger's equation remains a difficult task. Exact solutions of the equation are, in general, only solvable in times scaling exponentially with system size. This scaling precludes exact calculations for all but the smallest and simplest of systems. Approximations may be introduced to reduce the equations to a form that can be solved in polynomial time, but at the penalty of losing some degree of accuracy and predictive power.

In the tight binding approximation, it is assumed that the full Hamiltonian H of the system may be approximated by the Hamiltonian of an isolated atom centered at each lattice point. The atomic orbitals ψ_n , which are eigenfunctions of the single atom Hamiltonian, are assumed to be very small at distances exceeding the lattice constant. This is what is meant by tight-binding. It is further assumed that any corrections to the

atomic potential ΔU , which are required to obtain the full Hamiltonian H of the system, are appreciable only when the atomic orbitals are small. The solution to the time-independent single electron Schrödinger equation ϕ is then assumed to be a linear combination of atomic orbitals. There are four forms of a SK Hamiltonian that produce reasonable band structures: two-center orthogonal, two-center non-orthogonal, three-center orthogonal and three-center non-orthogonal (17). The implementation of a two-center non-orthogonal model has been chosen due to the transferability of the parameters from one structure to another. Furthermore, a non-orthogonal Hamiltonian is preferable on physical grounds (17). From the computational point of view, the non-orthogonal model demands twice the calculation time by solving a generalized eigenvalue problem compared with a simple diagonalization of a hermitian matrix in a case of an orthogonal model.

In the simplified LCAO-SK approach, starting from atomic orbitals $\phi_i(\mathbf{r})$, the Bloch functions are written:

$$\phi_{i,k}(\mathbf{r}) = \frac{1}{\sqrt{N}} \sum_{\mathbf{R}} e^{i \mathbf{k} \cdot \mathbf{R}} \phi_i(\mathbf{r} - \mathbf{R}) \quad 3.4$$

The Bloch functions are the basis set to develop the electron wave functions:

$$\psi_{nk}(\mathbf{r}) = \sum_i \phi_{ik}(\mathbf{r}) \quad 3.5$$

In Eq. 3.4, N is the number of primitive cells and \mathbf{R} are the lattice vectors. The solution of the Schrödinger equation is found by transforming it into the **matricial** eigenvalue problem:

$$H(\mathbf{k}) = E(\mathbf{k})S(\mathbf{k}) \quad 3.6$$

The matrix elements of $H(\mathbf{k})$ and $S(\mathbf{k})$ are given by:

$$H_{ij}(k) = \langle \phi_{ik} | H | \phi_{jk} \rangle = \sum_{\mathbf{R}} e^{i \mathbf{k} \cdot \mathbf{R}} \int \phi_i^*(\mathbf{r}) H \phi_j(\mathbf{r} - \mathbf{R}) d\mathbf{r} \quad 3.7$$

$$S_{ij}(k) = \langle \phi_{ik} | \phi_{jk} \rangle = \sum_{\mathbf{R}} e^{i \mathbf{k} \cdot \mathbf{R}} \int \phi_i^*(\mathbf{r}) \phi_j(\mathbf{r} - \mathbf{R}) d\mathbf{r} \quad 3.8$$

The integrals from Eq. 3.7 and 3.8 were calculated and tabulated in the original paper of Slater and Koster. For example, using the SK notations, if $\phi_i(\mathbf{r})$ is a p_x orbital,

$\phi_j(\mathbf{r})$ is a p_y orbital, and l, m, n are the direction cosines of \mathbf{R} , the integral is expressed as:

$$\int \phi_x(r) H \phi_y(r) dr = E_{x,y} = l m pp\sigma - l m pp\pi \quad 3.9$$

where $pp\sigma$ and $pp\pi$ orbital interaction energy are the parameters obtained by fitting more efficient calculations or even an experiment.

Neglecting high order orbitals as well as spin-orbit splitting, on a spd basis, the H and S matrices have a 9×9 dimension, resulting from the orbitals geometry: $s, p(x), p(y), p(z), d(xy), d(yz), d(zx), d(x^2-y^2), d(3z^2-r^2)$.

To calculate the energy eigenvalues for a given crystal structure, one begins by choosing an atom and its neighbours. Each neighbour j is contributing with the e^{ikR_j} factor to the matrix elements of H and S. For example, for an fcc structure, parametrized values of the energy integrals can be found in literature (18) by choosing twelve first neighbours of (110) type and six second neighbours of (200) type (Figure 3.1)

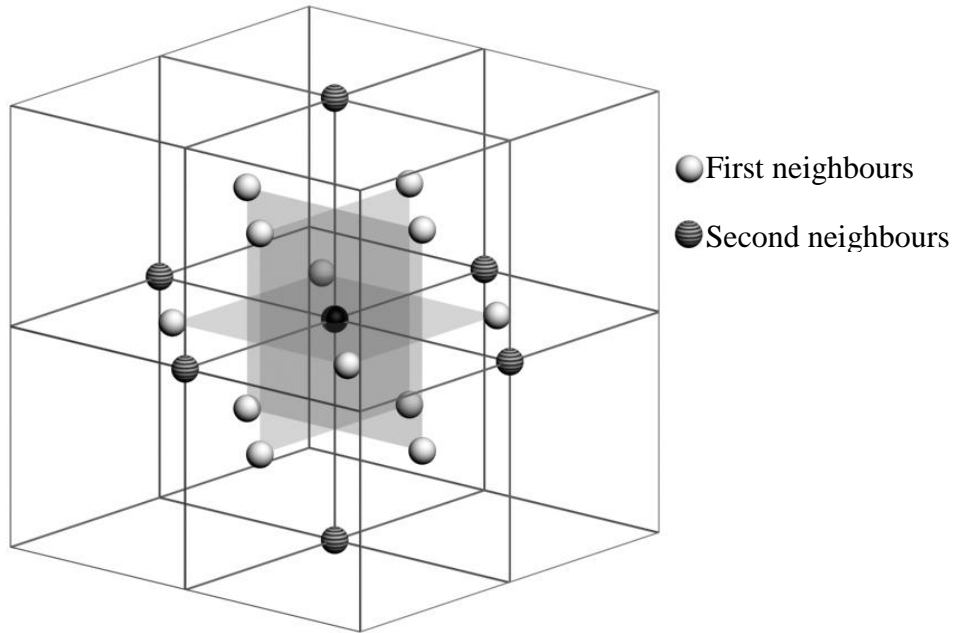


Figure 3.1 First and second nearest neighbours for an fcc structure.

From the computational point of view, the most considerable effort is spent in calculating complex exponential values at each k point for each of the neighbours chosen. Continuing illustrating with the fcc example, the H and S matrix elements are:

$$H_{ij} = \sum_{nf=1}^{12} e^{ikr_f} E_{ij}(k, r_f) + \sum_{ns=1}^6 e^{ikr_{fs}} E_{ij}(k, r_{ns}) \quad 3.10$$

with a similar expression for S (choosing the overlap energy integrals expressions instead of the energy integrals). n_f and n_s represent the number of the first and the second neighbour chosen, and r_f and r_s are the distances between the center atom and the neighbour position.

A fast implementation for calculating $E(k)$ solution would benefit if the sum of the complex exponentials would be expressed in an analytical form and calculating only one sinus instead of N, where N is the total number of neighbours. The original paper of Slater and Koster gives analytical solutions of the exponential sums for the particular situations of simple cubic, fcc and bcc structures. To obtain these analytical solutions, thorough trigonometric calculations have been performed (13). The level of complexity was leaking in small errors corrected after by Sharma (19).

3.2. Computer analytical solutions of the Slater Koster Hamiltonian matrix elements

The development of modern computers at the time of this thesis gives the possibility to perform advanced symbolic expression calculations (20). Any possible mathematical or typing errors are avoided, and elaborate simplifications of the final results are pushing the speed of the further calculations using the obtained expressions.

In the following, the code used in Mathematica TM (20) as input to obtain the analytical form of the H matrix elements of the fcc is going to be described.

First, the position vectors of first twelve and second six neighbours are defined as:

$$rf = \{ \{1,1,0\}, \{-1,-1,0\}, \{0,1,1\}, \{0,-1,-1\}, \{1,0,1\}, \{-1,0,-1\}, \{1,-1,0\}, \{-1,1,0\}, \\ \{1,0,-1\}, \{1,0,1\}, \{0,1,-1\}, \{0,-1,1\} \}$$

$$rs = \{ \{2, 0, 0\}, \{-2, 0, 0\}, \{0, 2, 0\}, \{0, -2, 0\}, \{0, 0, 2\}, \{0, 0, -2\} \}$$

The hardest part consists in providing the expression of the energy integrals (13) as an input in the $E_{ij}(l,m,n)$ vector, where l, m and n are the cosines directions of r_f and r_s . The orbital interaction energies ($ss\sigma$, $sp\sigma$, ...) are left in their symbolic form. The last step in obtaining the analytical expression of H matrix element of the fcc structure

is to simplify the trigonometric expressions obtained by the summation of the complex exponentials:

$$\mathbf{H} = \text{Table} \left[\text{FullSimplify} \left[\text{ExpToTrig} \left[\sum_{p=1}^{12} e^{i k r_f} E_f(p, i, j) + \sum_{p=1}^6 e^{i k r_s} E_s(p, i, j) \right], \{i, 1, 9\}, \{j, 1, 9\} \right] \right]$$

The “Table” function is iterating i and j indexes from 1 to 9, calculating all the matrix elements of \mathbf{H} . “FullSimplify” finds the optimal analytical expressions of the result of the function “ExpToTrig” which has as input the sum of 18 (12+6) complex exponentials contribution of the first and second neighbours.

\mathbf{H} will contain all the matrix elements in an analytical form. The first two are pasted here in order to illustrate the output:

$$H_{1,1} = \text{ss0} + 2 (2 \text{ss}\sigma_1 (\text{Cos}[y] \text{Cos}[z] + \text{Cos}[x] (\text{Cos}[y] + \text{Cos}[z])) + \text{ss}\sigma_2 (\text{Cos}[2x] + \text{Cos}[2y] + \text{Cos}[2z]))$$

$$H_{1,2} = 2 i (2 \text{sp}\sigma_2 \text{Cos}[x] + \sqrt{2} \text{sp}\sigma_1 (\text{Cos}[y] + \text{Cos}[z])) \text{Sin}[x]$$

It is important to note that the onsite energies (ss0 for example) for the diagonal elements of \mathbf{H} , and 1 for the diagonal elements of \mathbf{S} are added in the end.

Beside the correctness of results, analytical results for more complicated structures can be obtained in a matter of minutes. At least one order of magnitude in time is gained for the fcc structure if one uses in the implementation the analytical matrix elements expressions.

3.3. Constant energy surfaces

One of the first calculated constant energy surface was the Fermi surface of copper, published by Burdick et al in 1963 (21). At that time, the computers capabilities have allowed the calculation of very few $E(k)$ points.

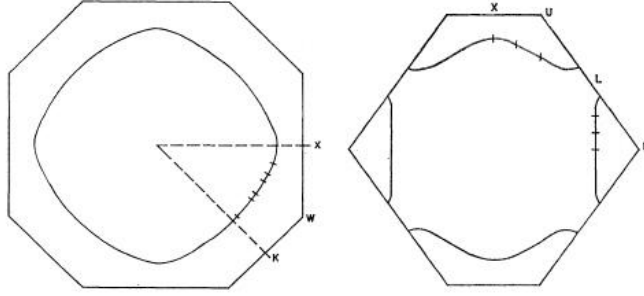


Figure 3.2 (100) (left) and (110) (right) cross sections of the Fermi surface of Copper (from reference (21)).

Figure 3.2 shows cross section of the Fermi surface of copper in the (100) and (110) planes. The cross sections were calculated in the original paper of Burdick (21) making use by of Augmented Plane Waves (APW) method.

Most of the published constant energy surfaces are calculated at the Fermi level, since the Fermi surface has a major physical significance (conduction properties of the crystal, for example). As raw data, no publication contains Fermi surface values due to the fact that a too large number of points is forming a Fermi surface. The only source that provides a link to Fermi surface data is reference (22). During the beginning of this thesis, the web page cited in the reference (22) was the only source of data that could be compared with the experimental Fermi surfaces. No data of constant energy surfaces at binding energies different from Fermi level was available.

The simplified tight binding method of Slater and Koster is three orders of magnitude faster than the APW method, giving results of comparable accuracy (14). The electronic structure obtained using tight binding model is good enough to be compared with an ARUPS experiment. Even if it is running three orders of magnitude faster than APW, the authors using a TB method from reference (22) are claiming the fact that several days of running code on a cluster of 20 modern computers in the year 2000 was required to calculate the Fermi surface of 47 elements. Reference (22) doesn't

provide too many details on how the code was implemented, neither how the isosurfaces were generated. The positive aspect of the work of reference (22) is the fact that historically it is the first time that computational raw data of electronic structure become available to ARUPS experimentalists. On the other hand, there are several negative aspects. First of all, it is creating the impression that calculating constant energy surfaces is out of the hand of the experimentalists. The computer advances when this thesis was done compared with the year 2000 are only a factor of 3, 2000 was the year when the processor reached 1 GHz clock rate, nowadays they are at 3 GHz. Second, the code that was creating the isosurfaces was rather imperfect because there are visible holes in some of the calculated Fermi surfaces. Moreover, isosurfaces at binding energies different from Fermi level are not available.

In the following subchapters it will be explained how it is possible to obtain accurate constant energy surfaces, electronic band structure and ARUPS features at an interactive rate. This was made feasible due to several things, among them it should be mentioned a novel converging algorithm for the determination of points of the constant energy surfaces and also the use of processor specific compiled libraries for calculating the generalized eigenvalue problem (23).

3.4. Marching Cubes and Advanced Marching Cubes algorithm

Marching Cubes (MC) is a computer graphics algorithm, published in the 1987 SIGGRAPH proceedings by Lorensen and Cline (24) for extracting a polygonal mesh of an isosurface from a 3D scalar field. Advanced Marching Cubes (AMC) algorithm is a modification of MC and it was developed during the time of this thesis for a faster and more precise calculation of constant energy surfaces.

A short description of the MC algorithm is necessary to describe AMC. The MC algorithm first creates a 3D grid of adjacent cubes and calculates the function value(s) at the corner point of each cube. For the tight binding model implemented, there are 9 energy values for each k point. The fundamental problem is to form a facet approximation to an isosurface through a scalar field sampled on the rectangular 3D grid. Given one grid cell defined by its vertices and scalar values at each vertex, it is necessary to create planar facets that best represent the isosurface through that grid cell. The isosurface may not pass through the grid cell, it may cut off any one of the vertices,

or it may pass through in any one of a number of more complicated ways. Each possibility is characterized by the number of vertices that have values above or below the isosurface (Figure 3.3).

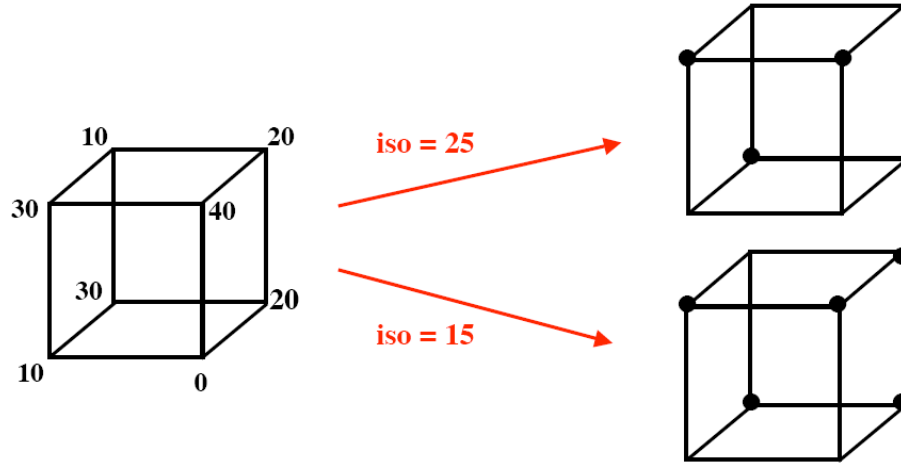


Figure 3.3 Marking the cube corners (spheres) if the corner value is bigger than the iso-value that is calculated.

If one vertex is above the isosurface and an adjacent vertex is below the isosurface then the isosurface cuts the edge between these two vertices. The position that cuts the edge will be linearly interpolated, the ratio of the length between the two vertices will be the same as the ratio of the isosurface value to the values at the vertices of the grid cell. The number of possible combinations of “above” or “below” values for 8 points is $2^8=256$. So, what makes the algorithm "difficult" is the large number (256) of possible combinations and the need to derive a consistent facet combination for each solution so that facets from adjacent grid cells connect together correctly. With a proper indexing convention, each case can be indexed and the facets can be built by looking in a precalculated table. Nevertheless, the precalculated array of 256 cube configurations can be obtained by reflections and symmetrical rotations of 15 unique cases, shown in Figure 3.4.

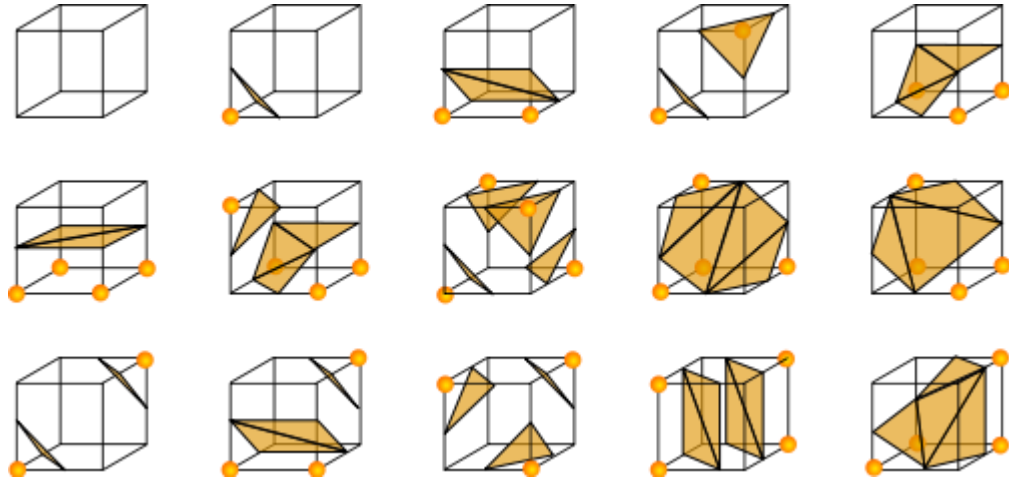


Figure 3.4 Building the iso-facets. The 15 unique cases from 256 obtained by reflections and symmetrical rotations are shown. The cube corners marked by a sphere have values above the isosurface value, the rest have values below.

Joining all the facets obtained in all the cubes, one has the full facet representation of the isosurface. Graphical and physical properties of the isosurface depend also on the surface normal at each point. The surface normals are calculated by interpolating the difference in all three spatial directions of the closest grid values.

The MC algorithm is using interpolation to generate the points of the isosurface, therefore decreasing the accuracy of the results. In order to increase the precision of the calculated points and to reduce the calculation time, a new way of calculating the position of the point along the cube edge has been implemented. The implementation of Advanced Marching Cubes algorithm is using the bisection method where the solution is encountered by iteratively dividing the cube edge that contains an isosurface point in half, choosing as next segment to divide the one that has the corners with different sign values different from the isovalue (one below and the other above). The difference with MC is that instead of marking the cubes with above and below values, AMC is marking iteratively the segments that contains points of the isosurface.

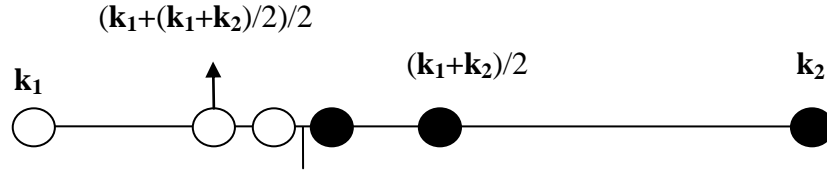


Figure 3.5 Illustration of the bisection method. Black circles have values bigger than the iso-value and the empty circles have values smaller than the iso-value.

The iteration of dividing the edges in half can go until a certain number of iterations or until a certain precision is obtained.

For the same size of the grid, AMC is slower than MC by calculating extra points for each of the cube segments. On the other hand, AMC does not need high values for the grid size to achieve more precise values than MC, because the bisection method is a convergent method. And since the total number of points is the grid size to the power of three, the AMC can run much faster giving more precise values. In principle, AMC can be applied to any analytical scalar field in order to generate fast and precise isosurfaces.

The symmetry of the Brillouin zone plays an important role when choosing the initial grid. It is absolutely unnecessary to calculate inside a large cube containing a full Brillouin zone. For the fcc, bcc and hcp Brillouin zones, it is enough to calculate the isosurface inside a cube having a corner at $k=(0,0,0)$ and the opposite corner at $k=(\pi/a, \pi/a, \pi/a)$ or $k=(\pi/a, \pi/a, \pi/c)$. a is the lattice constant of the unit cell of the fcc and bcc structure, and a and c are the lattice constants for the hcp structure. The rest of the isosurface in the Brillouin zone can be calculated by applying symmetry operations to the reduced isosurface. The case of the fcc structure is going to be discussed as an example of the importance of reducing the cube grid size.

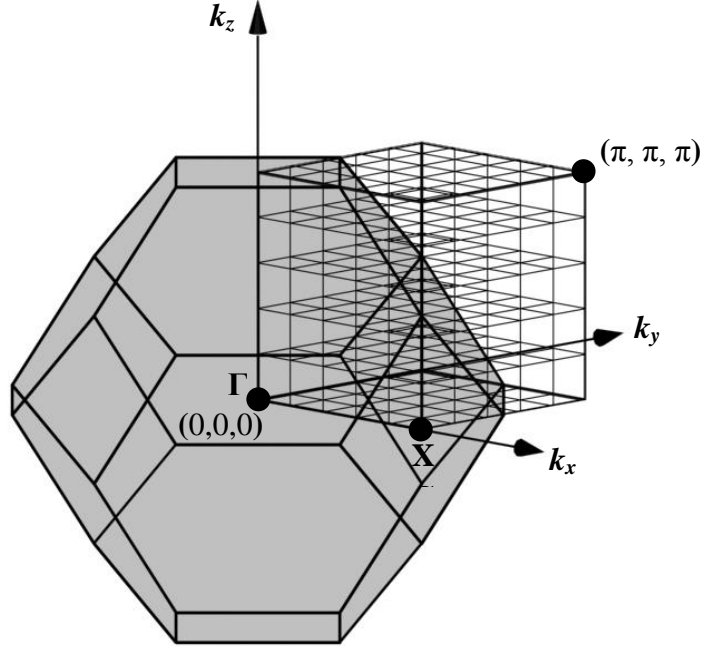


Figure 3.6 Illustration of choosing the cubes for the fcc Brillouin zone. The grid size value is 5 in figure. The lattice parameter a of the fcc structure is arbitrarily chosen to have a value equal to one.

The authors from reference (22) claimed a grid size of 160, resulting in a total number of $160 \times 160 \times 160$ values that have to be calculated. When looking to their data of Copper, one can observe that the actual length of the edge of a cube corresponds in dividing the fcc Brillouin zone from the Γ point to the X point in 40 segments. Choosing a grid size value of 40 in the way illustrated in Figure 3.6, one can go to the same result by simply dividing one eighth of the Brillouin zone in $40 \times 40 \times 40$ cubes. The result is that the same accuracy can be obtained 32 times faster simply taking in account the symmetry of the Brillouin zone. Another advantage of choosing the cubes as described before is that the isosurface has to be clipped only with the (111) plane from the L point of the Brillouin zone. In fact if the symmetry is not taken into account, the isosurface has to be clipped with 10 planes (4 at the X points and 6 at the L points).

3.5. The radial projected surface method

The radial projected surface method is making use of the property that, in general, a segment joining the Γ point and any point from the boundary Brillouin zone planes is intersecting a constant energy surface in maximum one point for most of the elements (especially their sp bands). When this is the case, one can rely on a very simple method to obtain constant energy surfaces.

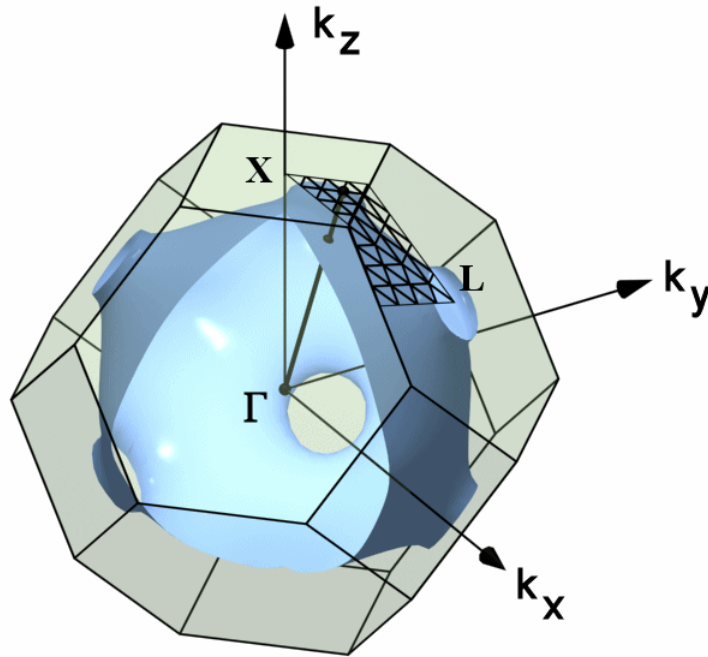


Figure 3.7 Illustration showing a grid of triangles enclosing the irreducible Brillouin zone of the fcc structure. By knowing the intersection point between the segments joining the triangle edges and the Γ point and the isosurface, one can rebuild the constant energy surface by projecting the triangle array onto the intersection points.

Figure 3.7 is illustrating the method used in the projected surface algorithm. The first step consists in building a triangle array lying onto the planes of the Brillouin zones. The triangles are chosen in such a way that the Γ point and the surface defined by these triangles is enclosing the irreducible Brillouin zone of the structure. For the fcc case illustrated in Figure 3.7, there are three tessellated triangles, one lying on the plane containing the X point, and two lying on the plane containing the L point. In fact, for the fcc structure, the irreducible Brillouin zone is 1/48 of the total volume. The next step is based on the assumption that between the points defining each of these triangles and the Γ point, there is maximum one point having the energy value equal to the value of

the isosurface that we want to calculate. When the energy value minus the isovalue at the Γ point at the triangle corner has the same sign, it means that there are no points crossing the isosurface. If the signs are different, the bisection method described in the previous subchapter can be used to find the \mathbf{k} value of the isosurface point. To build the isosurface, the triangles are basically radially projected on the points found by the bisection method. If no point has been found for a given corner of a triangle, the algorithm is checking the state of the surrounding corners. A triangle corner can be discarded if the neighbours had no solutions, or the triangle corner can be recalculated using k segment joining the corner with the X or L point if the neighbours had solutions.

The isosurface normal vector of an isosurface point can be calculated by smoothing the normal vector of the adjacent triangles. It is a rather complicated task since symmetry considerations have to be applied to the triangle corners sitting at the edges of the three tessellated triangles. Another possibility to determine the normal vector is to calculate six extra energy values, the normal vector \mathbf{n} for a given corner of momentum \mathbf{k} has the value:

$$n_x = E(k_x + dk_x) - E(k_x - dk_x)$$

$$n_y = E(k_y + dk_y) - E(k_y - dk_y)$$

$$n_z = E(k_z + dk_z) - E(k_z - dk_z)$$

The value of dk_x , dk_y , dk_z should be chosen as small as possible in order to have precise normal vectors.

The most important advantage of the projected radial surfaces method is the speed. It is no longer necessary to calculate a huge numbers of points like in the marching cube method. Basically, instead of calculating energy eigenvalues in a number of points equal to the grid size to the power of three, one can much better implement symmetry considerations and calculate a number of points equal to the tessellation size of the triangles to the power of two. The radial projected constant energy surfaces have the disadvantage of not being a general case to calculate constant energy surfaces, since not all of them are satisfying the condition described in the beginning of this subchapter. A solution to this problem could come by trying to roll an array of triangles on the isosurface. In two dimensions, the equivalent would be generating an isocontour by following its path by rotating small segments. It is relatively simple to implement, but

generalizing the solution in three dimension is a rather complicated problem. Up to my knowledge and based on an extensive literature research, there are no implementations of a rolling surface. A possible implementation of rolling surface would not only boost the calculation speed of the electronic structure constant energy surfaces, but also it would be for any analytical scalar field in general.

3.6. Spherical cuts of constant energy surfaces

As described in the first chapter of this thesis, one typical ARUPS experiment consists in mapping the angular (hence $k_{||}$) distribution of the photoemitted electrons for a certain photon energy value from a small energy window centered at a fixed binding energy value. A particular case is the Fermi surface mapping, when $E_b=0$ eV. From the theoretical point of view, assuming a free electron like final state and neglecting photoemission matrix element effects, one ends up in the k -space by plotting a chart that contains the surface specific projected cut of the intersection between the constant energy surface in the repeated Brillouin zone with the sphere of the free electron final state, whose radius is related with the photon energy used (Figure 3.8).

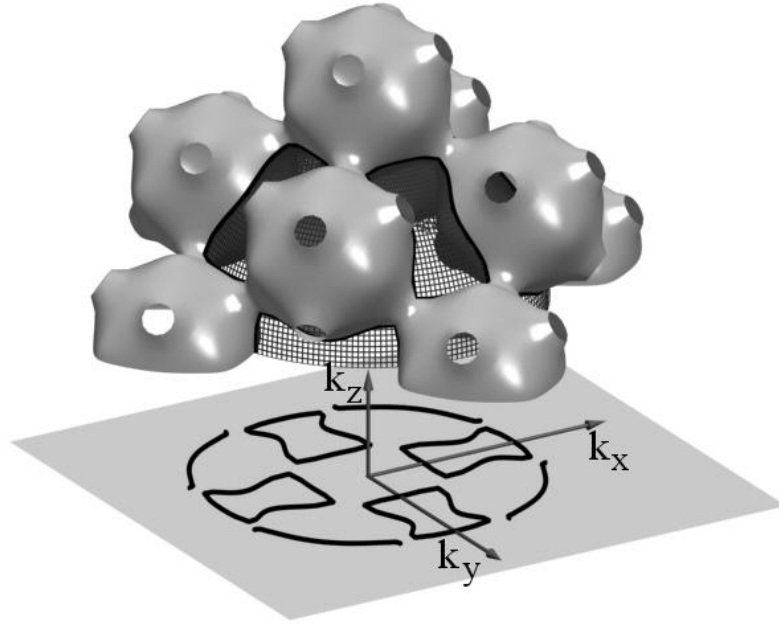


Figure 3.8 Illustration of a projected spherical cut of the Fermi surface of Copper in the repeated Brillouin zone. The corresponding surface of the projection is the (001) face.

It is useful to remember that the radius of the sphere (a part is displayed in Figure 3.8 as a rectangular mesh half sphere) is:

$$k_r = \sqrt{\frac{\hbar^2}{2m}} \sqrt{h\nu + V_0 - E_b}$$

where $h\nu$ is the photon energy, V_0 is the crystal inner potential constant and E_b is the binding energy of the emitted photoelectron.

In the repeated zone scheme, the orders h, k, l of Brillouin zones have values in theory from $-\infty$ to $+\infty$. In the calculations of the spherical cut, only those orders are considered which satisfy the condition that the final state sphere is passing through the Brillouin zone defined by h, k and l . This can be accomplished by imaginarily enclosing a given BZ in a sphere of radius π/a , where a is the minimum of the three real space lattice constants. If the reciprocal space translational vector multiplied by the BZ order makes that the enclosing sphere intersects with the final state sphere, then the given BZ order is considered for the calculation of the spherical cut.

In photoemission spectroscopy of surfaces, one has access only to the excited electrons that leave the crystal. This simple argument implies that only the half of the final state sphere pointing outwards the surface should be considered in the intersection with the constant energy surfaces. It also implies that only the half space of the repeated Brillouin zones pointing outwards of the given surface have to be considered when making the intersection.

At this point, the calculated constant energy surfaces as an array of triangles are crucial in determining the cut. The constant energy surface is first translated to the necessary h, k and l values that matter for calculating the cut, then the problem of finding the contour is reduced to the problem of determining the array of segments of the constant energy surface triangles that intersect the half sphere of the final state. During the time of this thesis, the first approach was to relate a tight binding model with the ARUPS experiments by using the Fermi surfaces from reference (22).

There are four particular geometrical situations for the position of a triangle respect to a sphere, as illustrated in Figure 3.9.

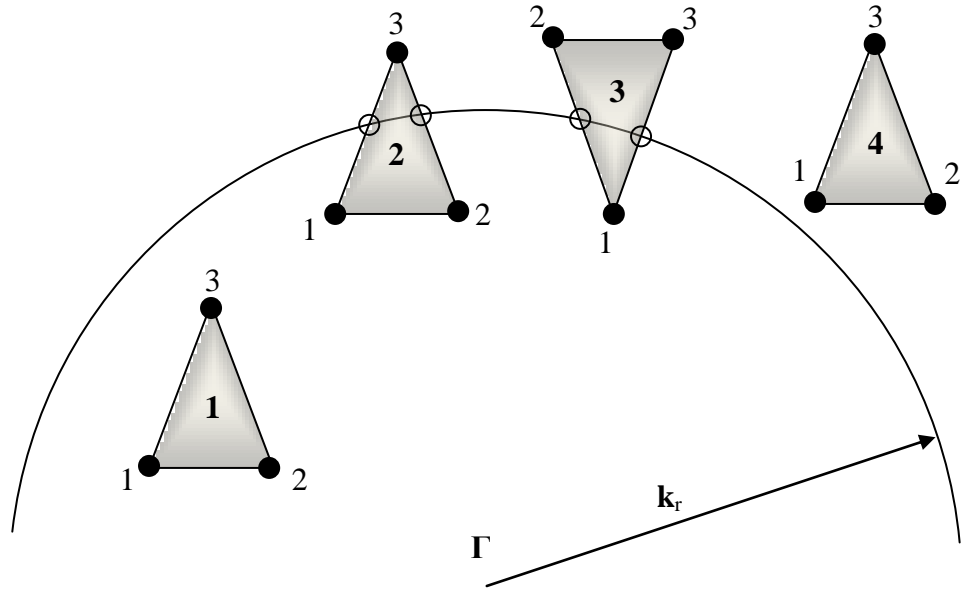


Figure 3.9 Illustration of the four particular positions of a triangle respect to a sphere. The triangle corners are marked with normal font numbers, and the triangles are marked with bold numbers.

Triangles 1 and 4 from **Figure 3.9** correspond to a case when all the points of the triangle have the distance to the center Γ point smaller (triangle 1) or bigger (triangle 4) than the sphere radius. The other two situations correspond to the cases when either one (triangle 3) or two (triangle 2) corners are inside the sphere, and the other corners are outside. For triangles 2 and 3 one has to calculate the intersection points between the triangle edges that have one point outside the sphere and one point inside the sphere. The analytical solution of line sphere intersection can be found in analytical geometry handbooks (25). The particular problem of finding the coordinates of the point P that results from the intersection of a line segment given by two vectors \mathbf{P}_1 and \mathbf{P}_2 with a sphere of radius r is not simplified in geometry handbooks. A fast implementation for calculating the coordinates of the intersection point P is presented in the following:

A vector \mathbf{P} stays on the segment given by the vectors \mathbf{P}_1 and \mathbf{P}_2 if:

$$\mathbf{P} = \mathbf{P}_1 + u(\mathbf{P}_2 - \mathbf{P}_1), \text{ where } u \in (0,1) \text{ (line segment equation)}$$

The problem is to find the value of u which makes that the point \mathbf{P} stays on the sphere with the origin at 0. Mathematically this means that the dot product of \mathbf{P} with itself is:

$$\mathbf{P} \cdot \mathbf{P} = r^2 \text{ (sphere equation)}$$

Combining the last two expressions, one obtains:

$$\mathbf{P}_1 \cdot \mathbf{P}_1 + 2u\mathbf{P}_1 \cdot (\mathbf{P}_2 - \mathbf{P}_1) + u^2(\mathbf{P}_2 - \mathbf{P}_1) \cdot (\mathbf{P}_2 - \mathbf{P}_1) = 0$$

In the implementation, first the dot product $\mathbf{P}_1 \cdot \mathbf{P}_1$ is calculated, then the difference vector $(\mathbf{P}_2 - \mathbf{P}_1)$, then its dot product and the dot product with \mathbf{P}_1 . The solution is obtained by solving a second order equation in u . Once u is obtained, the coordinates of the point P can be calculated.

After iterating through all the triangles of all the translated constant energy surfaces in the k-space, an array of segments in the 3D k-space is obtained. The last task is simply to plot the segments as a function of their k_{\parallel} values (parallel refers to the crystal surface). This implies basically to project them onto the plane given by the surface Miller indexes. In **Figure 3.8**, the projection in the (001) surface plane is shown. This kind of plot can be directly compared with the experimental ARUPS constant energy surfaces.

3.7. Theoretical band dispersion

The most typical ARUPS measurements consist in determining the band dispersion along a given k_{\parallel} direction of the surface for a fixed photon energy. As described in the first chapter, the results can be plotted even in a waterfall like chart or as grayscale images. The grayscale images have the advantage that one can draw directly the $E(k_{\parallel})$ dispersion, but enough angular resolution and signal to background ratio is needed.

Calculating $E(k_{\parallel})$ bands starting from a tight binding model seems to be at first sight more complicated than calculating constant energy surfaces cuts. The prerequisites of the following assumptions are based in the model of a free electron final state bond. Basically, for each binding energy that one wants to plot in the $E(k_{\parallel})$ chart, a corresponding isosurface should be calculated (at least once). The situation is illustrated for several binding energies in Figure 3.10. Each isosurface corresponding to a given binding energy is cut by a sphere of radius dependent on the binding energy (the photon energy supposed to be fixed). The plane of measurement is defined by the surface normal direction and the k_{\parallel} direction. Along this plane the free electron final sphere is reduced to a circle. The $E(k_{\parallel})$ band dispersion for a specific band would consist in

joined points that come from the circle-isosurface intersection, as displayed in Figure 3.10.

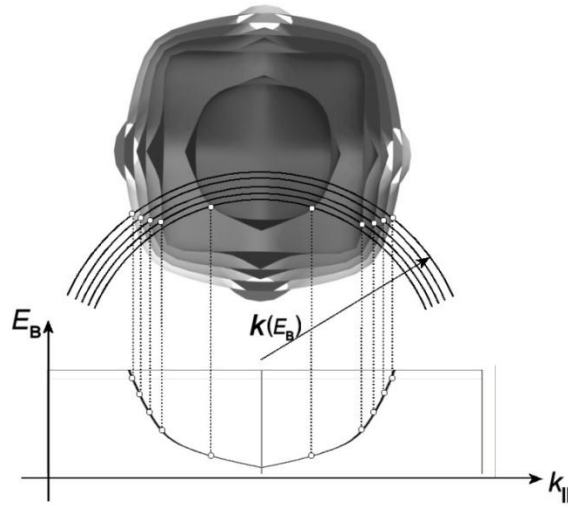


Figure 3.10 Each point from a $E(k_{\parallel})$ plot originates from the intersection of the specific CES surface with the circle of radius corresponding to the photon energy and binding energy measured.

There is one physical argument that makes that $E(k_{\parallel})$ plots are calculated much easier than described before. A given band can appear only once in a vertical line of the $E(k_{\parallel})$ dispersion. Having this in mind, one can try to imagine what would happen when following a segment starting from the Γ (0,0,0) point and going to any direction in the plane given by k_{\parallel} direction and the surface normal direction (see Figure 3.11).

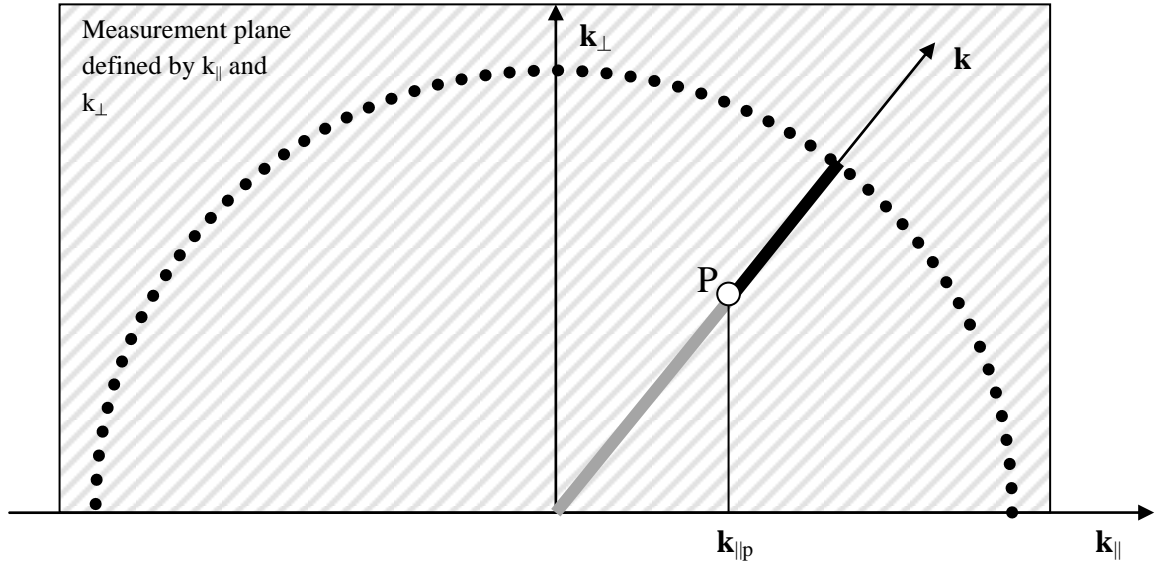


Figure 3.11 Finding the E_b value for a certain \mathbf{k} moving along a k direction. If at the value $k_{\parallel p}$ the difference described in the text becomes 0, the point P appears in the $E(k_{\parallel})$ diagram.

For a given band, each point of this segment has a specific value of binding energy calculated by the tight binding model. For this calculated value of binding energy, it corresponds a certain value of the radius of the free electron final state sphere. If the two specified values are equal, then the point will appear as a point in the $E(k_{\parallel})$ diagram. Moreover, it is possible to apply the bisection algorithm in order to find the point, resulting in a fast and precise implementation. One has to check for which k value the difference between the two specified values is equal to 0. The expression has the form:

$$\sqrt{\frac{\hbar^2}{2m}} \sqrt{h\nu + V_0 - E_b(\mathbf{k})} - |\mathbf{k}| = 0$$

The first part of the above expression corresponds to the radius of the free electron final state for the binding energy given by the \mathbf{k} value.

The dotted circle from Figure 3.11 shows how a segment starting from the Γ (0,0,0) point and ending in these bold points has to be iterated in order to fully cover a certain k_{\parallel} direction. The iteration has to be performed separately for each band of the tight binding model. The radius of the dotted circle should correspond to a free final

electron final state energy slightly higher than the Fermi level in order to be able to plot the occupied bands.

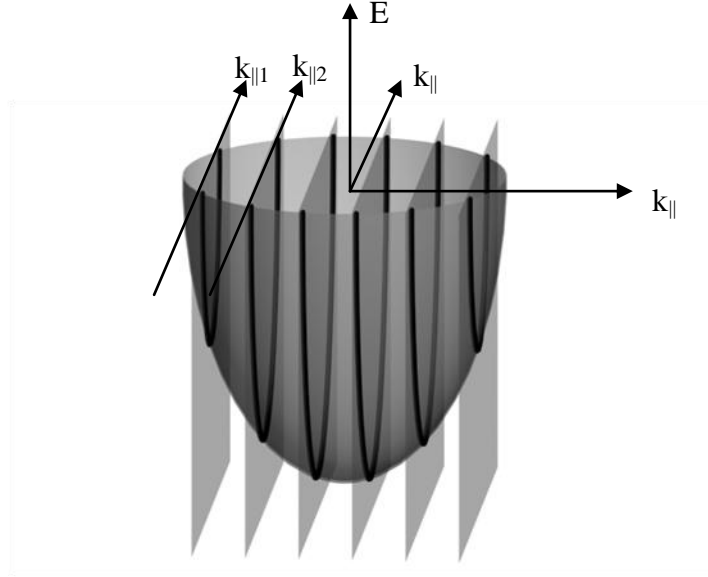


Figure 3.12 Illustration of the method chosen to calculate $E(k_{\parallel x}, k_{\parallel y})$ plots. Contours are first calculated in parallel planes containing several $k_{\parallel i}$ vectors and joined after into a 3D object (the paraboloid).

Besides the precision of the presented method, there is another advantage when the $E(k_{\parallel})$ calculation is running fast. By iteratively moving the k_{\parallel} vector to a parallel position $k_{\parallel} + dk_{\parallel}$, it is possible to map completely in a reasonable time a band position for a fixed photon energy. Dividing an initial k_{\parallel} vector into its components $k_{\parallel x}$ and $k_{\parallel y}$, it is possible to obtain a 3D representation of E_b as function of $k_{\parallel x}$ and $k_{\parallel y}$: $E(k_{\parallel x}, k_{\parallel y})$ (see Figure 3.12). The initial k_{\parallel} can be any k_{\parallel} vector perpendicular to the surface normal. The contours from each plane of Figure 3.12 will contain an equal number of points, therefore it is possible to join the segments into quads and to draw a facet representation of the $E(k_{\parallel x}, k_{\parallel y})$ function. The 3D object obtained contains an approximation of the binding energy value for any k_{\parallel} value for a fixed photon energy. When clipping this object to a certain binding energy level, one can see from the top view of the cartesian system from Figure 3.12 nothing else than a constant energy cut. More discussion about this topic is going to be presented in the result section of this chapter.

3.8. Projected band gaps

A surface projection of all the possible crystal electronic bands is not always filling all the $E(k_{||})$ space. The regions that are not filled are the so called projected band gaps of the crystal electronic structure. The symmetry breaking at the surface of a crystal makes that parts of these forbidden regions can be occupied by surface localized electrons. The fundamental importance in surface science of the projected band gaps resides in the possibility of identifying states at the surface of the crystal.

Two major maps of projected band gaps can be obtained. The first one consist in projecting all the electronic states for a fixed binding energy for all $k_{||}$ values (Figure 3.13 left). The second kind of map is obtained by making a projection of all the binding energies of all the electronic states along a fixed $k_{||}$ direction (Figure 3.13 right). The example of band projection is illustrated for the Cu(111) surface in Figure 3.13. As it can be observed, there are white regions where no crystal states can exist. If a theoretical model is reliable, any state identified by ARUPS that appears in the gaps of the projected bulk band structure is a candidate for a possible surface state.

The question that arises is how starting from the $E(k)$ values given by a theoretical model, one can obtain the projected band gaps. The answer is straight forward for the first kind of maps described before. It is enough to project on the crystal surface plane the isosurface for the binding energy that is plotted. Of course the isosurface should be translated to sufficient symmetry points of the reciprocal space in order to cover an irreducible zone for the crystal surface that is being analyzed.

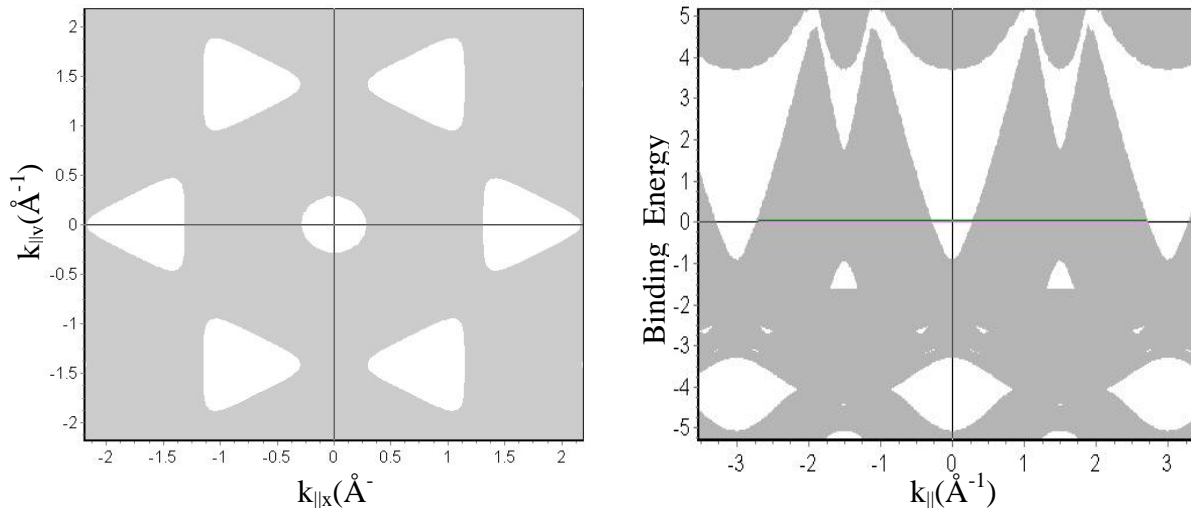


Figure 3.13. Projected band gap plots of the Cu(111) surface. On the left side, the binding energy is fixed, therefore the two components of k_{\parallel} are forming the chart axes. On the right side, the projection is done by keeping the k_{\parallel} vector in the surface plane and varying the binding energy

A fast implementation of the projection of the translated isosurfaces was done by using the capabilities of the hardware implemented computer graphic card functions. As input, a single isosurface represented by an array of triangles is supplied to the graphic card. This array of triangles is then translated to the necessary symmetry points and projected on the surface plane. If no lighting calculations are done by the graphic card, the result is the image map of the triangle projection on the surface plane. The final result is obtained by rescaling the image to the original crystal k_{\parallel} values.

The second kind of maps, where the binding energy is on the ordinate of the plot, is obtained in a completely different way. An intuitive way of thinking how this map is generated would be imagining the bands plotted for the fixed k_{\parallel} direction for a lot of photon energies. The bands would never enter to the gaps and if the step in photon energy is small enough, the bands would fill a certain region leaving the gaps exposed. This intuitive image would work rather slow in the implementation since generating bands for a certain photon energy requires the convergent algorithm described in the previous subchapter. Even if it is not so intuitive, the projection map is obtained faster if one is sweeping not the photon energy, but the k_{\perp} values for a given k_{\parallel} direction. The surface normal with the fixed k_{\parallel} direction is defining a plane in the k -space. Calculating energy values for a band along lines of constant k_{\parallel} for different k_{\perp} values as illustrated

in Figure 3.14, one can map a slice of the plane large enough to cover a region of reciprocal space that is irreducible for the given crystal surface. For example, it is enough to sweep in the length of one Brillouin zone for a (001) surface.

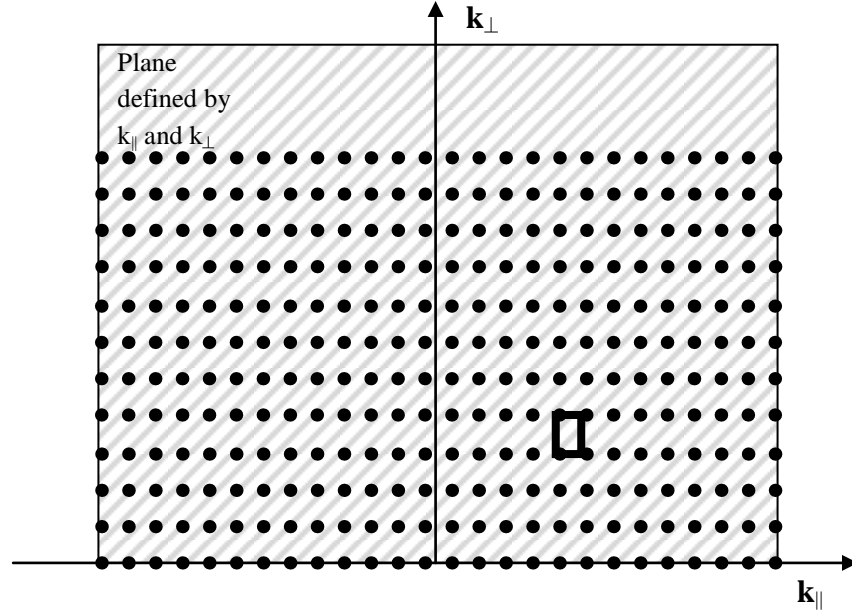


Figure 3.14 Choosing lines of constant k_{\parallel} for different k_{\perp} values in order to sweep a slice through the plane defined by k_{\parallel} and k_{\perp} vector. The band projection of the second type described in the text is obtained by replacing the k_{\perp} value with the energy value of a band and repeating the calculation for all the bands. The small rectangle from the figure denotes a quad that is rendered by the computer graphic hardware.

In order to obtain the map of the projection of the bands, the k_{\perp} value is simply replaced by the energy values given by the theoretical model for the given k points. Four adjacent point are forming a rectangle (showed as a small rectangle in **Figure 3.14**), and all the points chosen to calculate the projection are forming a large array of rectangles. For the computer graphics hardware, the equivalent of a rectangle is called quad. Giving as an input to the graphic card hardware the described array of quads and removing the light calculation, the result is an image map of the band projection. The term projection can be explained by the fact that the k_{\perp} values are simply forgotten when building the quads. The advantage of using the modern computer graphic hardware instead of making use of standard processor routines when creating the image map is speeding up the calculation time by at least one order of magnitude.

3.9. Initial and final state width effects

Up to this point, the initial and final states were considered to be infinitesimally narrow. The result of this approximation was leading to surfaces and contours. The advantage is that it is relatively fast to generate them and they contain precious information that can be directly compared with an ARUPS experiment. On the other hand, the information regarding the intensity of the photoemitted current is lost. Just to fill part of this gap, this subchapter is dealing with the effects of the initial and final state widths.

As shown in reference (26), it is physically reliable if when simulating the photoemission process one is choosing a width of the initial state around a value of 0.1 eV. The width of the free electron final state can be chosen to have values of 2 eV, determined by the value of the mean free path of the photoemitted electrons (26). The approach of considering the widths of the initial and final state presented in this thesis is described in the following. The example of the (001) surface of a crystal having face center cubic structure was chosen to describe the method.

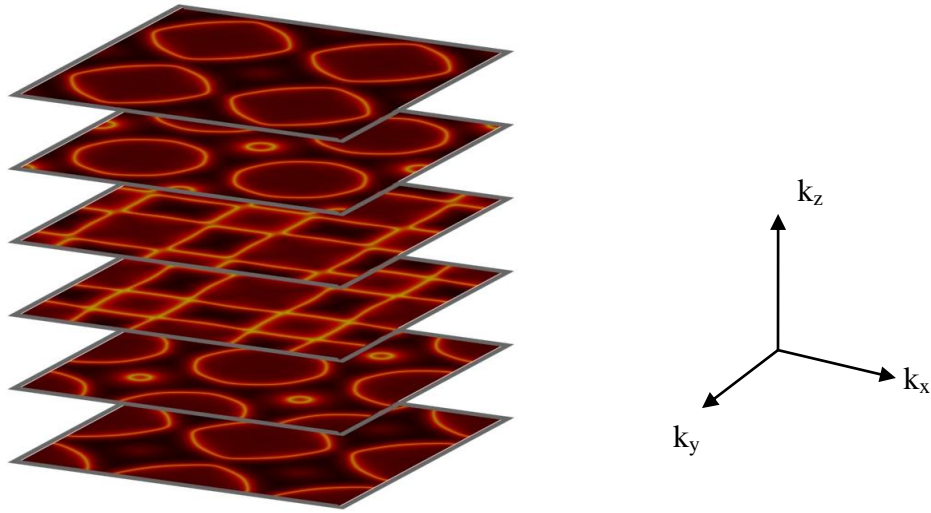


Figure 3.15 Intensity maps of the initial state taking into account a Gaussian width, calculated in planes parallel to the surface. The width value is exaggerated in order to have a better visibility in the illustration.

The first step of the implementation consists in generating image maps in planes parallel with the surface crystal, considering a Gaussian width of the initial state. Figure 3.15 illustrates the example of Cu(001) crystal, where only six planes are displayed. The value of the width has been chosen higher than 0.1 eV for the illustration, in order to

have a better image of the initial state width. After generating the image maps of the initial state width, a convolution with the width of the free electron final state is performed for each pixel of the maps generated and then all the maps are summed. The final image contains both the contribution of the initial and the final state.

3.10. Implementation

Along the time of this thesis, the first code that has been written has generically received the name FLAN (Fermi Level Analyzer). As input, the code is using the Fermi surfaces from reference (22). Shortly described, the task of FLAN was to perform final states spherical cuts of the Fermi surfaces in the repeated zone scheme of the Brillouin zones. No calculation of the initial states is done in FLAN, the Fermi surfaces are read from a virtual modeling language (WRL) format available from reference (22). FLAN has been completely included in a subsequent code called ELAN (Energy Level Analyzer). ELAN is performing advanced calculations of the initial state and also is fully including FLAN capabilities. Therefore, the implementation of ELAN is going to be described here.

ELAN was thought to be an independent application, not running as a macro of another software environment. The advantage of this approach consists in the fact that no additional software has to be purchased by the user and besides, the program consumes less computer resources. As programming language for developing the end user ELAN application, Borland Delphi TM has been chosen. Delphi is a Pascal-based programming language, with low-level escapes for experts. Being a popular programming language, rich literature posted by a large community can be found (27). The use of Visual Component Libraries (VCL) usually available with full source code is greatly simplifying the programmer work. ELAN makes use of two external VCL components. The TeeChart component (28) is used to display 2D charts, and TOGDraw (29) component is used for displaying 3D objects. The last component was modified in order to be able to use the latest OpenGL (30) capabilities. OpenGL (Open Graphics Library) is a standard specification defining a cross-language cross-platform API (Application Programming Interface) for writing applications that produce 3D computer graphics (and 2D computer graphics as well). The interface consists of over 250 different function calls, which can be used to draw complex three-dimensional scenes from simple primitives. OpenGL was developed by Silicon Graphics Inc. (SGI) in 1992

(30) and is popular in the video game industry, where it competes with Direct3D on Microsoft Windows platforms. OpenGL is widely used in CAD, virtual reality, scientific visualization, information visualization, flight simulation and video game development. Delphi fully incorporates the OpenGL headers required to use the OpenGL functions.

The energy eigenvalues of the generalized eigenvalue problem have been solved by using the *zhegv* function from LAPACK (23). A processor specific optimized library of LAPACK has been used. The optimized LAPACK library used is included in the Math Kernel Library (MKL) package of Intel (23).

The graphical user interface of ELAN is a MDI (Multiple Document Interface) application. In simple words, in an MDI application, more than one document or child window can be opened within a single parent window. Three main kinds of child windows have been chosen to make ELAN. A main control panel governs the user choice of which features to be calculated or displayed. The two other windows are dedicated to the 3D and 2D displaying of the results. Both the form containing the 2D or the 3D charts has its own set of chart specific controls. For space economy reasons, the main control form has been subdivided in four tabs. The first tab is dedicated to the calculation and displaying of isosurfaces. The second tab contains controls dedicated to the ARUPS experiment. The third tab of the control form contains elements that govern both display properties of the isosurfaces or the ARUPS experiment features. The fourth tab called “Tools” is dedicated to import/export features and to future implementations of possible extension of the program. At the top of the control form, one can choose which element and which band from the nine of the tight binding model should be taken into account in the program.

Each time the ELAN program is closed, it is saving most of the parameters displayed in the controls. Even the values of the windows positions are stored in order to be able to create the environment of a “project”.

An important part of the implementation is based in pure graphic hardware calculations. For example, displaying only triangles contained inside of a sphere can be obtained by time consuming clipping algorithms of the array of triangles, or one can make use of a powerful concept in the 3D graphics that is the texture mapping. Without entering too much into details, texture mapping represents a method of adding detail,

surface texture, or color to a computer-generated graphic or 3D model. Beside the red, green and blue components, the color can contain a fourth value that is the transparency (so called “alpha channel”). Beside the spatial coordinates, each vertex of a 3D object contains also the texture coordinates. If a 1D texture composed of two colors is applied to an object having spherical texture coordinates, the result is the object colored with a color inside of the sphere and other color outside of the sphere. If one of the colors has the alpha value zero, the result is equivalent with a spherical clipping of the object. The 3D rendering engine of OpenGL server can not perform at interactive rates a front to back triangle sorting of a large array of triangles. Therefore, whenever necessary, a front to back quick sorting algorithm of the 3D objects displayed has been implemented and it can be invoked by the user in order to obtain correct rendered images.

3.11. Results, discussion, experimental proof and conclusions

The main results of this chapter are presented in this section. The results are going to be presented and discussed in the order of the previous subchapters. At the end of this section, a short theory-experiment comparison for the angle resolved photoemission of the Cu(111) surface is going to be shown.

Figure 3.16 shows the constant energy surfaces of a Cu crystal for a binding energy of -2 eV. The election of the mentioned value of binding energy is to illustrate the capabilities of ELAN in displaying more than one isosurface at a binding energy not necessarily equal to zero. The panel on the left top side of Figure 3.16 represents a part of the control panel of ELAN. Once chosen the value of -2 eV for the binding energy, automatically the labels of the band numbers that have non zero isosurfaces are shadowed in green. One can chose to display the isosurfaces by activating the checkboxes below the band number labels. Each isosurface can receive its own color and transparency by invoking the color editor shown in the right side of Figure 3.17, by clicking in the colored panel placed below the band number checkboxes. The final result from the middle of Figure 3.17 was obtained by a subsequent invocation of sorting in a front to back order of the triangles composing the complex 3D object displayed.

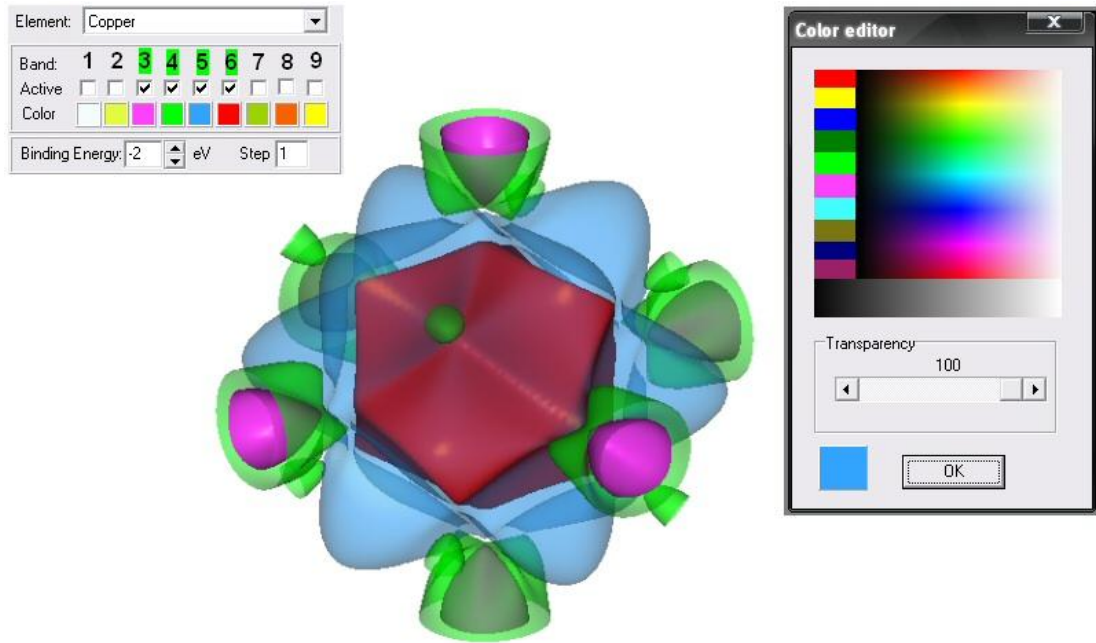


Figure 3.16 Constant energy surfaces of Copper for a binding energy of -2 eV (middle). The top left panel shows green shadowed labels for the bands having isosurfaces at the given binding energy. Each band can be controlled to be active in the 3D chart by using the checkboxes below the band number label. The color editor shown on the left side can be invoked by pressing the colored panel below the band label.

Changing the color or the transparency of a certain band has an immediate effect in the 3D plot. In case of using transparent objects, a subsequent invocation of sorting the objects in a front to back order has to be done. Any result displayed in the 3D window can be exported as an image or as a 3D object in virtual reality modeling language.

Figure 3.17 shows constant energy surfaces of Cu at binding energies of -2 eV (left), -1 eV (middle) and 0 eV (right) obtained by the radial projected method (colored in green) and by the marching cubes algorithm (colored in red). On a Pentium 4 processor with a clock rate of 3 GHz, the isosurfaces calculated with the projection surface method using a tessellation factor of 10 in each triangle from the irreducible Brillouin zone were computed in 30 milliseconds. The rendering process of the isosurfaces takes approximately the same time using a rather modest graphic card.

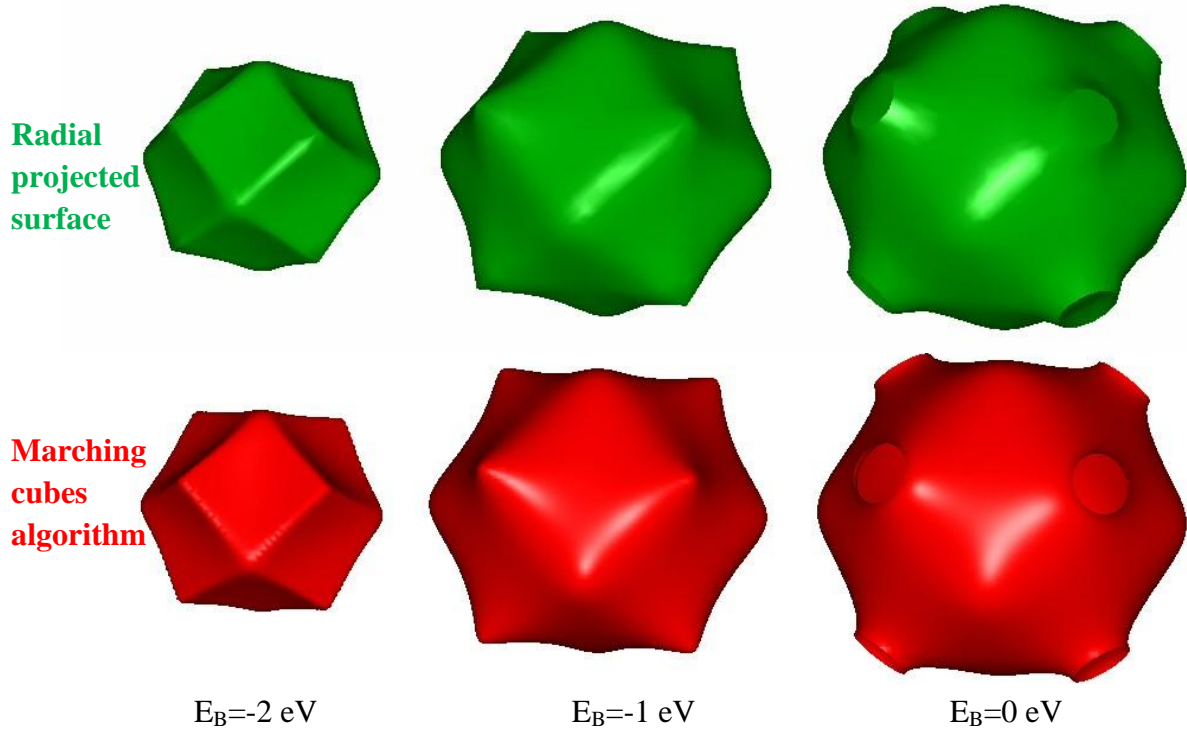


Figure 3.17 Constant energy surfaces of Copper at binding energies of -2 eV (left), -1 eV (middle) and 0 eV (right) obtained by the radial projected method (green) and by the marching cubes algorithm (red).

Regarding the marching cubes algorithm, the energy eigenvalues of the grid size of $40 \times 40 \times 40$ were computed in a time of around two seconds on the same machine. Once the grid is initialized, 50 milliseconds are enough to generate isosurfaces and to clip them at the Brillouin zone plane boundaries for any given binding energy. Both types of isosurfaces are properly indexed and scaled in ELAN in order to be use for subsequent calculations, as for example projected band gaps and spherical cuts.

The first type of approach to the ARUPS experiment described in this chapter was related with constant energy angular mapping of the electronic structure for a fixed photon energy. From the theoretical point of view, a comparison of the theoretical model with the experiment consists in performing a spherical cut of the constant energy surface in the repeated zone scheme (assuming a free electron like final state). Figure 3.18 shows the example of the Cu Fermi surface cut with a sphere of radius given by a photon energy of 21.2 eV. The projection of the cut for the (001) crystal surface is shown in the bottom right side of the image. The isosurface that is cut is restrained to those Brillouin zone orders that are touched by the final state sphere.

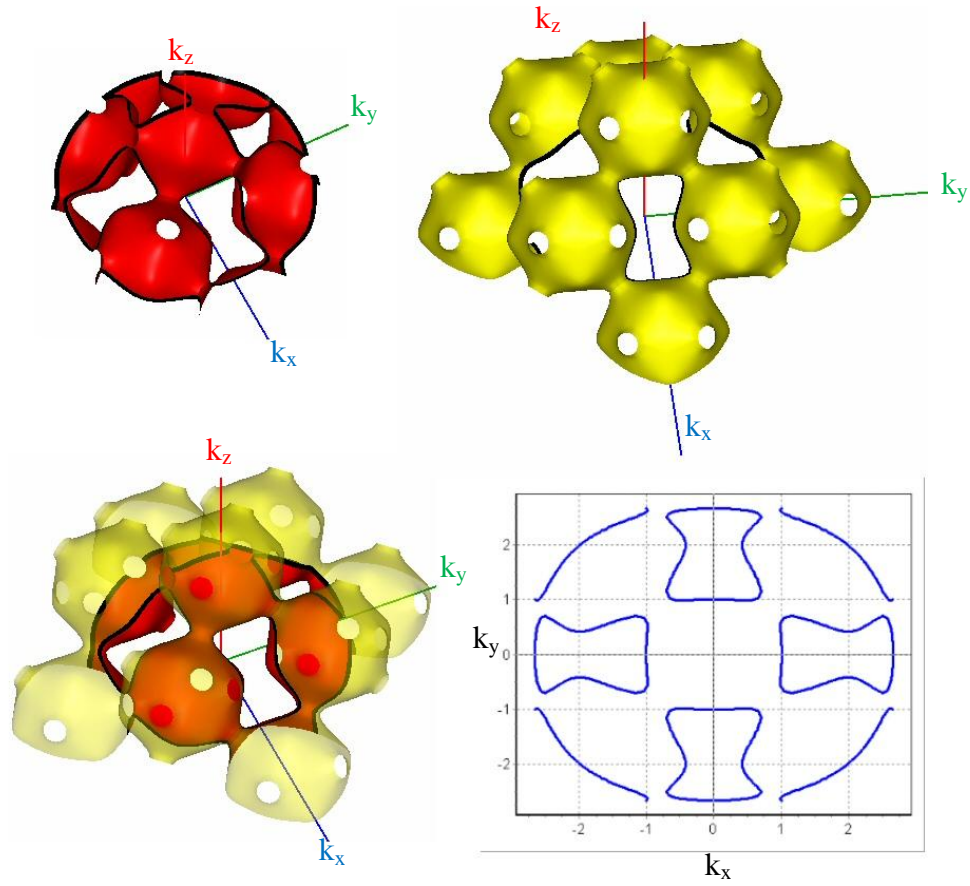


Figure 3.18 Spherical cuts of the Cu Fermi surface for a (001) crystal surface. The left top side of the image shows the isosurface part inside of the final state sphere from those Brillouin zone orders touched by the sphere. The right top image shows the part of the isosurface that is left outside, while the left down image shows all the isosurface colored with red (inside) and transparent yellow (outside). The right bottom side shows the cut projection onto the surface (001) plane in parallel momentum coordinates.

The left top side of Figure 3.18 shows in red the isosurface part inside of the final state sphere from those Brillouin zone orders touched by the sphere. The right top side shows the same, but outside of the final state sphere and colored in yellow. A combination of the two objects from the top of Figure 3.18 is resulting in the image from the left bottom side of figure. Additional transparency has been added to the region outside of the sphere in order to let the isocontour partially visible. The projection onto the surface (001) plane taken from the 2D chart is shown in the bottom right side. The momentum values are strictly correlated with the Copper lattice parameters, therefore making it possible a direct comparison with the experiment.

The right side of Figure 3.19 shows the band dispersion of the Cu(001) crystal along the (100) $k_{||}$ direction corresponding to a photon energy of 21.2 eV. Each band

represented as a red line is calculated separately, but computation times less than 3 milliseconds per band make the band dispersion interface working at interactive rates.

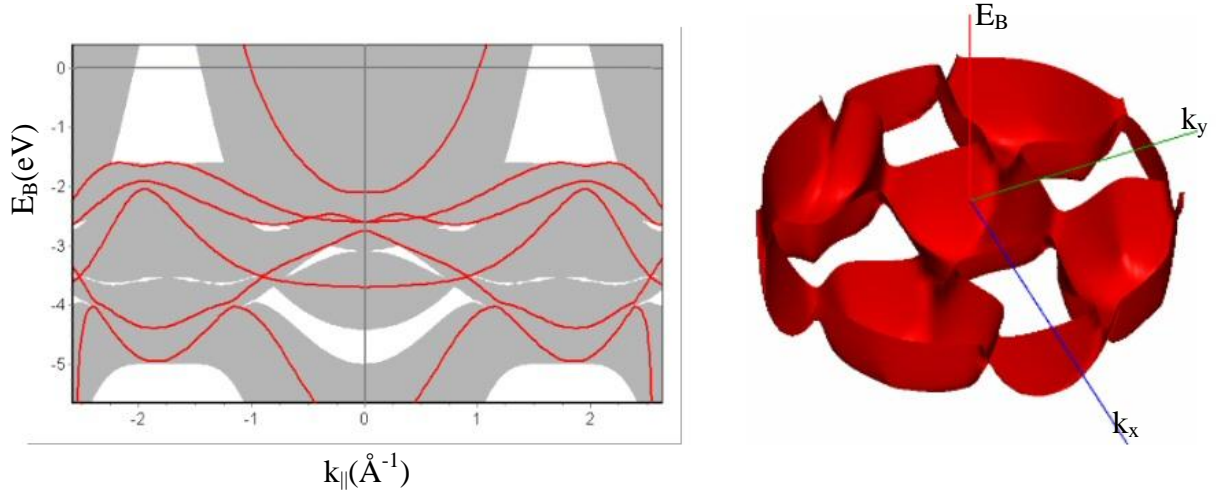


Figure 3.19 Left: band dispersion of Cu(001) crystal along (100) k_{\parallel} direction calculated for a photon energy of 21.2 eV. Each band displayed in red corresponds to a different band number, the band crossing the Fermi level is the band number 6. The band projection map has been added to illustrate the gap position. Right: The energy eigenvalues of band number 6 versus the two components of the parallel momentum, for the same value of photon energy of 21.2 eV.

The band projection map has been added to the chart from the left side of Figure 3.19 in order to illustrate the gap position along the (001) direction. The right side of Figure 3.19 shows the position in k_{\parallel} coordinates of the energy eigenvalues of band number 6 (the one that crosses the Fermi level) for the same photon energy of 21.2 eV. The 3D object has been calculated as described in the band dispersion subchapter making use of 100 parallel lines in k -space. The total computational time is around 5 seconds. A top view of the object from the right side is basically showing at which binding energy one can encounter the band number 6 in the occupied states for the given photon energy at a certain k_{\parallel} position.

The input for ELAN in order to calculate the band dispersion is given by the h , k , l corresponding to the direction of k_{\parallel} . These values should define a vector perpendicular to the surface normal. A surface rotation in the azimuthal plane is simulated by providing a rotational angle to the k_{\parallel} vector in the ARUPS tab of the control panel of ELAN.

Results of the projected band gaps have been showed already when describing the implementation of the method (Figure 3.13). As a remark in this section, it is convenient to underline the fact that typically it takes less than one second to achieve the maps from Figure 3.13. Moreover, since the maps are calculated by the limits from the 2D chart, any zoom is not provoking a pixelation effect if the projection map is recalculated.

As an example of the initial and final state widths effect, the same (001) face of the Cu crystal is illustrated. The photon energy used in calculation was 50 eV and the angular map corresponds to the Fermi level.

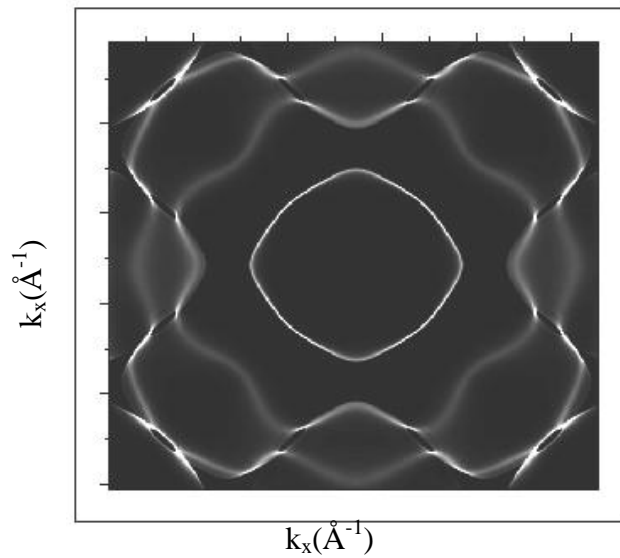


Figure 3.20 The effect of the initial and final states width calculated for Cu(001) for a photon energy of 50 eV.

Figure 3.20 shows the intensity map given by the calculation when taking 0.1 eV Gaussian width for the initial state and 2 eV width for the final state for a photon energy of 50 eV. The central contour is much more intense because during the projection more states have the same k_{\perp} value for the same k_{\parallel} value.

The last result of this section consists in an experimental confirmation of the reliability of the theoretical model under discussion. Due to the good experimental confirmation already known for the Cu tight binding parameters (21), a fast check of the experimental ARUPS data of Cu(111) face was investigated. The Cu(111) face presents no surface reconstruction, which makes it a good candidate to check the implemented extension of the tight binding model.

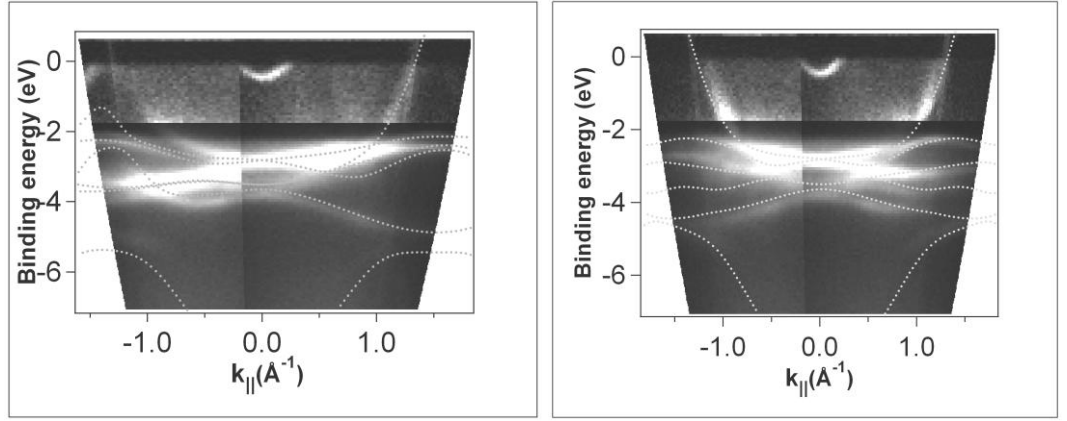


Figure 3.21 Cu(111) band dispersion along $\langle 1\bar{1}0 \rangle$ ($\bar{\Gamma}\bar{M}$) and $\langle 11\bar{2} \rangle$ ($\bar{\Gamma}\bar{K}$) directions (greyscale) and the theoretical plot (dotted lines)

Good agreement between the theory and the experiment can be seen in Figure 3.21, which shows the greyscale image of band dispersion along $\bar{\Gamma}\bar{M}$ and $\bar{\Gamma}\bar{K}$ surface directions (greyscale) and the dot lines representing the theoretical calculated position of the bands. The tiny parabolic band at $k_{||}=0$ is the Cu(111) surface state from the bulk L-gap.

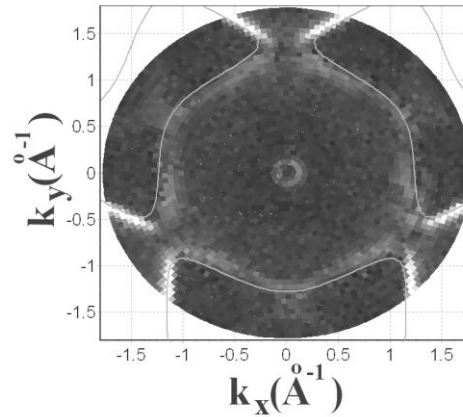


Figure 3.22 Experimental Cu(111) Fermi surface measured with HeI $_{\alpha}$ (greyscale) and the calculated Fermi surface cuts (contour).

Figure 3.22 shows the good agreement between the Fermi surface experimental cut for $h\nu=21.2$ eV and the theoretical cut (lines).

Several conclusions are summarized here. A comprehensive energy band calculation starting from a TB model has been implemented. The computations make use of precalculated TB parameters obtained to fit more precise calculations. From these

calculations, constant energy surfaces, band structure along high symmetry directions and projected bulk band plots are obtained in very reasonable amounts of time, even three orders of magnitudes faster than existing published work. Good agreement has been found with the Cu(111) measurements. As a final remark, without the need of cluster computers or supercomputers, it was possible to develop a user friendly code that brings a theoretical model in the hands of an ARUPS experimentalist.

CHAPTER
FOUR

4. Phase transitions and surface electronic structure of Pb/Cu(100)

Phase transitions in ultrathin films provide insight in the physical phenomena typical of low dimensional materials, with a potential impact in the physics of materials at nanometer scale. Due to these reasons, surface reconstructions and phase transitions have received ample theoretical and experimental attention in the past (31) (32) (33). The case of 2D is even more interesting because fluctuations play a much more important role than in 3D. 2D phase transitions triggered by a gain in electronic energy are a subject of current interest (34) (35) (36) (37). The most important example of this kind is the formation of a charge density wave, a macroscopically coherent state with very interesting properties (38).

The growth of submonolayer amounts of Pb on Cu(100) has deserved ample attention in the past (39) (40) (41) (42) (43) (44) (45) (46) (47) (48) (49) (50). In the following, a brief enumeration of the most relevant properties of this system is presented. For a more detailed account I refer the reader to Refs. (49) (50). Pb on Cu(100) is a lattice-mismatched system. Pb and Cu are immiscible in the bulk, but Pb atoms intermix with Cu in the earliest stages of the growth (46). Furthermore, Pb acts as a surfactant for the epitaxial growth on Cu (45). Finally, several different surface structures with intriguing properties are observed in the submonolayer coverage range (39) (40) (41) (42). As a result of this previous research, it is well established that Pb grows on Cu(100) following a Stranski-Krastanov mode. A dense Pb layer is completed for a coverage of 0.6 ML. Further Pb deposition gives rise to island formation. Three different surface reconstructions are observed for coverages below 0.6 ML: $c(4\times 4)$ (for 0.375 ML), $c(2\times 2)$ (for 0.5 ML) and $c(5\sqrt{2}\times\sqrt{2})R45^\circ$ (for 0.6 ML). The atomic model of these phases is shown in Figure 4.1. The $c(4\times 4)$ structure is interpreted as a Cu-Pb surface alloy with a Cu_4Pb_3 composition (47). On the contrary, the $c(2\times 2)$

reconstruction is due to a simple arrangement 0.5 ML of Pb atoms occupying every other Cu(100) hollow site (40) (41) (47). For a coverage range above 0.5 ML and below 0.6 ML, a $c(2 \times 2)$ phase with split superstructure spots is observed. The origin of this phase is the insertion of antiphase domain boundaries into the $c(2 \times 2)$ structure (40) (see Figure 4.1c). At a critical coverage of 0.6 ML, a regular distribution of linear domain boundaries is observed, characterized by the regular succession of three rows of Pb atoms occupying the same kind of hollow site (see Figure 4.1d). The long range order of this structure corresponds to a $c(5\sqrt{2} \times \sqrt{2})R45^\circ$ conventional unit cell (equivalent to a $\begin{pmatrix} 2 & 3 \\ 3 & 2 \end{pmatrix}$ structure) (42) (43) (44) (45). This surface phase has twofold symmetry, and therefore there are two orientational domains arranged with an angle of 90° to each others. All the three phases melt in the 500-570 K range (43) (44) (45) (46) (47) (48) (49) (50).

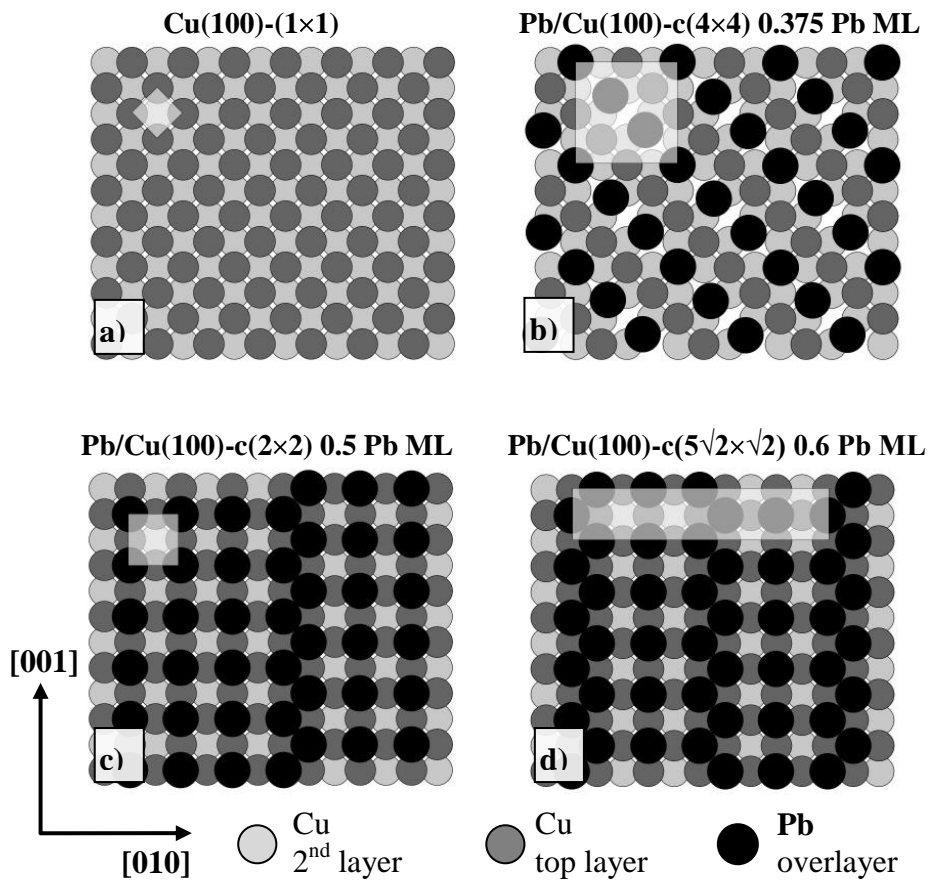


Figure 4.1 Literature atomic models of unreconstructed Cu(100) surface (a) and main phases of Pb/Cu(100) system (b, c and d). Structure and coverage are shown on top of the model. The unit cell of each structure is drawn as a gray rectangle.

Reconstructions of the type $(n\sqrt{2} \times m\sqrt{2})R45^\circ$ (primitive or centered) are commonly found on the (100) surfaces of noble metals for a variety of adsorbates. Several recent

studies have reported compelling evidences on the role of Fermi surface nesting and gapping in the stabilization of several surface phases of this family. In particular, it has been proposed that In/Cu(100)-(9 $\sqrt{2}\times 2\sqrt{2}$)R45° (51) (52), In/Cu(100)-(2 $\sqrt{2}\times 2\sqrt{2}$)R45° (53), and Sn/Cu(100)-p(3 $\sqrt{2}\times \sqrt{2}$)R45° (54) are stabilized by a gain in electronic energy with respect to a high temperature phase of simpler structure. The (n $\sqrt{2}\times m\sqrt{2}$)R45° phases are interpreted as a surface charge density wave in the strong electron-phonon coupling regime (51) (52) (53) (54).

The first part of this chapter of the thesis is dealing with a reversible phase transition of the (5 $\sqrt{2}\times \sqrt{2}$)R45° phase of Pb/Cu(100) when annealing to temperatures higher than the room temperature.

The second and main part of this chapter is treating the evolution of the surface electronic structure of the system for a Pb coverage range between 0 and 0.6 ML. Special attention has been devoted to the surface states observed in the projected band gaps of the Cu(100) surface. During the formation of several phases with an increasing Pb coverage, forbidden electronic states for the bulk substrate but not for the surface are gradually filled by electrons. The filling of these electronic states takes place gradually and the surface reconstructions put their fingerprint to the electronic structure and vice versa. Due to the rich variety of surface reconstructions, the Pb/Cu(100) system is a good model system for studying the interplay between the surface crystalline and electronic structure. Secondary photoemission effects like diffraction Umklapps are carefully considered at the time of analyzing the data. Each main phase described before presents its own electronic structure peculiarities, which will be analyzed separately.

4.1. Surface phase transitions of Pb/Cu(100) system

Surface reconstructions of the Cu(100) surface covered with submonolayers amount of In or Sn are undergoing phase transitions at temperatures in the range of 300-450 K (53). The transition was associated with the contribution to the energy balance of the system given by the surface electronic structure. In these interfaces it was observed a significant energy gain of the surface electronic structure between the high-temperature ungapped and low-temperature gapped phases. These observations are implying that the observed phase transitions can be classified as Peierls charge density wave phase transitions. Moreover, it is expected that the case of Sn and In is not an isolated one, but

it can be generalized for heavier p-block metals on top of the Cu(100) surface. The main goal of investigating the phase transitions of the Pb/Cu(100) system was to identify a reversible phase transition in order to study the contribution of the electronic structure and the electronic properties of the phases involved in the transition.

The most promising phase that undergoes CDW transitions is observed for 0.5 ML of deposited d-metal. In the case of Sn, a $p(3\sqrt{2}\times\sqrt{2})R45^\circ$ phase obtained by depositing 0.5 ML Sn at room temperature undergoes a reversible phase transition to a $c(2\times 2)$ phase at a temperature of 360 K. The phase transition is reversible and ARUPS studies of the electronic structure strongly support that the transition is due to a CDW stabilization. In the case of In, a $p(9\sqrt{2}\times 2\sqrt{2})R45^\circ$ at 0.5 ML In undergoes a phase transition to a $c(2\times 2)$ phase at a temperature of 350 K. Same interpretation as for the Sn case has been given to the In case. A recent report of Aruga (53) is stating that no other results have been reported for the case of Pb/Cu(100).

The situation of Pb for a coverage of 0.5 ML is different from the Sn and In cases. Already at room temperature the structure is a $c(2\times 2)$ phase, which is the high temperature phase for the Sn and In. A first idea was to identify a phase transition by cooling down the system. With the available technical equipment it was possible to cool down to a temperature of 70 K using liquid He at the facilities from the beamline BL33 from MaxLab in Lund. No surface phase transitions were observed. The possibility of a transition at lower temperatures can not be discarded, especially because the surface electronic structure of the $c(2\times 2)$ surface strongly resembles the one of $c(2\times 2)$ Sn/Cu(100). The results of the electronic structure of the $c(2\times 2)$ surface are going to be presented in the following subchapters.

The LEED patterns of the room temperature phases of the Pb/Cu(100) system for a coverage range between 0 and 0.6 ML are shown in Figure 4.2.

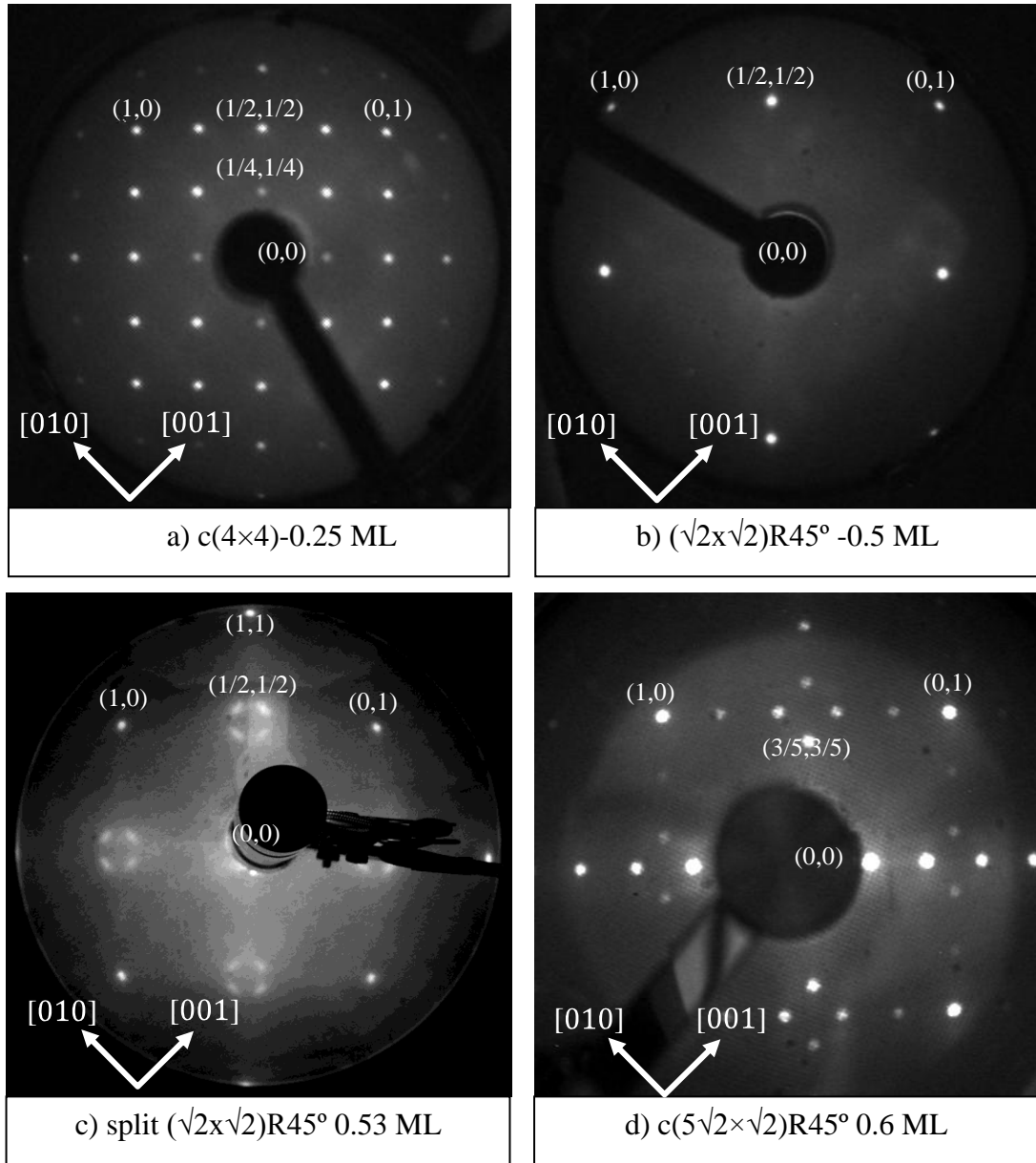


Figure 4.2 LEED patterns of the room temperature phases of the Pb/Cu(100) system for a coverage between 0 and 0.6 ML. The phase structure and the coverage are written at the bottom of the LEED images. The electron energy used was 70 eV.

The phases shown in the Figure 4.2 have been obtained by Pb deposition on the Cu(100) substrate held at room temperature. Very precise deposition times of a well calibrated evaporator are necessary to obtain pure phases. Even if it is not the case for the phases that were measured, it is convenient to point that the Pb is sublimating from the surface at temperatures higher than 700 K, making it possible in this way to obtain a certain phase by evaporating slightly more Pb and then by sublimating the extra amounts by annealing for short periods of time at temperatures of around 700 K.

In an extensive study of the phases observed at different coverages and temperatures, we identified a phase transition for the $c(5\sqrt{2}\times\sqrt{2})R45^\circ$ structure at a coverage of 0.6 ML.

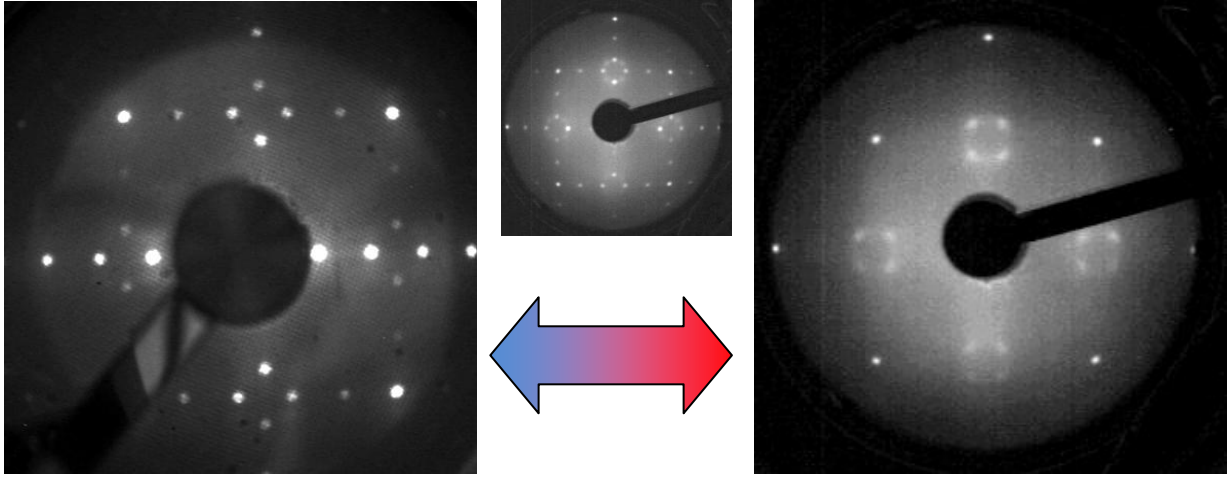


Figure 4.3 LEED patterns at 85 eV primary energy for 0.6 ML of Pb on Cu(100) at 300 K (left, $c(5\sqrt{2}\times\sqrt{2})R45^\circ$ phase), and at 450 K (right, split $c(2\times 2)$ phase). The middle pattern corresponds to a temperature right on the transition edge where both phases coexist.

When annealing the $c(5\sqrt{2}\times\sqrt{2})R45^\circ$ structure at a temperature of 450 K, a sharp transition takes place to a split $c(2\times 2)$ phase. Figure 4.3 shows the LEED patterns at 85 eV primary energy for 0.6 ML of Pb on Cu(100) at 300 K (left, $c(5\sqrt{2}\times\sqrt{2})R45^\circ$ phase), and at 450 K (right, split $c(2\times 2)$ phase). For the narrow temperature range where the phase transition takes place, a mixture of the two phases is visible in the LEED pattern (Figure 4.3 middle). The split $c(2\times 2)$ phase shows the same LEED pattern as the one obtained with less Pb coverage at room temperature. This transition has not been reported before, and it was believed that only a Pb overlayer melting is produced when annealing to high temperatures.

The LEED reflection orders that are defining the $c(5\sqrt{2}\times\sqrt{2})R45^\circ$ structure are completely disappearing after the transitions. Figure 4.4 shows the relative intensity of one of the specific reflections from the $c(5\sqrt{2}\times\sqrt{2})R45^\circ$ (blue line) phase and one from the split $c(2\times 2)$ phase (red line). The blue to red shadowed region is corresponding to an increasing temperature ramp where the transition from the low temperature phase to high temperature phase takes place. The red to blue shadowed rectangle indicates that the sample is cooling down and the transition is crossed in the other direction. The time

scaled horizontal axis of the left chart corresponds to a narrow temperature range of 20 K.

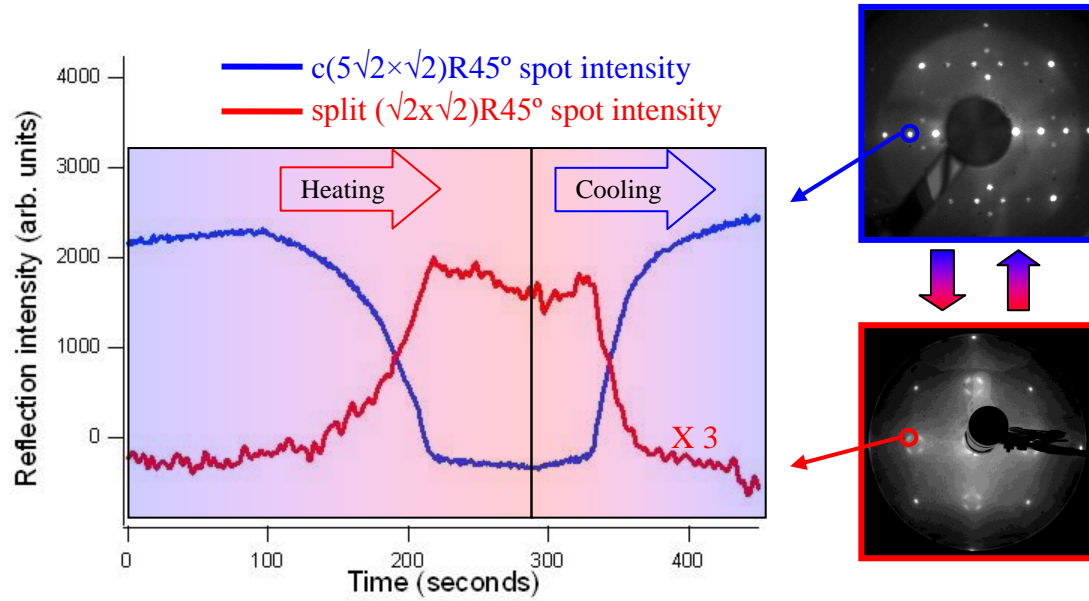


Figure 4.4 Reflection specific intensities of the $(5\sqrt{2}\times\sqrt{2})R45^\circ$ phase (blue line) and split $c(2\times 2)$ phase (red line).

The crystalline structure of both phases has been established from LEED I/V analysis (40) (41) (42), and it is reproduced in Fig. 4.15. In the case of the $c(5\sqrt{2}\times\sqrt{2})R45^\circ$ surface phase, Pb atoms still occupy hollow sites of the Cu(100) surface, as in the conventional $(\sqrt{2}\times\sqrt{2})R45^\circ$ phase at 0.5 ML. The $c(5\sqrt{2}\times\sqrt{2})R45^\circ$ reconstruction is generated by a periodic sequence of long-range ordered linear antiphase-domain boundaries. The linear antiphase domain boundaries define Pb stripes of three atomic rows width. The formation of antiphase domain boundaries permits to accommodate extra Pb atoms with respect to the $c(2\times 2)$ phase. Indeed, the formation of the domain boundaries is a way to compress the $c(2\times 2)$ structure. The linear domain boundaries run either along the (001) or the (010) directions, giving rise to the two different orientational surface domains mentioned before, as observed in the LEED pattern (Fig. 4.1).

A reliable interpretation of the role of the surface electronic structure in the $c(5\sqrt{2}\times\sqrt{2})R45^\circ$ phase to $c(2\times 2)$ phase transition is presented in the section 4.5, after describing general electronic structure properties of the system.

4.2. Projected band gaps of the Cu(100) surface

The knowledge of the substrate electronic structure properties is a necessary condition in order to understand the surface electronic structure. In general, surface electronic states are localized in the projected band gap of the crystal.

In the case of Cu, it is a relatively simple task to obtain the $E(k)$ localization of the projected band gaps for a specific surface. The electronic structure of Cu has been successfully described theoretically (21). A more than acceptable agreement between the theory and experiment exists (21), and parameters for the simplified tight binding model have been calculated (18). In this section, the $E(k)$ localization of the projected band gaps of Cu(100) is presented. The calculations have been performed making use of the code described in the second chapter of this thesis.

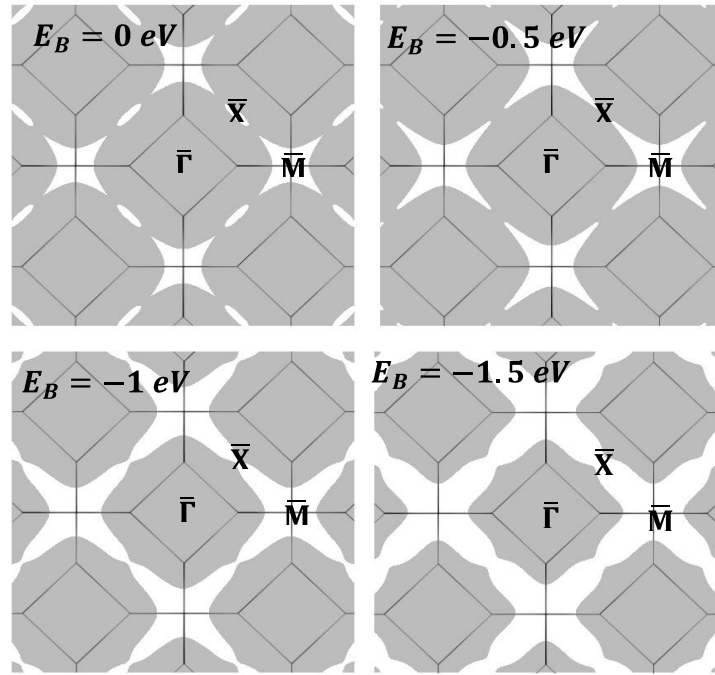


Figure 4.5 Projected momentum band gaps of Copper (grey shadowed) for the (001) surface at constant binding energies. The binding energy value is at the top left side of each image.

Figure 4.5 shows the momentum projected band gaps of the Cu(001) surface for several constant binding energies. At the Fermi level (0 eV binding energy), a star-like gap is observed at the \bar{M} point and an ellipse-like smaller gap is observed at the \bar{X} point. The \bar{M} gap is increasing in size when decreasing the binding energy, until the moment when a continuous gap joining \bar{M} and \bar{X} points is observed. At the \bar{X} point, the

gap is closing at a binding energy of -0.5 eV, then the gap reopens for lower binding energies.

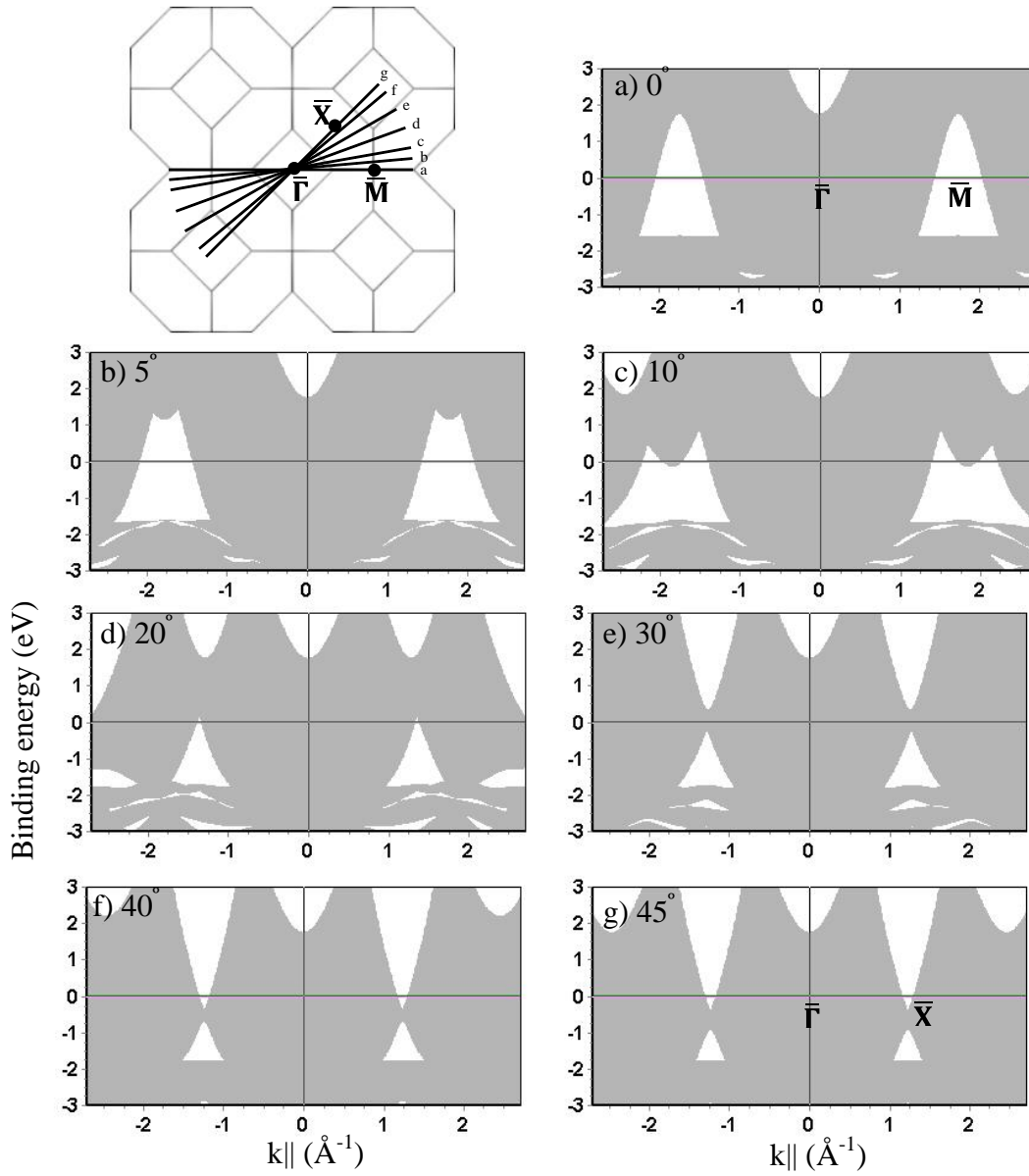


Figure 4.6 Projected band gaps structure along radial $k_{||}$ lines starting from $\bar{\Gamma} \bar{M}$ (a) and going to $\bar{\Gamma} \bar{X}$. The left top image shows the momentum position of the $k_{||}$ lines where the band projection has been calculated. The angle displayed in the images from a) to g) represent the off-angle with respect to the $\bar{\Gamma} \bar{M}$ direction.

Figure 4.6 shows the projected band gaps along several radial $k_{||}$ lines starting from $\bar{\Gamma} \bar{M}$ and ending along $\bar{\Gamma} \bar{X}$. Figure 4.6 a) shows the situation when $k_{||}$ runs along the $\bar{\Gamma} \bar{M}$ direction. Between the Fermi level and -1.9 eV, a large gap is observed at the \bar{M} point. When going to the $\bar{\Gamma} \bar{X}$ direction, this gap becomes smaller and shifts completely to the occupied states. On the other hand, a gap observed in the unoccupied states in Figure 4.6 c) for an off-angle of 10° off $\bar{\Gamma} \bar{M}$ direction is approaching the Fermi level upon

increasing the azimuthal angle. On the surface \bar{X} point, this gap is slightly entering in the occupied states, as shown in Figure 4.6 g).

4.3. Filling of a surface electronic band

Most of the properties of a material are directly correlated with its electronic structure. The importance of tuning electronic properties of a solid resides in the possibility of developing new materials related with technological applications. Due to its simplicity, the physics of low dimensional systems can provide a fundamental understanding of complex processes related with the electronic structure. The goal of this part of the thesis was to investigate the surface electronic structure dependence of Pb/Cu(100) system as a function of the Pb coverage between 0 and 0.7 ML. With an increasing Pb coverage, an increasing number of electrons from the Pb overlayer have to be accommodated in occupied states of the forming structure. A result of the deposition of Pb atoms on the surface can be the formation of allowed energy states in the Copper crystal band gaps. In some sense, the situation resembles the effect of doping of semiconductors. In semiconductors, the major effect of doping is the shifting of the Fermi level towards the energy band that corresponds to the dopant. No such an effect is expected for the deposition of a metal on top of another metal, due to the insignificant contribution of surface electrons to the density of states at the Fermi energy with respect to the bulk contribution. Moreover, the surface electronic states confined on the surface of metals lie at projected band gaps of the substrate crystal. These states resemble the semiconductor situation, with the difference that the energy gap is not extending to all the possible values of k . If the value of the Fermi level is not affected, the effect that can be expected is a gradual filling of a surface state as a function of the adsorbate coverage. In the present study, special efforts are devoted to the projected band gap of Cu for the (100) surface around the \bar{M} point. This gap is going to be referred in the following as the \bar{M} gap.

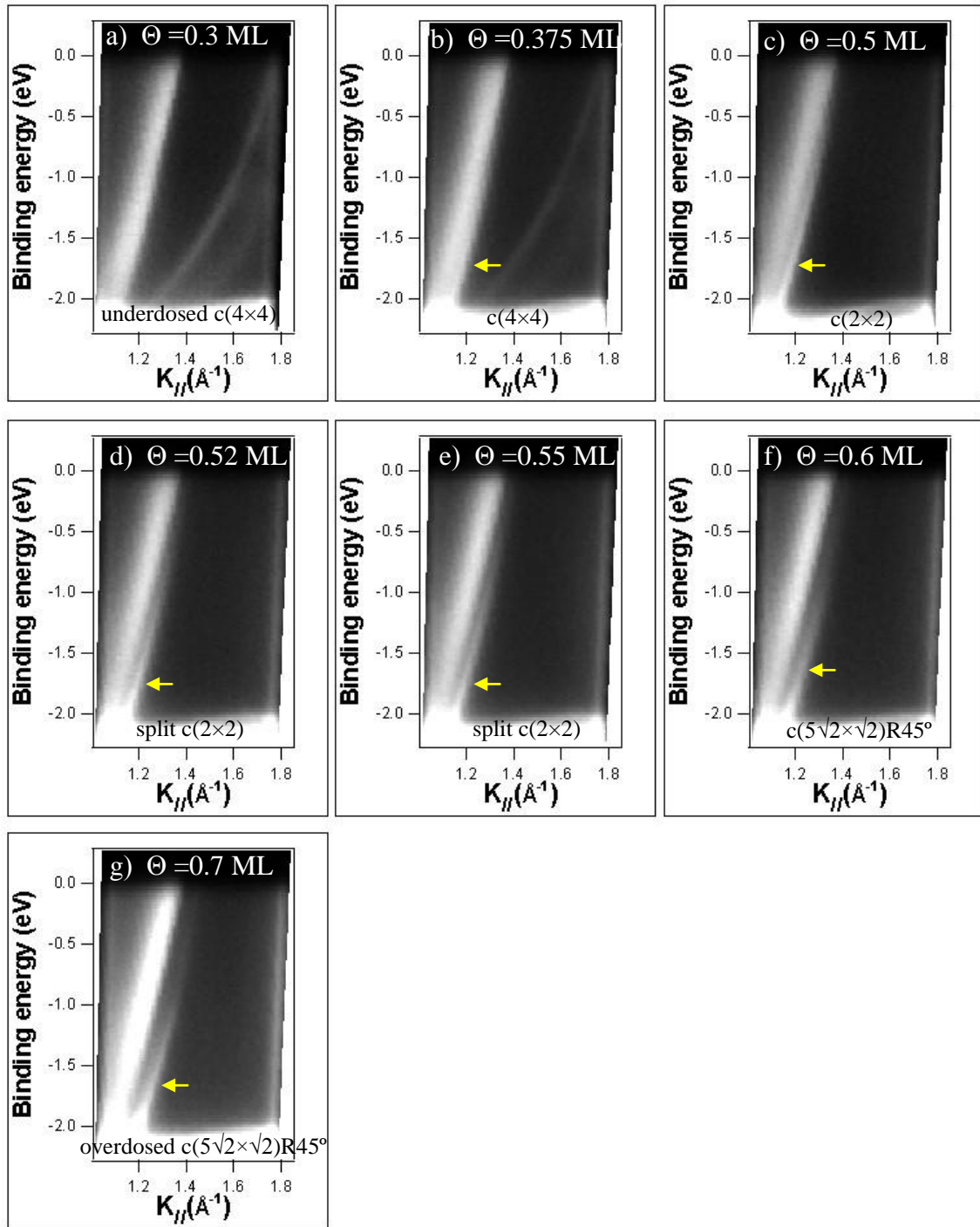


Figure 4.7 Sequence of ARUPS scans of Pb/Cu(100) along $\bar{\Gamma}-\bar{M}$ direction measured at 50 eV photon energy. The scans correspond to an increasing Pb coverage, starting from a coverage of around 0.2 ML (a) and ending with an overdosed $c(5\sqrt{2}\times\sqrt{2})R45^\circ$ phase at 0.7 ML (g). The broad band at low $k_{||}$ values that crosses the Fermi level at 1.35 \AA^{-1} is the bulk Copper sp band. The yellow arrow indicates a surface state.

Recent ARUPS studies focused on the Cu \bar{M} gap on In/Cu(100) (52) and Sn/Cu(100) (54) were identifying a surface state lying in this gap. This surface state has been assigned to have an adsorbate-substrate *sp*-like orbital origin (55) (56). Same type of state is observed for all Pb coverages in the submonolayer regime in the Cu(100) \bar{M} gap. Each coverage presents specific surface state features and this fact was leading to the idea of performing a precise description of this state as a function of coverage. None of the experimental chambers that were available for making ARUPS experiments could perform photoemission measurements while depositing. The sample had first to be transferred in front of the Pb evaporator and then moved back in the measurement position, leading in most of the cases to small positioning errors. This is not relevant when all measurements are made for a single surface or structure, but it is important when coverage-dependent changes are to be monitored. The effect of positioning errors is inaccuracies in the *k*-space mapping of a state. A precise mapping of the surface state observed along the $\bar{\Gamma}\bar{M}$ direction has been performed by making use of the fact that at certain photon energies the *sp*-band of Cu is close to the edge of the \bar{M} gap. In one *E(k)* window of a Scienta analyzer both the *sp* band of copper and the surface state can be recorded. If the same photon energy is used all the times, the position of the bulk copper *sp* band does not change. Therefore, by making the difference of the *k*-values of the surface state and the *k*-values of the bulk *sp* band it is possible to obtain an accurate positioning of the surface state in *k* space. The accuracy degree is basically as high as the analyzer angular resolution. The value of the photon energy required to have the *sp* band of Cu(100) close to the \bar{M} gap has been first calculated theoretically by using the code described in the second chapter. It was confirmed by the experiment, that 50 eV is a good value to have the *sp* band at the edge of the \bar{M} gap. The value of 50 eV photon energy is available only at synchrotron facilities and it has the advantage of the accurate location of the surface band, but on the other hand the angular resolution is less than at lower photon energies. Features of the fine structure of the surface state can be lost, but the main purpose of the measurement can be achieved.

Figure 4.7 shows the effect of increasing the Pb coverage on the band dispersion along $\bar{\Gamma}\bar{M}$ direction. All the scans have been measured at a photon energy of 50 eV. At low values of k_{\parallel} (left side of each image) one can observe the bulk *sp* band crossing the Fermi level at $k_{\parallel}=1.35 \text{ \AA}^{-1}$. Emerging from the edge of the \bar{M} gap defined by the *sp* band, a new state is gradually shifting to the right. From Figure 4.7 a) to g), the Pb

coverage is varied from 0.3 ML to 0.7 ML. Figure 4.7 a) corresponds to 0.2 ML Pb coverage and due to the fact that this coverage is slightly less than the one required to obtain a $c(4\times4)$ structure, it is called a “underdosed $c(4\times4)$ ”. At a close look to the data shown in Figure 4.7 a), the sp band presents an extra shoulder better contrasted for binding energies less than 1 eV. Figure 4.7 b) corresponds to a $c(4\times4)$ surface structure for a Pb coverage of 0.375 ML. The band dispersion shows now the shoulder out of the sp band, but still very close to it. For the $c(2\times2)$ surface structure at 0.5 ML Pb coverage, Figure 4.7 c) shows the surface state shifted to higher k_{\parallel} values compared with lower coverages. This behavior continues as coverage increases, as shown in Figure 4.7 d), e), f) and g) where the dispersions corresponding to 0.52 (d), 0.55 (e), 0.6 (f) and 0.7 (g) ML of Pb are plotted.

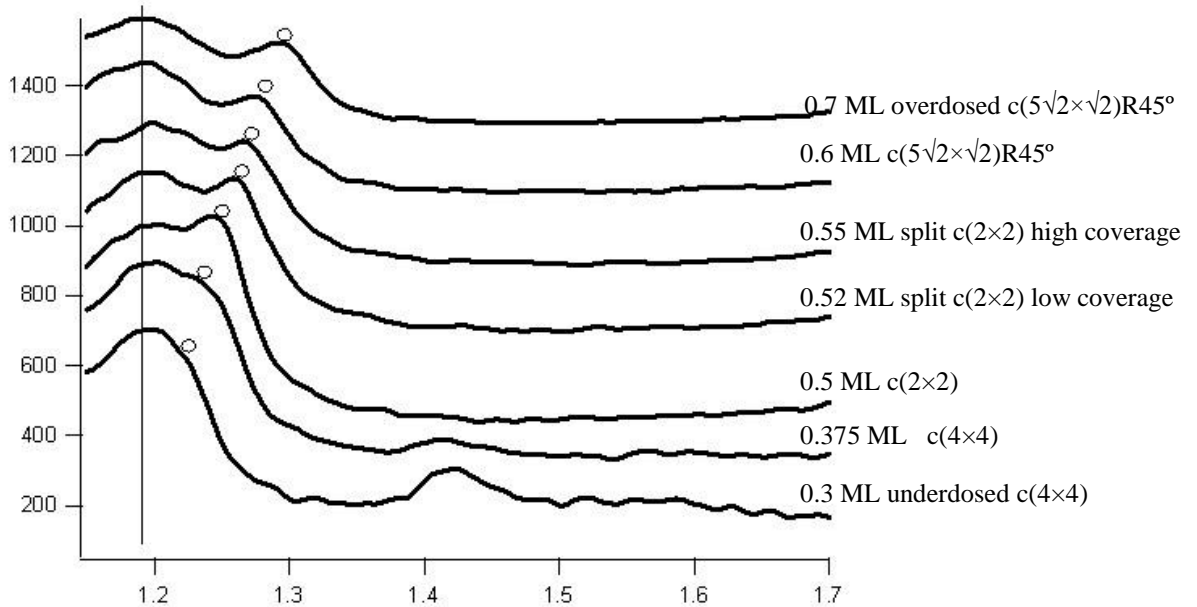


Figure 4.8 Momentum distribution curves at $E_B = -1.7$ eV from the scans shown in Figure 4.7. The bottom profile corresponds to the lowest Pb coverage of 0.3 ML. The circle on top of the surface state peak shows the shift of the state with increasing Pb coverage.

As it can be observed from Figure 4.7 and Figure 4.8, the shift of the surface state is gradual, indicating that the physical phenomenon corresponds to a novel type of electron band filling of a surface state.

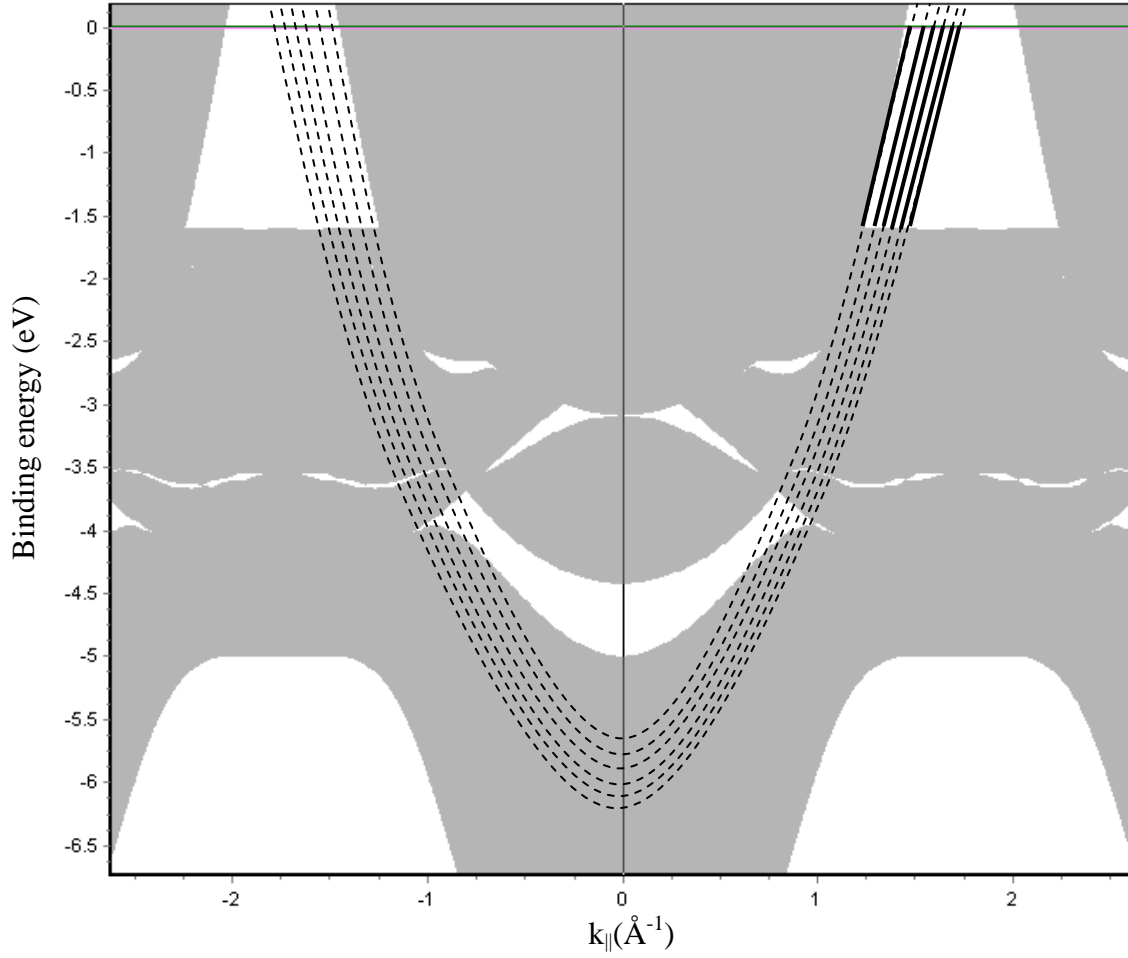


Figure 4.9 Illustration of the surface band filling situation for the Pb/Cu(100) system. The dotted lines from the parabolic dispersions along $\bar{\Gamma}-\bar{M}$ direction correspond to a theoretical free electron like surface state along the $\bar{\Gamma}-\bar{M}$ direction. Portions of this parabola represented with a bold black line within the \bar{M} gap correspond to the observed surface state.

An illustrative interpretation of the band filling situation is given in the Figure 4.9. A theoretical free electron parabolic dispersion has been fitted to the experimental dispersion of the surface state presented in the Figure 4.7. The data used for fitting the theoretical parabola are given by the dispersion of the surface state from the \bar{M} gap (data shown in Figure 4.7). Illustratively, it is represented with bold lines in Figure 4.9. For the lowest coverage of 0.2 ML, no points could be extracted due to the difficulty of locating the state on the sp band shoulder. The parabola parameters obtained by the fit are given in the table 4.1. The function used to fit the experimental dispersion was:

$$f(k_{||}) = Ak_{||}^2 + B$$

Phase	A	B
c(4×4)	2.85 ± 0.20	-5.75 ± 0.3
c(2×2)	3.03 ± 0.05	-6.01 ± 0.1
split c(2×2) low coverage	2.97 ± 0.07	-6.04 ± 0.1
split c(2×2) high coverage	3.07 ± 0.06	-6.18 ± 0.1
c(5√2×√2)R45°	3.02 ± 0.02	-6.26 ± 0.01
c(5√2×√2)R45° high coverage	2.89 ± 0.05	-6.30 ± 0.1

Table 4.1 Parameters of the free electron theoretical parabolas corresponding to the six values of the Pb coverage studied. The B parameter of the fitting gives the bottom of the parabola, and as it can be remarked in table 4.1, a gradual decrease is observed as coverage increases.

For the c(4×4) phase, the errors in fitting are large due to the fact that the surface state is quite close to the bulk sp band .

For the precise Pb coverages corresponding to the c(4×4) phase and the c(5√2×√2)R45° phase, extra features besides the analyzed surface state are observed. Solving these features requires the use of lower photon energy values, where the angular dispersion of the state gives better k_{\parallel} precision. This topic will be discussed in the following sections.

4.4. Electronic structure of the c(4×4) phase. Surface states and/or surface Umklapps.

The c(4×4) phase is obtained for a precise coverage of 0.25 ML of Pb. A thorough experimental procedure making use of a well calibrated Pb evaporator is required to achieve a uniform coverage of 0.25 ML.

The top of Figure 4.10 shows the surface Brillouin zones of the c(4×4) structure. Red circles corresponds to the $\bar{\Gamma}$ points of the c(4×4) phase and red lines to the zone boundaries of the same structure. The zone boundary of the unreconstructed (1×1) substrate is drawn with a dotted black line. The $\bar{\Gamma}$, \bar{M} and \bar{X} symmetry points of the unreconstructed (1×1) surface are also plotted. The gray shadowed area of Figure 4.10 is the bulk band projection of copper on the (001) surface at the Fermi level. The projection has been included as guidance to the regions of interests from the electronic structure point of view.

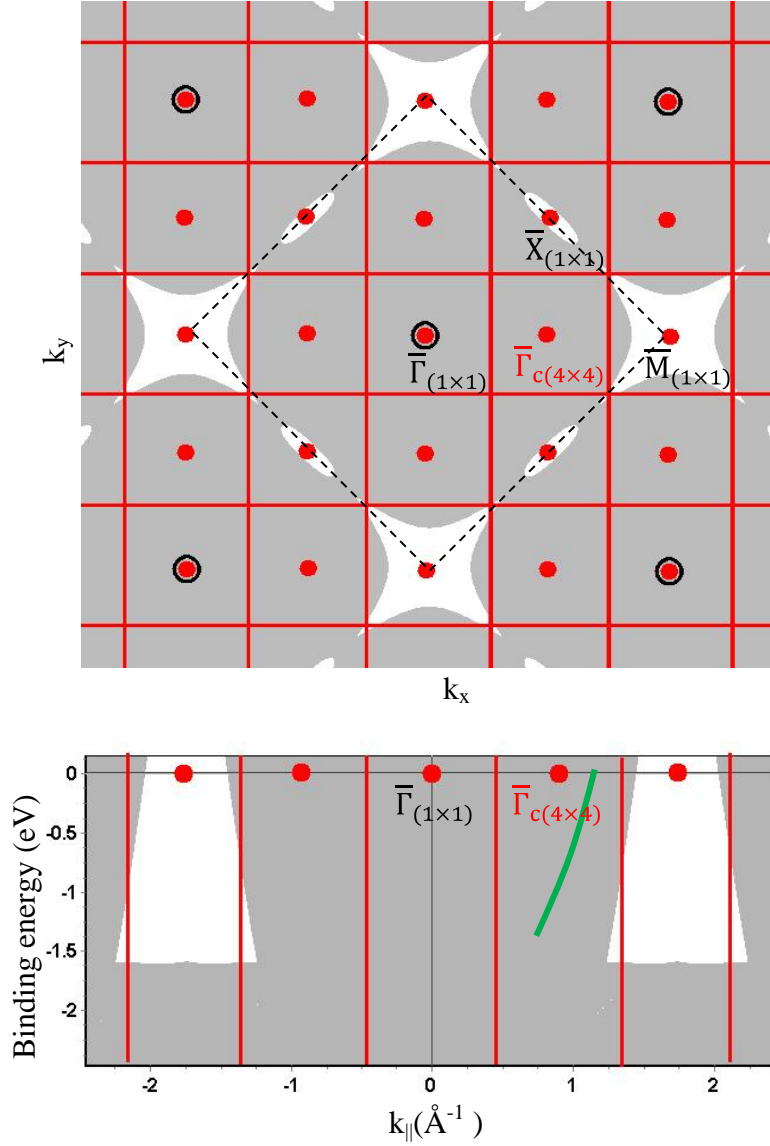


Figure 4.10 Top: Illustration of the surface Brillouin zones of the $c(4 \times 4)$ structure. The $\bar{\Gamma}$ points of the $c(4 \times 4)$ phase are marked with red points and the zone boundaries with red lines. The $\bar{\Gamma}$, \bar{M} and \bar{X} symmetry points of the unreconstructed (1×1) surface are also plotted. The dotted line corresponds with the zone plane boundary of the (1×1) substrate. The grey shadowed area gives the band bulk projection at the Fermi level. Bottom: $\bar{\Gamma}$ \bar{M} band gap plot together with the symmetry points of the $c(4 \times 4)$ structure. The green line correspond to the theoretical position of Cu sp band for 27 eV.

The bottom of Figure 4.10 shows the symmetry lines of the $c(4 \times 4)$ structure along the $\bar{\Gamma}$ \bar{M} direction in an $E(k_{||})$ plot. Red lines correspond to the Brillouin zone boundaries and black empty circles correspond to the (1×1) $\bar{\Gamma}$ points. The bulk Cu band projection shows the position of the projected band gap of the (001) surface with respect to the $c(4 \times 4)$ symmetry lines for the $\bar{\Gamma}$ \bar{M} direction. At the Fermi level, the $c(4 \times 4)$ zone edge is out of the \bar{M} gap. Between binding energies of -0.7 and -2 eV, the zone edge of the $c(4 \times 4)$ structure is within the \bar{M} gap.

The ARUPS measurements have been performed using a photon energy of 27 eV. More angular resolution is achieved than using 50 eV, and the bulk band of Cu stays away from the \bar{M} gap leaving a larger “clear” region for this photon energy. The Cu sp band for 27 eV is shown with a green line in the bottom side of Figure 4.10. The band has been calculated using the ELAN code explained in chapter 2.

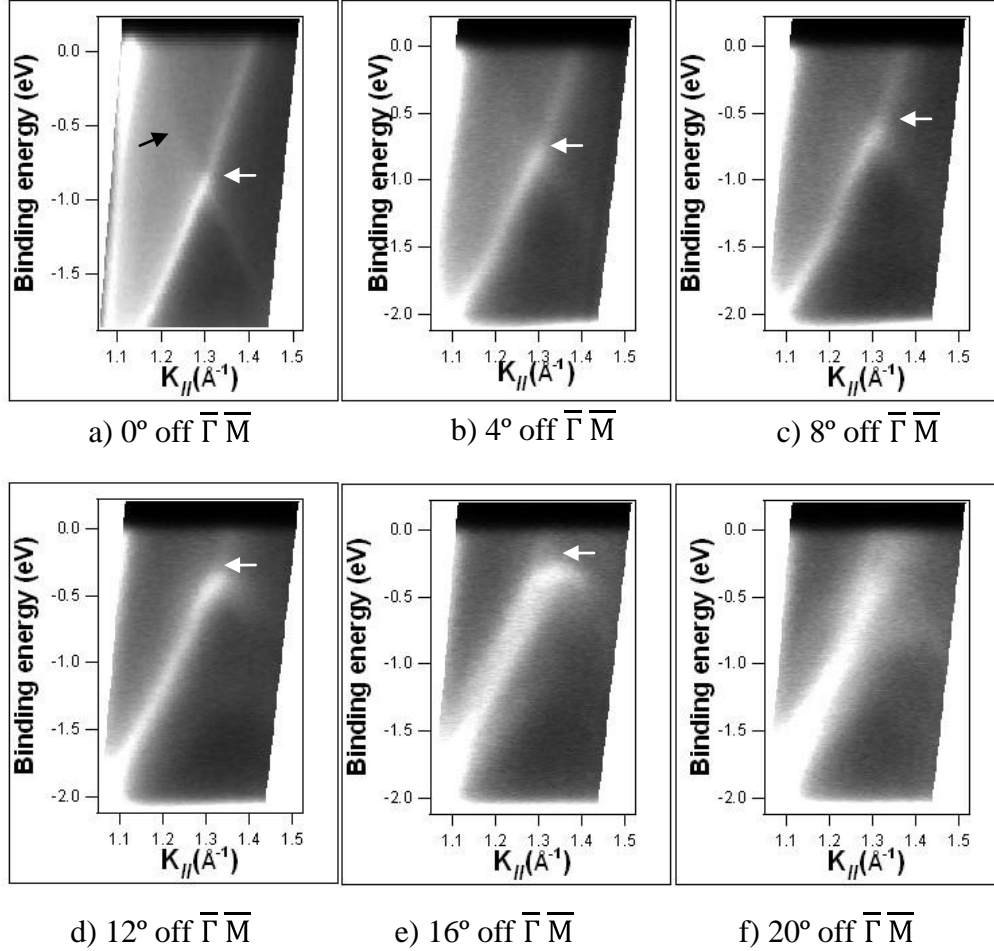


Figure 4.11 Band dispersion of c(4×4) Pb/Cu(001) system at 27 eV along several k_{\parallel} directions. The first image a) correspond to the $\bar{\Gamma}\bar{M}$ direction, and the subsequent images correspond an azimuthal angles of 4° (b), 8° (c), 12° (d), 16° (e), 20° (f) off $\bar{\Gamma}\bar{M}$ direction.

Figure 4.11 a) shows the $E(k_{\parallel})$ measurement along the $\bar{\Gamma}\bar{M}$ direction. The subsequent images are $E(k_{\parallel})$ scans at azimuthal angles off $\bar{\Gamma}\bar{M}$ as following: 4° (b), 8° (c), 12° (d), 16° (e), 20° (f).

Two states are observed in Figure 4.11. One is staying close to the edge of the \bar{M} gap and it crosses the Fermi level at $k_{\parallel}=1.35 \text{ \AA}^{-1}$. A weaker second band marked with a black arrow is also observed and it looks like a band backfolded with respect to the

zone boundary. The folding point marked with a white arrow in Figure 4.11 corresponds to k_{\parallel} points sitting along the zone boundary line of the $c(4\times 4)$ structure. An illustration of the k_{\parallel} position of these points is given in Figure 4.12.

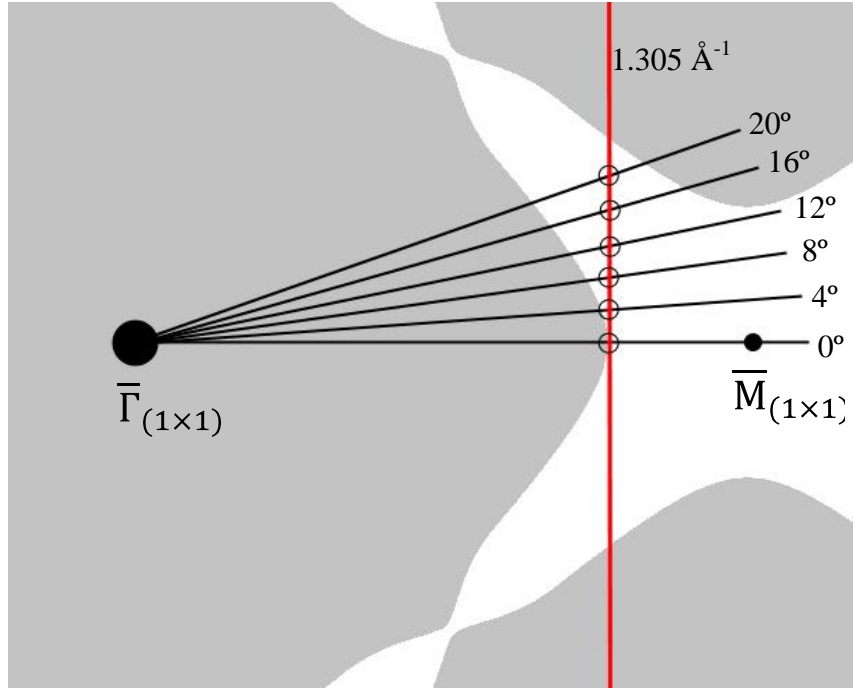


Figure 4.12 k_{\parallel} map of the backfolding points for the observed surface state. The folding points shown with black empty circles are following the zone boundary of the $c(4\times 4)$ structure (red line). The Cu band projection (grey shaded region) has been calculated at a value of -0.95 eV binding energy in order to underline the fact that the folded state is in the band gap all the time.

Two states were also observed in the \bar{M} gap for the $(3\sqrt{2}\times\sqrt{2})R45^\circ$ structure of the Sn/Cu(100) system (54). The second state was explained by the two-domain nature of the structure. The $c(4\times 4)$ structure is a single domain structure and an explanation based on the existence of multiple domains can not be valid. At a closer look, the band dispersion shown in Figure 4.11 is showing two folded band exposing a gap in the occupied states. The binding energy of the position of the gap is approaching the Fermi level as the azimuthal angle off the $\bar{\Gamma}\bar{M}$ direction is increasing. At an azimuthal angle of 16° off the $\bar{\Gamma}\bar{M}$ direction the gap is at the Fermi level (Figure 4.11 (e)). A gap at the Fermi level of a state that has mostly a free electron character is producing an overall decreasing in total electronic energy of the structure and therefore it contributes to the stabilization of the structure.

During the experiments, another state for the $c(4\times 4)$ structure in the \bar{M} gap has been observed. This state crosses the Fermi level at a $k_{\parallel}=1.79 \text{ \AA}^{-1}$ (Figure 4.13). In an

effort to explain the origin of this state, a detailed mapping at 50 eV photon energy has been performed and extra photon energies have been used to measure along $\bar{\Gamma}\bar{M}$ direction in order to check whether the observed state has a surface character. Figure 4.13 shows the band dispersion along $\bar{\Gamma}\bar{M}$ direction for three photon energies: 32 eV (a), 37 eV (b) and 50 eV (c).

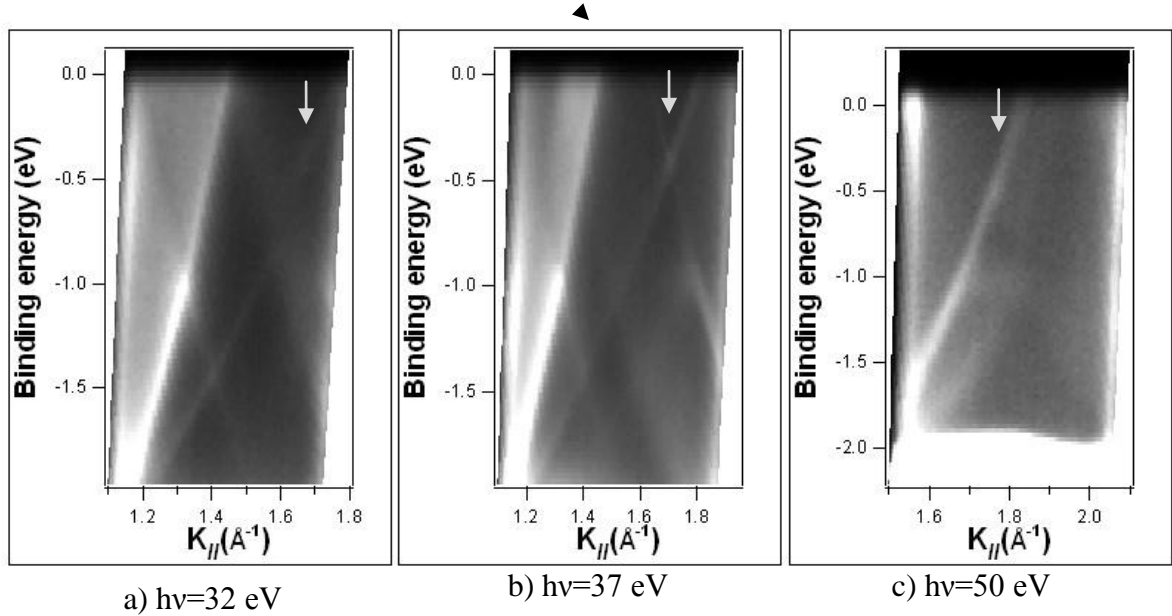


Figure 4.13 Band dispersion along GM direction for the c(4×4) Pb/Cu(001) phase measured at 32 eV (a), 37 eV (b) and 50 eV (c).

The state marked with a white arrow from the dispersion spectra shown in Figure 4.13 can be observed at a k_{\parallel} values around 1.6 \AA^{-1} for all the three photon energy used. The crossing of the Fermi level at $k_{\parallel}=1.79 \text{ \AA}^{-1}$ can be precisely measured at 50 eV photon energy. Two considerations are used in the following to explain the origin of this state. First, a semi empirical free electron like parabolic state is fold with the c(4×4) structure periodicity. The parabola parameters are took from Table 4.1. for 0.25 ML Pb coverage. Second, the possibility of an Umklapp diffraction effect of the bulk band with the c(4×4) symmetry is considered. The experimental mapping of the state observed in the middle of the \bar{M} gap corresponds with azimuthal scans for small angles off $\bar{\Gamma}\bar{M}$ direction and constant energy maps at the Fermi level shown in Figure 4.14 and Figure 4.15.

Figure 4.14 shows the band dispersion along $\bar{\Gamma}\bar{M}$ direction (a) for the c(4×4) Pb/Cu(001) phase measured at 50 eV. The other three plots correspond to k_{\parallel} directions off $\bar{\Gamma}\bar{M}$ direction of 1.5° (b), 3° (c) and 4.5° (d). Along the $\bar{\Gamma}\bar{M}$ direction, a single state

is observed and it crosses the Fermi level at $k_{\parallel}=1.79 \text{ \AA}^{-1}$. The origin of this state comes from the intersection of the semiempirical free electron like paraboloids centered at $\{1/4,1/4\}$ symmetry points. Once the sample is rotated only 1.5° , the band dispersions clearly shows two band (Figure 4.14 (b) corresponding to a k_{\parallel} direction 1.5° off GM direction). The value of this splitting behavior increases very fast with the angle of the azimuthal direction that is measured, Figure 4.14 c) and d) shows the bands dispersion along k_{\parallel} direction 3° and 4.5° off $\bar{\Gamma}\bar{M}$ direction. All the states can be explained by performing the intersections of the paraboloids mentioned before and in Figure 4.14 the theoretical bands are displayed with dotted lines.

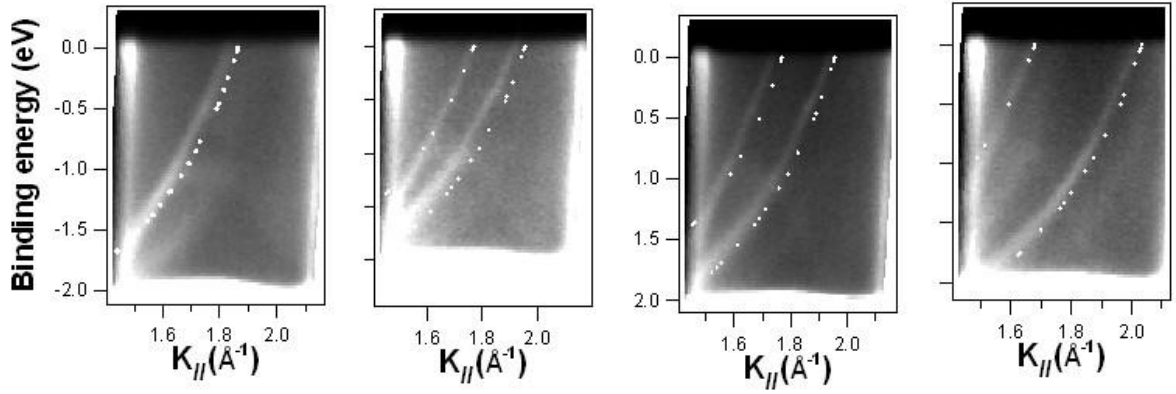


Figure 4.14 Band dispersion along $\bar{\Gamma}\bar{M}$ direction (a) for the $c(4\times 4)$ Pb/Cu(001) phase measured at 50 eV. The other three plots correspond to k_{\parallel} directions off $\bar{\Gamma}\bar{M}$ direction of 1.5° (b), 3° (c) and 4.5° (d). The dotted lines originate from the intersection of semiempirical free electron like paraboloids centered in $\{1/4,1/4\}$ symmetry points.

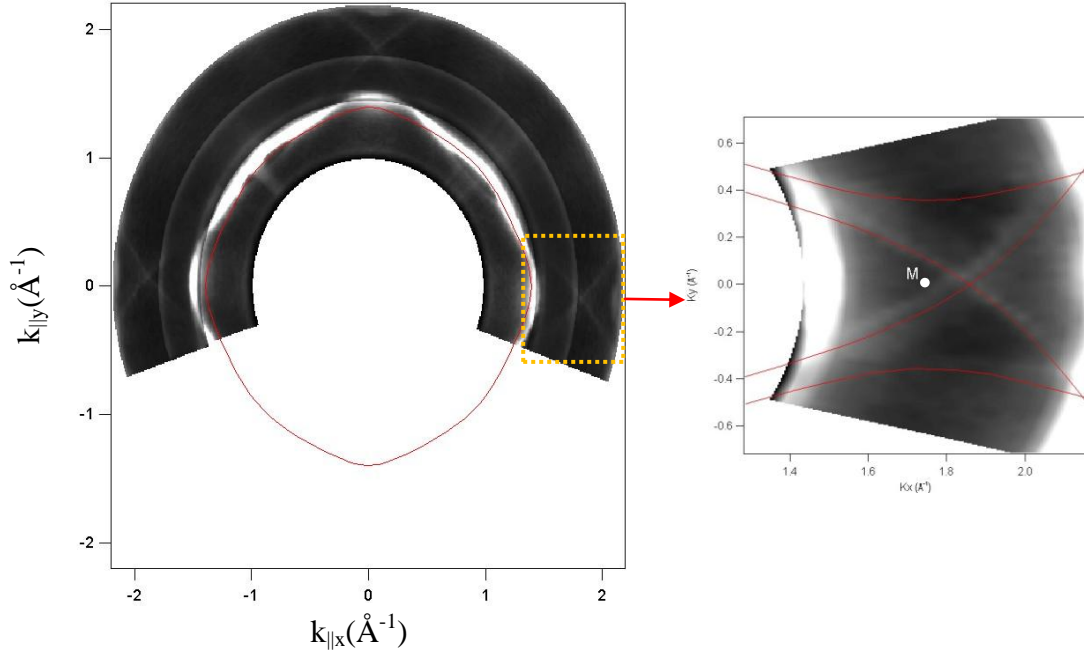


Figure 4.15 Left: Fermi surface slice of the $c(4\times 4)$ Pb/Cu(001) phase at a photon energy of 50 eV. Right: a zoom around the \bar{M} point of the Fermi surface.

Figure 4.15 is showing a slice of the constant energy map at the Fermi level for the $c(4\times 4)$ phase. The intense circular state corresponds to the bulk Cu sp band. The red line contour is the theoretical prediction of the sp band position from the tight binding model at a spherical cut corresponding to a photon energy of 50 eV. In the right side of Figure 4.15 it is shown a zoom in a window centered at the \bar{M} point. At 50 eV, the theoretical bulk cut at the Fermi level is almost indistinguishable from the value of the semiempirical free electron like state corresponding at 0.25 ML Pb coverage from the Table 4.1. Therefore, no clear distinction between a possible Umklapp phenomena and a surface state can be made for 50 eV photon energy. Translating the red contour to the $c(4\times 4)$ symmetry points, a satisfactory fit of the experimental data can be achieved (Figure 4.15 right).

4.5. Electronic structure of the $c(5\sqrt{2}\times\sqrt{2})R45^\circ$, $c(2\times 2)$ and split $c(2\times 2)$ phases and the role of the electronic structure in the $c(5\sqrt{2}\times\sqrt{2})R45^\circ$ to split $c(2\times 2)$ phase transition

In this subchapter, the electronic structure of the $c(5\sqrt{2}\times\sqrt{2})R45^\circ$, $c(2\times 2)$ and split $c(2\times 2)$ phases is described. Moreover the role of the electronic structure in the phase transition from the $c(5\sqrt{2}\times\sqrt{2})R45^\circ$ phase to the split $c(2\times 2)$ phase (described in the first subchapter) is going to be analyzed and discussed.

Figure 4.3 has shown the LEED patterns of the $c(5\sqrt{2}\times\sqrt{2})R45^\circ$ (fig 4.1 (d)) and the split $c(2\times 2)$ (fig 4.1 (b)) phases. The atomic model of both phases has been established from LEED I/V analysis (40) (41) (42), and it is reproduced at bottom of Figure 4.16. In the case of the $c(5\sqrt{2}\times\sqrt{2})R45^\circ$ surface phase, Pb atoms still occupy hollow sites of the Cu(100) surface, as in the conventional $c(2\times 2)$ phase at 0.5 ML. The $c(5\sqrt{2}\times\sqrt{2})R45^\circ$ reconstruction is generated by a periodic sequence of long-range ordered linear antiphase-domain boundaries. The linear antiphase domain boundaries define Pb stripes of three atomic rows width. The formation of antiphase domain boundaries permits to accommodate extra Pb atoms with respect to the $c(2\times 2)$ phase. Indeed, the formation of the domain boundaries is a way to compress the $c(2\times 2)$ structure. The linear domain boundaries run either along the (001) or the (010) directions (see Fig. 1), giving rise to the two different orientational surface domains mentioned before, as observed in the LEED pattern (Fig. 5.1 (d)). The $\bar{\Gamma}$ points and the Brillouin zone borders for both $c(5\sqrt{2}\times\sqrt{2})R45^\circ$ domains are drawn in Figure 4.16 top left. The $c(2\times 2)$ phase has only one domain and the Brillouin zone is drawn in the right top side of Figure 4.16.

The band dispersion along $\bar{\Gamma}-\bar{M}$ direction of the split $c(2\times 2)$ high temperature phase has been measured using the facilities from the beamline BL33 from MaxLab, Sweden. The sample has been heated using current pulses, and only in the “off” time of the pulses the photoelectron counts have been recorded, avoiding in this way the influence of the magnetic field of the heating current on the spectra. Unfortunately, at the specified facility, the energy and especially the angular resolution is lower than at the APE beamline at Elettra, Italy, where the rest of the phases at room temperature have been measured with better resolution.

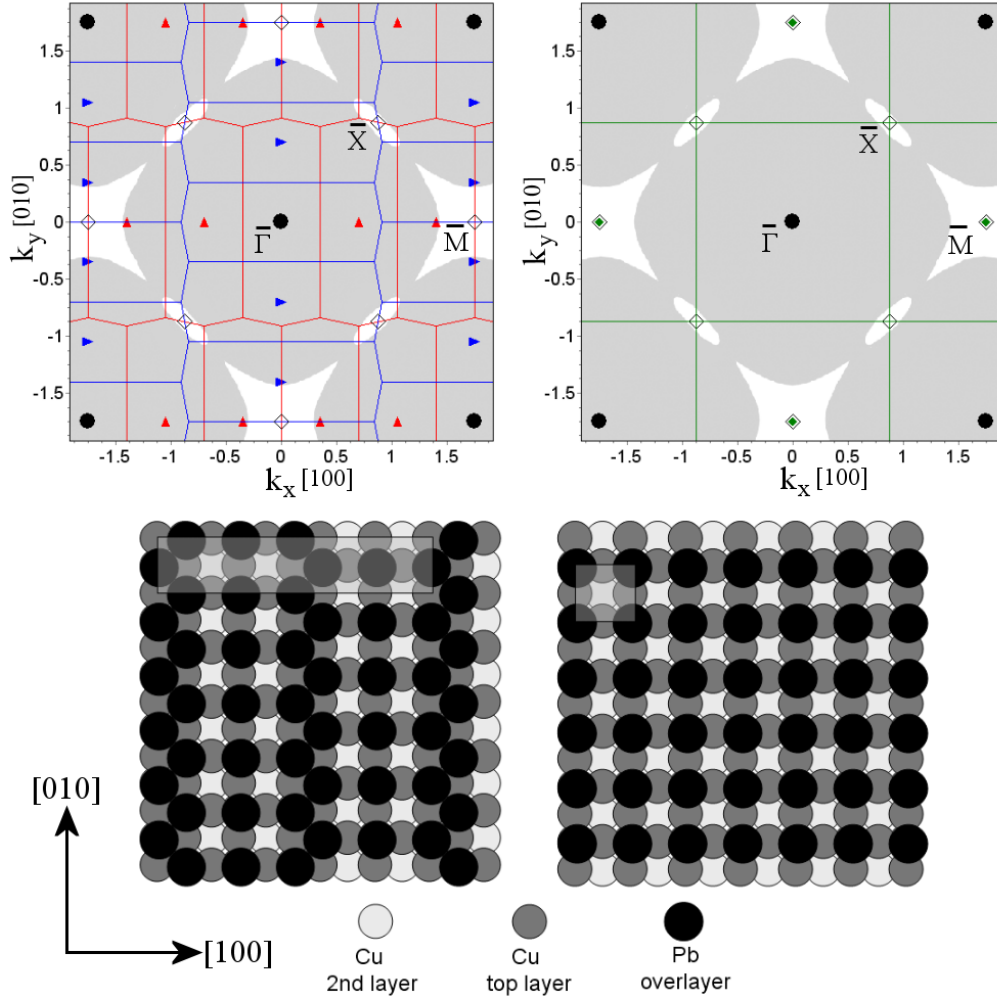


Figure 4.16 Top: Reciprocal space illustration of the Brillouin zones of the $c(5\sqrt{2}\times\sqrt{2})R45^\circ$ and $c(2\times 2)$ phases. Right panel shows the $c(2\times 2)$ Brillouin zone, and left panel the two domains of the $c(5\sqrt{2}\times\sqrt{2})R45^\circ$ phase. The unshaded areas denote the bulk Cu band gaps of the (001) surface. Bottom: literature atomic models for the $c(2\times 2)$ phase (right) and the $c(5\sqrt{2}\times\sqrt{2})R45^\circ$ phase (left).

As known already from the discussion about the $c(4\times 4)$ phase and shown in the top side of Figure 4.16, the projection of the Cu electronic bulk bands along the (001) direction leaves absolute band gaps around \bar{M} points. Fig. 4.16 shows ARPES spectra of both the room temperature $c(5\sqrt{2}\times\sqrt{2})R45^\circ$ and the high temperature split $c(2\times 2)$ phases, measured along $\bar{\Gamma}\bar{M}$ in the band-gap region. A prominent surface state band is observed in the split $c(2\times 2)$ phase. Taking into account the similarity of this surface state band with previous observations for In/Cu(100) (51) (52) and Sn/Cu(100) (54), its orbital origin is ascribed to a Pb 5sp-Cu 4sp band. It exhibits a parabolic dispersion towards the Fermi energy (E_F) with a nearly free-electron behaviour. It crosses E_F at 1.43 \AA^{-1} . The surface band dispersion can be fitted using a parabola of the form

$E=E_0+\hbar^2k^2/2m^*$, with values of $E_0=-6.06$ eV (bottom of the band) and $m^*=1.291 m_e$ (m_e , electron mass). Upon lowering the temperature and crossing the phase transition, the $c(5\sqrt{2}\times\sqrt{2})R45^\circ$ phase is formed.

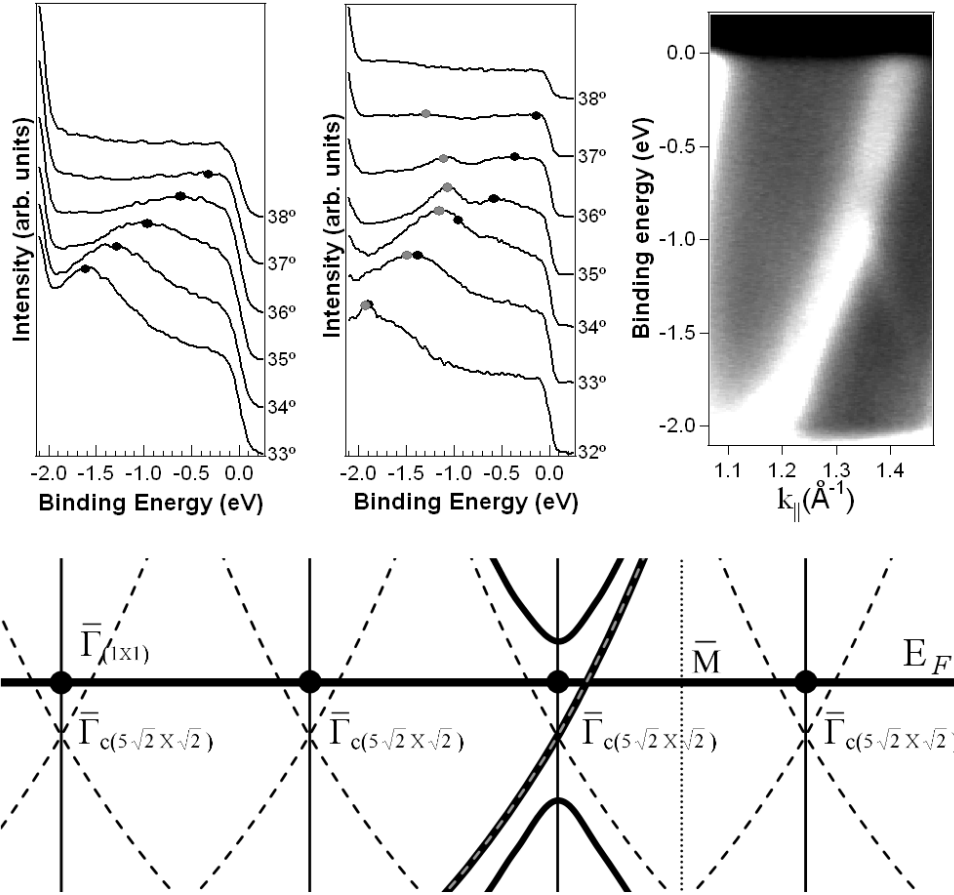


Figure 4.17 Top: valence-band spectra with $h\nu=27$ eV at 450 K (split $c(2\times 2)$ phase) and at 300 K ($c(5\sqrt{2}\times\sqrt{2})R45^\circ$ phase) together with the grayscale, respectively. Bottom: schematic diagram showing the proposed band backfolding in the $c(5\sqrt{2}\times\sqrt{2})R45^\circ$ phase is shown.

The appearance of the new phase gives rise to significant modifications in the surface electronic structure (Fig. 16). In the energy range below ~ 0.9 eV from E_F , the surface band is split in two different bands. One of them shows the same dispersion as in the $c(2\times 2)$ phase, while the second one is backfolded at 1.31 \AA^{-1} , opening a surface band gap. The origin of the two bands is understood recalling the existence of two orientational domains in the $c(5\sqrt{2}\times\sqrt{2})R45^\circ$ reconstruction. For one of the domains (see Fig. 15), the $\bar{\Gamma}\bar{M}$ direction probed runs parallel to the linear antiphase domain boundaries. In this case, we expect to observe a behaviour quite similar to the high-temperature split $c(2\times 2)$ phase, since each of the Pb stripes has the same $c(2\times 2)$

structure, and there is no extra periodicity along this direction. On the contrary, $\bar{\Gamma}\bar{M}$ is perpendicular to the linear antiphase domain boundaries for the other orientational domain, and we expect to be sensitive to the $c(5\sqrt{2}\times\sqrt{2})R45^\circ$ superstructure periodicity. Indeed, the observed backfolding is rationalized from the scheme shown in Fig. 17. The reciprocal space area probed is quite different for each of the domains. For one of them, we are around the $\bar{\Gamma}_{5\sqrt{2}}$ area, while for the other domain the area probed is of no special significance. Taking into account that the high-temperature split $c(2\times 2)$ phase exhibits a nearly-free electron surface band, we have folded this band with $c(5\sqrt{2}\times\sqrt{2})R45^\circ$ symmetry in Fig. 15. It is easy to see that we expect an avoided-crossing band gap at $\bar{\Gamma}_{5\sqrt{2}}$. Thus, we detect at the same time a band backfolding (with the opening of a surface band gap) for one of the domains, and for the other domain, a band which behaves as in the split $c(2\times 2)$ phase. The first band crosses the Fermi energy at 1.43 \AA^{-1} , a value close to the crossing point of the split $c(2\times 2)$ phase. The second band folds back at 1.38 \AA^{-1} , with a minimum binding energy of 0.9 eV (at 300 K). The folding point coincides very precisely with $\bar{\Gamma}_{5\sqrt{2}}$ (at 1.38 \AA^{-1}). The opening of an avoided-crossing band gap involves no significant energy gain, unless the gap coincides with the Fermi energy. Thus, an important point is to determine whether the upper band of the observed surface band gap is below or above the Fermi energy.

From a detailed analysis of the data shown in Fig. 4.16, it has been concluded (57) that there is no indication of backfolding for binding energies below 0.8 eV, where a single band is observed. Such an interpretation gives a major role to the electronic structure as the trigger of the phase transition. Higher angular resolution and higher cross section of the $c(5\sqrt{2}\times\sqrt{2})R45^\circ$ phase surface state can be achieved if the photon energy value is 25 eV instead of 27 eV. Moreover, subsequent azimuthal k_{\parallel} directions other than $\bar{\Gamma}\bar{M}$ have been measured in order to check the role of the electronic structure in the observed phase transition. Figure 4.18 (a) shows the band dispersion along the $\bar{\Gamma}\bar{M}$ direction measured with 25 eV photon energy. Parts (b) and (c) of Figure 4.18 are corresponding to k_{\parallel} direction 3° and 6° off $\bar{\Gamma}\bar{M}$ direction. As it can be observed, in top of the folded state there is another folded band close to the Fermi level. Exactly for the $\bar{\Gamma}\bar{M}$ direction, the intensity of this band is rather weak and it can be confused with the background. When increasing the azimuthal angle, the intensity of the folded band close to the Fermi level is also increasing. The position of the two observed folded bands

resembles to a sand clock. Such a situation places the gap position inside of the occupied states.

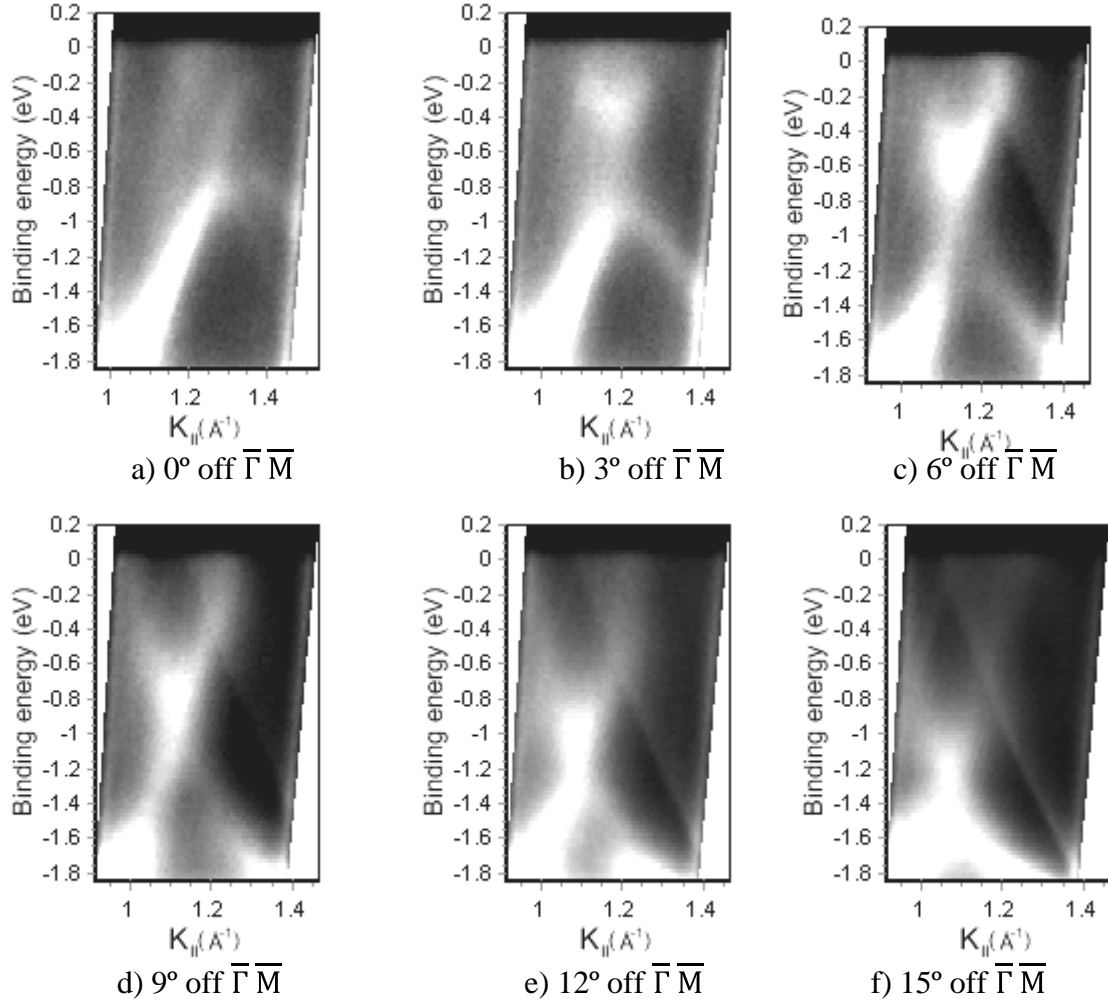


Figure 4.18 Band dispersion at 25 eV photon energy for the $c(5\sqrt{2}\times\sqrt{2})R45^\circ$ along $\bar{\Gamma}-\bar{M}$ direction (a). Several $k_{||}$ directions off $\bar{\Gamma}-\bar{M}$ are shown in the panels from (b) to (f).

The $c(2\times 2)$ and the split $c(2\times 2)$ at room temperatures present a very similar dispersion along the $\bar{\Gamma}-\bar{M}$ direction, as it can be seen in Figure 4.19.

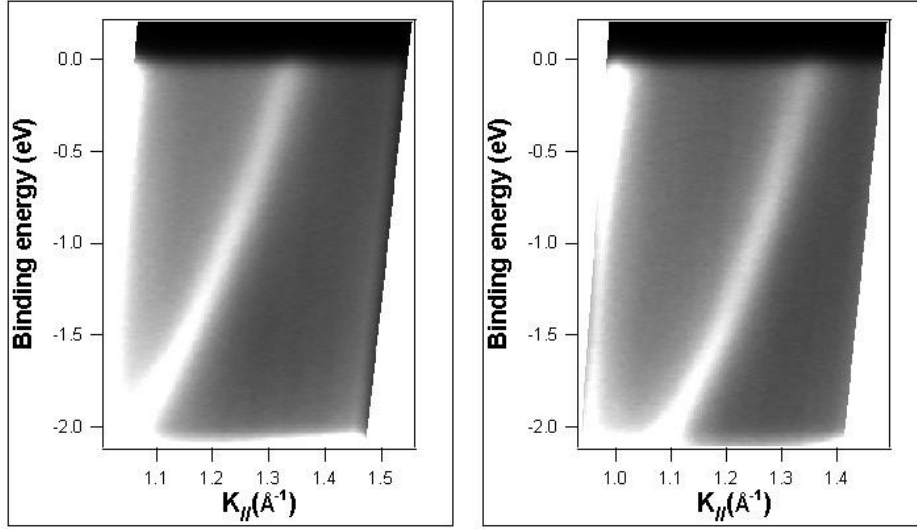


Figure 4.19 Band dispersion along the $\bar{\Gamma}\bar{M}$ direction measured with 27 eV for the $c(2\times 2)$ phase (left) and the split $c(2\times 2)$ right.

As it can be observed from the Figure 4.19, a single surface state crossing the Fermi level can be observed on the low $k_{||}$ values of the \bar{M} gap. The difference resides to the small $k_{||}$ value where the band is crossing the Fermi level, 1.36 \AA^{-1} for the $c(2\times 2)$ and 1.37 \AA^{-1} for the split $c(2\times 2)$.

4.6. Conclusions

The electronic structure of the Pb/Cu(001) system is showing a rich variety of phenomena. A novel gradual filling of an electronic surface state with an increasing Pb coverage for the submonolayer regime is observed with clarity along $\bar{\Gamma}\bar{M}$ direction. Folding of this state is observed in the occupied states for the $c(4\times 4)$ and $c(5\sqrt{2}\times\sqrt{2})R45^\circ$ phases at their corresponding symmetry points. The $c(4\times 4)$ structure shows a rich variety of states in the substrate band gap that can be theoretically understood by a nearly free electron like character of the surface state. The electronic structure contribution to the stability of the phases has been analyzed. A gap at the Fermi level for the observed surface state have been noted for the $c(4\times 4)$ structure for a portion of the reciprocal space, suggesting the contribution of the electronic structure in the $c(4\times 4)$ phase stability. From the ARUPS data, it can be drawn that the electronic structure plays a major role to the $c(5\sqrt{2}\times\sqrt{2})R45^\circ$ to split $c(2\times 2)$ phase transition.

**CHAPTER
FIVE**

5. Electronic structure of clean and halogenated Pt(110) surface

One of the most interesting features of surface science is that experimental and theoretical studies of well-characterized single-crystal surfaces may significantly advance the basic understanding of complex processes that take place at the solid surfaces. Platinum is of special interest due to its applications in heterogeneous catalysis. This chapter deals with the electronic structure of the Pt(110) surface and Pt(110) halogenated surface. The stable structure of the Pt(110) is the well-known (1×2) missing row reconstruction. A feature of this surface is the large stress anisotropy along the two high symmetry crystallographic directions. This property makes the Pt(110) surface a good model system to investigate and understand electronic effects related to a structural anisotropy. This surface is also a good model system for obtaining low dimensional surface structures by depositing an adsorbate. The adsorption of halogens is known to effectively inhibit several catalytic processes and to promote others (58). The catalytic properties of a surface are strongly affected by the surface electronic structure, and the poisoning mechanism of halogens may be explained by the modification of the surface electronic structure induced by the halogen adsorption. Beside the catalytic interest, halogens adsorbed on Pt(110) exhibit a rich behavior, with several surface reconstructions, depending on coverage and temperature (59). The main phases observed when depositing Br are a $c(2\times 2)$ and a (3×1) structure for Br coverages of 0.5 and 0.66 ML respectively. The distance between Pt atoms in the (3×1) phase of Br/Pt(110) is almost the same as in the $\text{K}_2\text{Pt}(\text{CN})_4\text{Br}_{0.30}\cdot 3\text{H}_2\text{O}$ (KCP) compound, which was the first material discovered showing a Charge Density Wave (CDW) instability (60). It has been proposed that the quasi-1D character of the Br/Pt(110)- (3×1) surface gives rise to the stabilization of a Surface Charge Density Wave (SCDW) from the Br/Pt(110)- $c(2\times 2)$ phase (61) (62) (63). The goal of this part of the thesis was to

comprehensively investigate the electronic structure of the clean Pt(110) surface and the Br halogenated surface at energies close to the Fermi level.

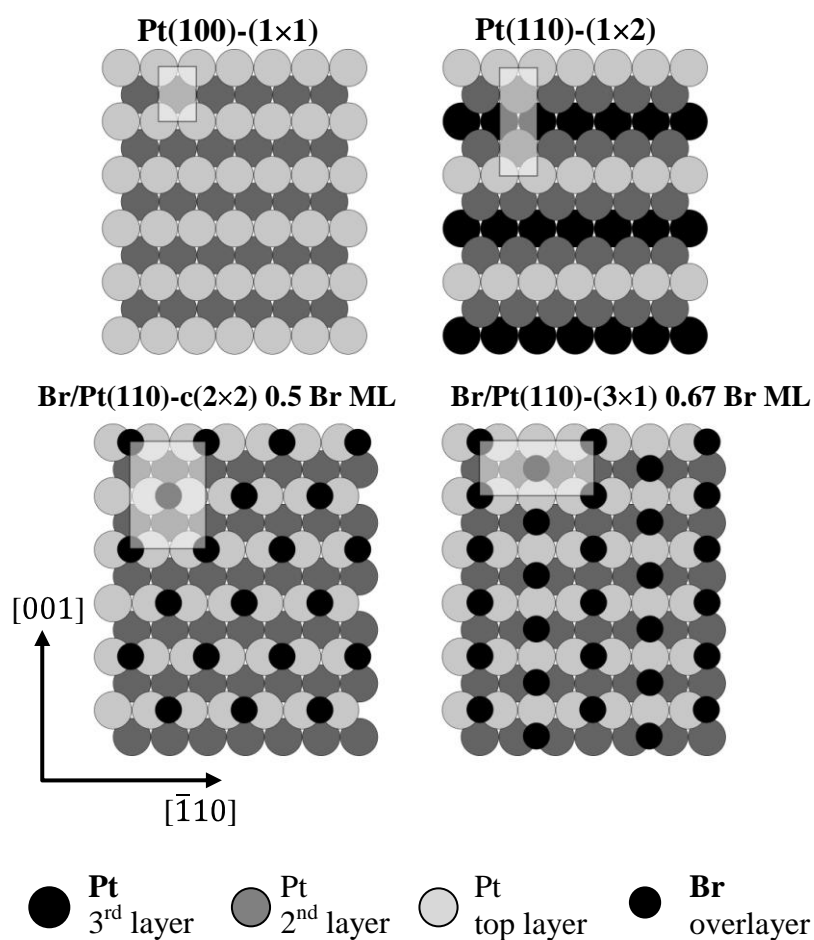


Figure 5.1 Literature atomic models of unreconstructed Pt(110) surface (a) and room temperature reconstruction (b) and main phases of Br/Pt(110) system (c and d). Structure and coverage are shown on top of the model. The unit cell of each structure is drawn as a gray rectangle.

5.1. Electronic structure of the clean Pt(110) surface

A proper preparation of the clean Pt(110) surface is leading to a (1×2) phase at room temperature (64). The (1×2) structure is also called “missing row” because on the surface every second $[\bar{1}10]$ surface chain is missing. The (1×2) phase presents a remarkable stability and temperatures higher than 960 K are required to trigger an Ising type order disorder phase transition to a (1×1) phase (64).

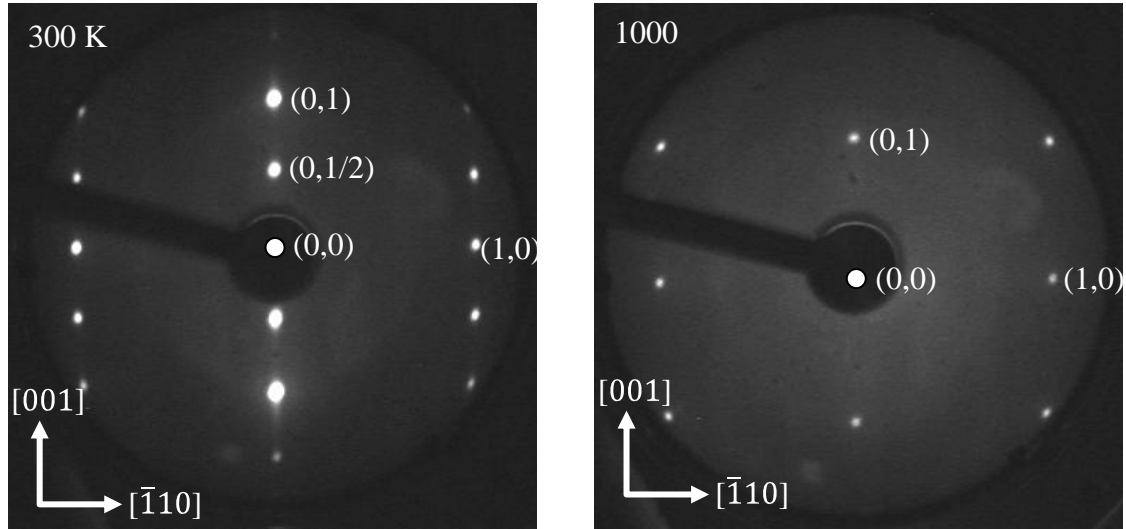


Figure 5.2 LEED patterns at 80 eV primary energy of Pt(110)- (1×2) phase at room temperature (left) and Pt(110)- (1×1) at around 1000 K (right).

Before performing any ARUPS measurements, the LEED pattern was checked in order to verify the reconstruction quality. Figure 5.2 shows the LEED patterns of the (1×2) phase (left), and the high temperature (1×1) phase.

The first step to understand the surface electronic structure of Pt(110) is understanding the bulk electronic structure. In the following, a brief description of the theoretical electronic structure of Pt is going to be presented. After that, novel results of the fingerprints of the bulk crystal electronic band structure will be shown, as obtained from photoemission experiments on Pt(110). The experimental surface states of the Pt(110) surface will be described and characterized in a subsequent subchapter.

5.2. The electronic structure of platinum. Calculated electronic structure.

For a clear understanding of the results presented here, the Brillouin zone of the face-centered cubic lattice with the naming convention of the high symmetry points is illustrated in the left side of Figure 5.3. The Brillouin zone of the (110) surface is shown in the right side of Figure 5.3. The surface \bar{X} symmetry point is the projection of the bulk X symmetry point while the bulk L point is projected onto the surface \bar{Y} symmetry point. The surface \bar{S} point is situated on top of the bulk W point. The surface $\bar{\Gamma}$ point is the projection of the bulk Γ point along $\Gamma\Sigma K$ direction of the bulk Brillouin zone.

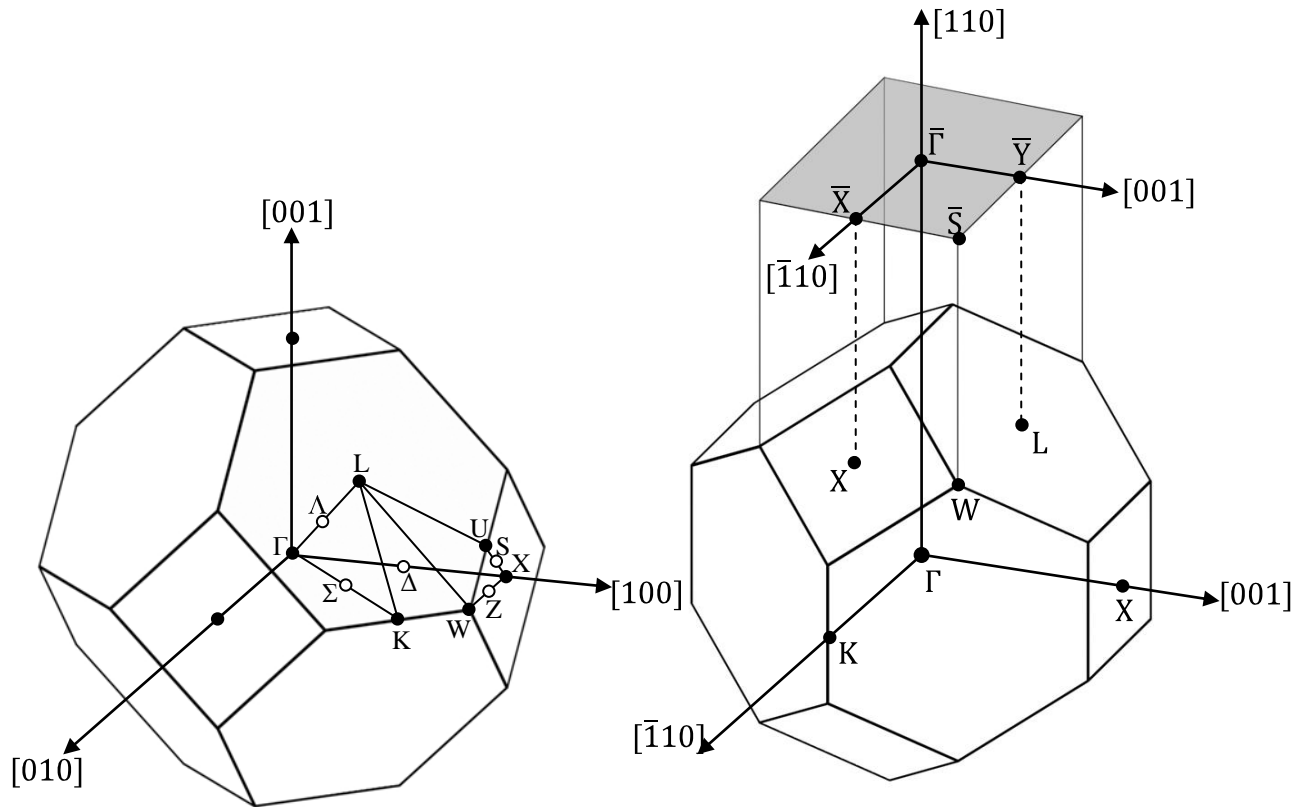


Figure 5.3 Left: Illustration of the first Brillouin zone of a face-centered cubic lattice including high symmetry k points marked with black filled dots. Right: Surface Brillouin zone of the (110) face with the corresponding symmetry and their relationship with the projection of bulk points. Note that the Brillouin zone from the right side is rotated 45° around $[010]$ axis compared with the one from the left side, in order to have the (110) surface horizontally aligned.

The electronic structure of Pt close to the Fermi level presents a complex configuration of the electronic bands (65). A main difference compared with noble metals (Cu, Ag, Au) is that Pt has an incomplete filling of the d-orbitals, some of Pt d-bands are therefore crossing the Fermi level. Figure 5.3 is illustrating the band structure of Pt along high symmetry directions. The numbering of the bands is consistent with a tight binding model using a *spd* orbital basis. Lines are showing the result of the band structure calculation from reference [papa]. The dotted lines are the result of the tight binding calculation using the code presented in the third chapter of this thesis. Based on these calculations, one finds three bands at the Fermi level. Band number 6 has an sp character, while bands 3, 4 and 5 have d character. Photoemission and Haas van Alphen measurements of Pt (65) indicate that the electronic structure calculations should take in account a relativistic description of the band structure. The effect of a relativistic calculation is mainly affecting the d bands. In Figure 5.4, the position of the bands number 3, 4 and 5 as a result of relativistic effects calculation is represented with dashed lines.

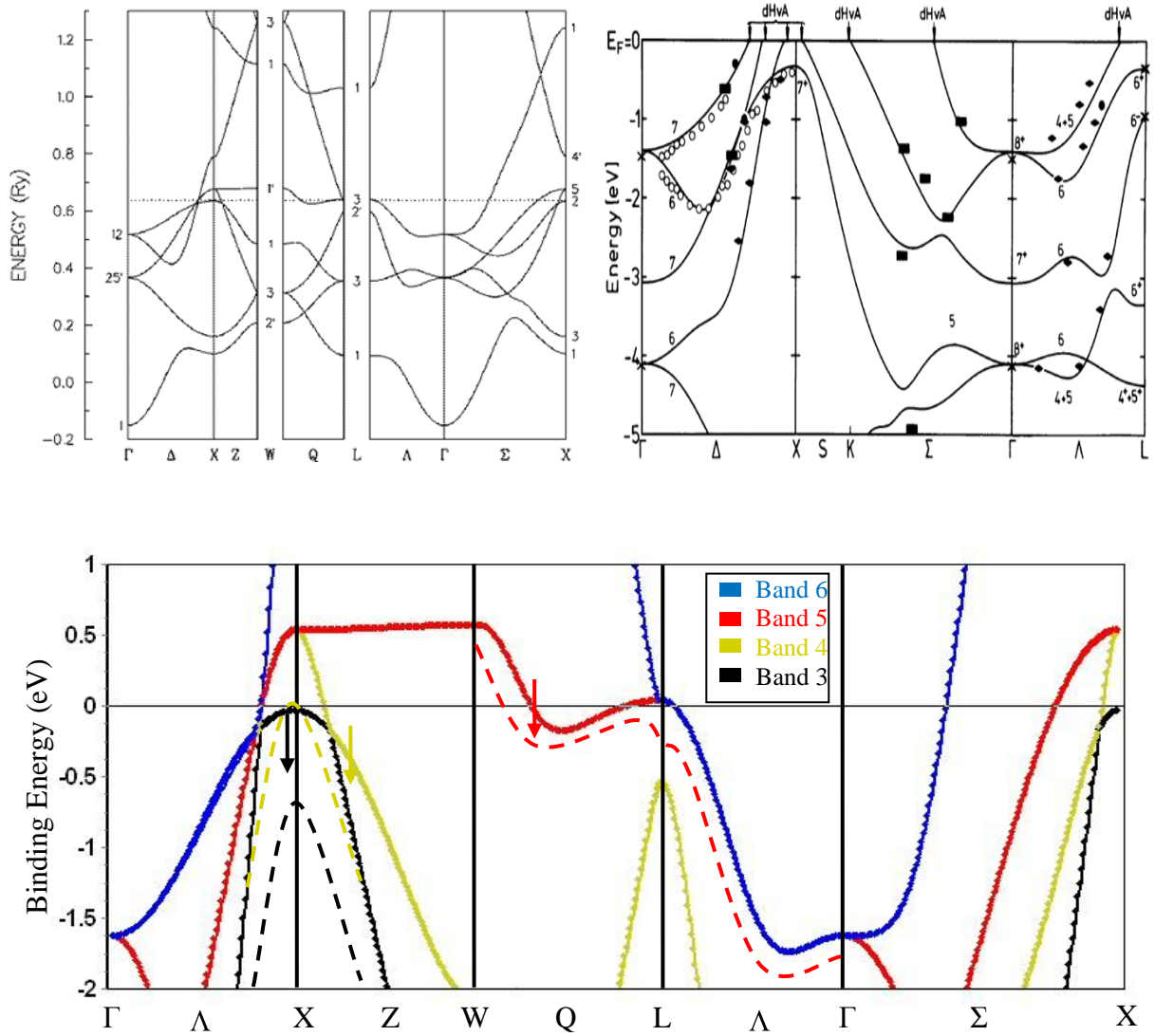


Figure 5.4 Band structure of Pt close to the Fermi level along high symmetry directions. Bottom: Lines denote the bands position from reference [papa], dotted lines correspond to our tight binding calculation. Dashed lines are indicating the position of the bands when calculating the band structure taking in account relativistic effects. The band number from the legend panel correspond with the number of the band in the tight binding model. Top left: Tight binding electronic structure calculation of Pt with a larger energy scale from reference Papa. Top right: Electronic structure calculations of Pt including relativistic effects and experimental photoemission (dots) and Haas-van Alphen (Fermi level) data (from reference (65)).

The main effect of including relativistic effects in the calculation of the electronic structure of Pt is a lowering in binding energy of the position of the d-bands. Band number 5, represented in red in Figure 5.4, is no longer crossing the Fermi level along ΓL direction. Regarding the LW direction, for the relativistic calculation, band number 5 crosses the Fermi level in only one point instead of two. The same band number 5 is

also well separated from band number 6 (the sp band) when dispersing along Γ L direction. The most dramatic change produced by the relativistic effects is found around the X point. Band number 4, represented in yellow in Figure 5.3, is found almost entirely in the occupied states, and band number 3, colored in black, is lowered by around 1 eV in energy.

The Fermi surface of Pt from tight binding calculations is shown in Figure 5.4. The Fermi surface from the left side of Figure 5.5 has been calculated using the ELAN code described in the third chapter of this thesis, using the parameters from reference [papa]. On the right side of Fig 5.4 the Fermi surface from reference [Florida] is shown. As it can be remarked, there is a difference for band number 5 (drawn in red) near to the L point. Both Fermi surfaces displayed in Figure 5.5 should be similar, because they are using the same set of tight binding parameters, but it seems that the authors from reference Florida were using a higher value for the Fermi level.

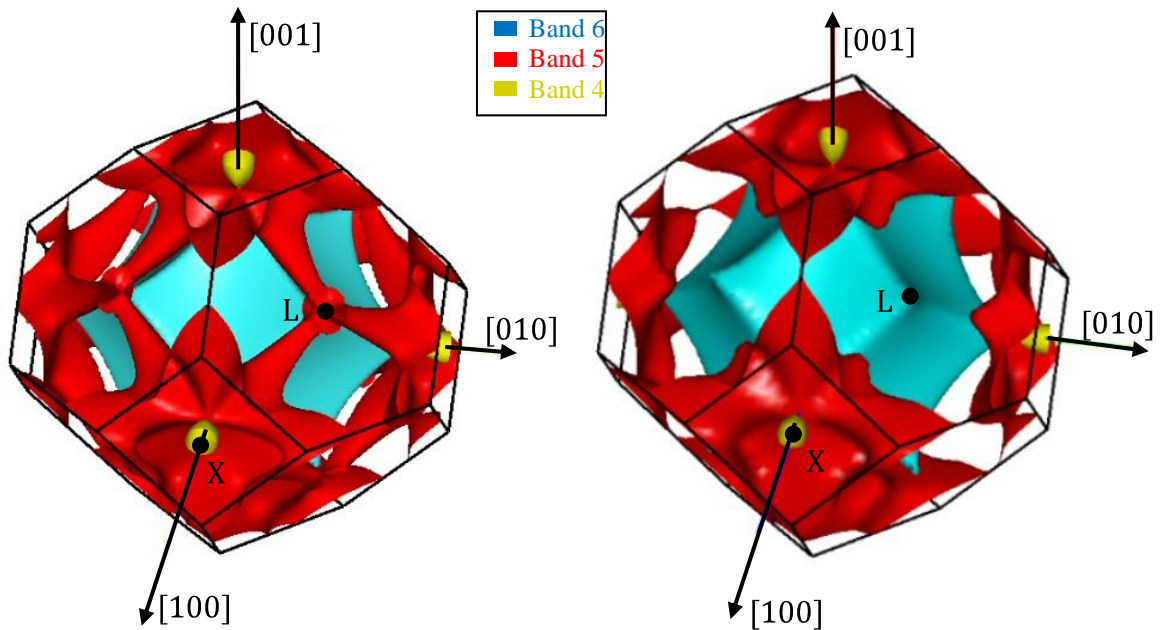


Figure 5.5 Left: Fermi surface of Pt calculated using a tight binding model calculated with ELAN code. Right: Fermi surface of Pt from reference [Florida]. A difference between the two surfaces can be noted for the band 5 (drawn in red) around the L point.

A reason why the Fermi surface from reference Florida has been included in Figure 5.5 is because it is closer to a possible Fermi surface calculation taking in account relativistic effects. Using a higher value for the Fermi level lowers the binding energy of the bands for the Fermi surface, in a similar way as the relativistic effects do.

5.2.1. Fermi surfaces and band dispersion of Pt(110)

The characteristic behaviour of the Pt bands at the Fermi level gives rise to a complex Fermi surface cut for the (110) surface. A recall to the effects of the initial and final states width in the photoemission process is necessary to understand the experimental Fermi surfaces. Left and middle column in **Figure 5.6** show the theoretical Fermi surface maps for three photon energies (45, 24 and 20 eV). These photon energies correspond to three measured Fermi surface maps shown on the right column in **Figure 5.6**. The theoretical calculations were performed for an unreconstructed (1×1) surface (left column) and a (1×2) surface (middle column) using 0.1 eV width of the initial state and 2 eV width of the final state when calculating the intensity map[Lindros]. A 5% of partial density of states contribution has been also included to reproduce features observed in the experimental maps. Other photoemission matrix elements different from the initial and final state width effects have not been included in the calculation.

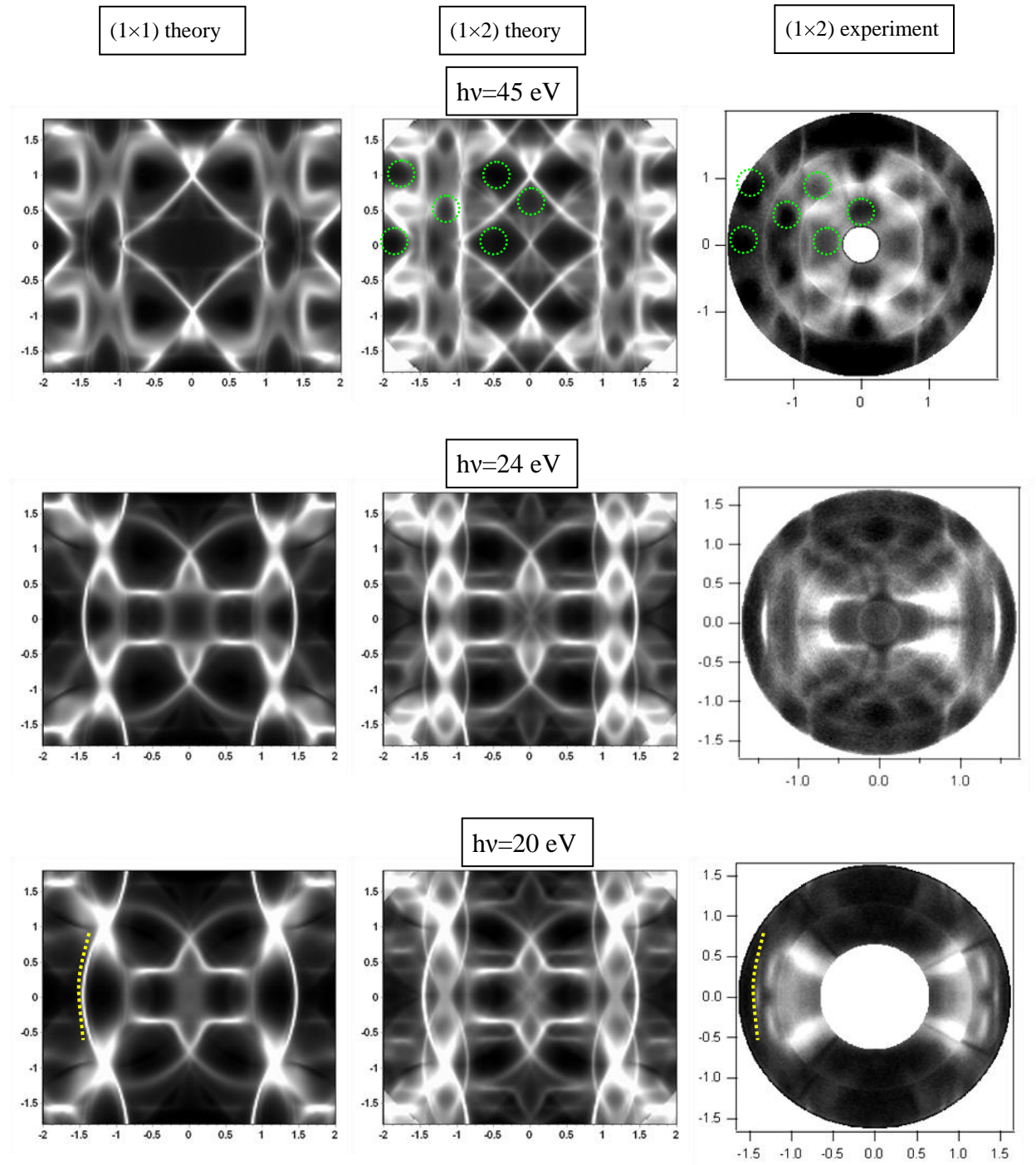


Figure 5.6 Theoretical (left and middle column) and experimental (right column) Fermi surfaces of Pt(110) for different photon energies (45 eV top row, 24 eV middle row and 20 eV bottom row). Left column corresponds to a calculation of an unreconstructed (1×1) surface while middle column to a (1×2) surface.

A qualitative agreement between the theoretical and experimental Fermi surfaces from Figure 5.6 can be observed. An analysis of the electronic structure based on this agreement is presented here. This analysis is of great help in understanding later the band dispersion along the high k_{\parallel} symmetry direction of the Pt(110) surface.

The first important analogy between the theoretical and experimental Fermi surfaces for a photon energy of 45 eV (Figure 5.6 top) and 24 eV (Figure 5.6 middle) is the existence of well defined low intensity “holes” in the photoemission map. The holes that are analog both in the experimental and theoretical plots have been emphasized with a green dashed contour in Figure 5.6. These holes are defined by borders that are originating even from the cuts given by the final state or by the band edges coming from the non conservative transitions. For photon energy values of 45 eV and 24 eV, a good contrasted edge defined by the band number 6 (the sp band) is emphasized with a yellow dashed line. For a photon energy of 20 eV, the final state position of the sp band in the k space generates a well defined contour (marked also with a yellow dashed line) parallel with the $\bar{X}\bar{S}$ direction. The good theory-experiment agreement of the k_{\parallel} position of this edge indicates that the sp band is well reproduced by the theoretical model. Regarding a d band present at the Fermi level (number 5), it is properly seen in the photoemission experiments for a photon energy of 24 and 20 eV. It is underlined with a blue dashed line both in the experimental and theoretical plots (Figure 5.6 middle and bottom). The theory experiment agreement for the d band (number 5) is not as good as it is for the sp band but qualitatively the theoretical model is reproducing the experiment.

The information given by the Fermi surfaces presented before makes it possible to understand features of the band dispersion along high symmetry direction of the Pt(110) surface. The band dispersion obtained by using HeI α radiation (21.23 eV) along $\bar{\Gamma}\bar{X}$ and $\bar{\Gamma}\bar{Y}$ directions is shown in Figure 5.7.

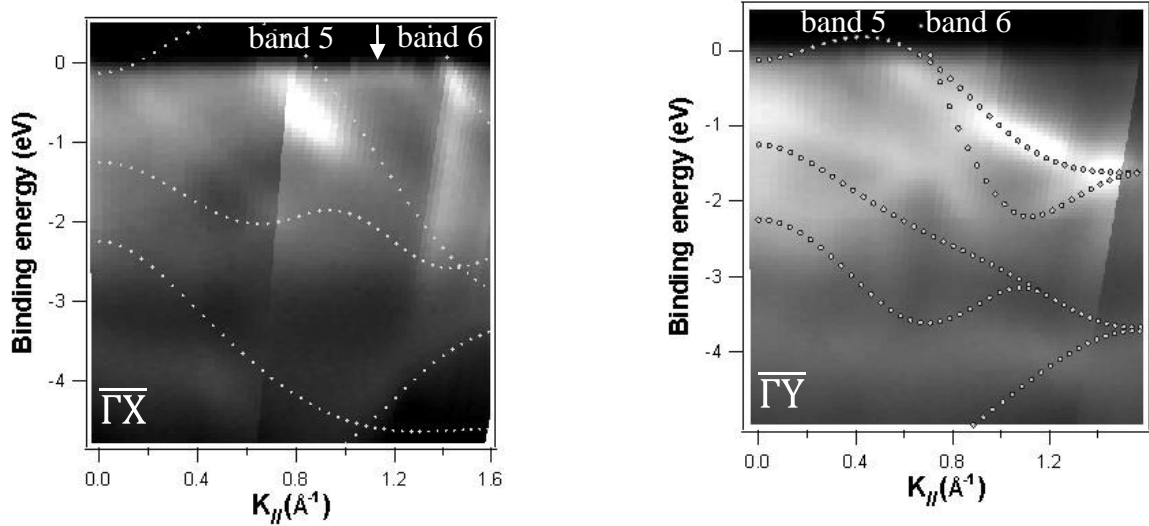


Figure 5.7 Band dispersion of the Pt(110)-(1×2) surface along $\bar{\Gamma}\bar{X}$ (left) and $\bar{\Gamma}\bar{Y}$ (right) directions using HeI α radiation (21.23 eV). A remarkable agreement between the theoretical model (plotted with dotted line) and the experiment is observed along $\bar{\Gamma}\bar{X}$ for the band number 6 (sp band). The experimental d-band (number 5) stays at lower binding energies than the calculation.

The band crossing the Fermi level at a $k_{||}$ value of 1.5 \AA^{-1} along $\bar{\Gamma}\bar{X}$ direction (Figure 5.7 left) can be identified without any doubt as being the sp band (band number 6 of the tight binding model). The other intense band along $\bar{\Gamma}\bar{X}$ that crosses the Fermi level at a $k_{||}$ value of 0.8 \AA^{-1} is a d band (band number 5 of the tight binding model). As the relativistic calculations (65) indicate, the theoretical band from the simple tight binding model is appears at a higher binding energy. Nevertheless, the band crossing the Fermi level at a $k_{||}$ value of 0.8 \AA^{-1} along $\bar{\Gamma}\bar{X}$ direction is a d band. Between the d-band and the sp-band along $\bar{\Gamma}\bar{X}$ direction at the Fermi level, one observes a weak band marked with a white arrow. Along the $\bar{\Gamma}\bar{Y}$ direction, a good agreement is found both for the sp band and the d band number 5. The other observed bands except band 5 and band 6 show a rather poor experiment-theory agreement. A tight binding parameterization of the relativistic calculations would probably increase the agreement between the experiment and the tight binding model.

5.2.2. Surface states of Pt(110)-(1×2) surface

The hints given by the information from the Fermi surfaces and the band dispersion indicates the presence of an extra band around the \bar{X} point of the Pt(110)-(1×2) surface. As it will be shown, this band can be attributed to a surface state. The same band dispersion measurements as in the lab has been performed at the synchrotron using horizontally polarized 21.2 eV radiation. The grayscale map of the dispersion along $\bar{\Gamma}\bar{X}$ and $\bar{\Gamma}\bar{Y}$ direction is shown in Figure 5.8.

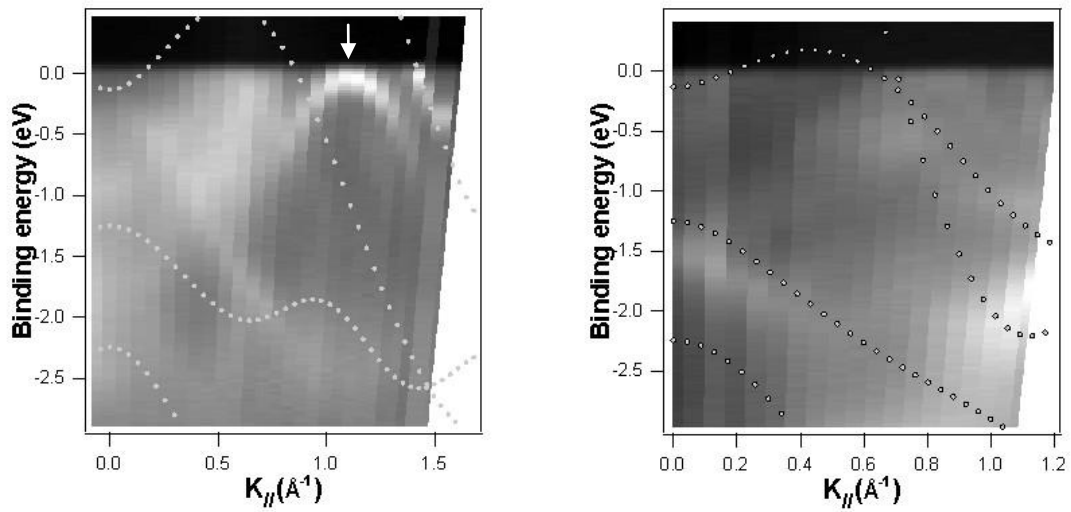


Figure 5.8 Band dispersion of the Pt(110)-(1×2) surface along $\bar{\Gamma}\bar{X}$ (left) and $\bar{\Gamma}\bar{Y}$ (right) directions using polarized radiation in the horizontal plane ($h\nu=21.2$ eV). Compared with HeI α radiation, the d-band number 5 is strongly attenuated both along $\bar{\Gamma}\bar{X}$ direction, but the most remarkable difference is the perfectly contoured state at the \bar{X} point.

A simple comparison between the dispersion using non polarized (HeI α , Figure 5.6) and polarized radiation of the same energy (Figure 5.8) shows a strong attenuation of the d band number 5 along $\bar{\Gamma}\bar{X}$ direction. The most dramatic effect observed when comparing the dispersion along $\bar{\Gamma}\bar{X}$ direction is a much higher contrast for the state from the \bar{X} point when seen with polarized radiation. The explanation of this change can be traced back to the orbital origin of the band. The d_{xy} symmetry of the band number 5 makes that the intensity along $\bar{\Gamma}\bar{X}$ direction of the (110) surface is going theoretically to 0. The non-conservative transitions that are generating the photoemission background in the occupied states are also symmetry dependent, resulting in a background of lower intensity. In this way, the state from the \bar{X} point is much better contrasted.

The state from the \bar{X} point is best observed at a photon energy of 20 eV. Even if this value is close to 21.23 eV, the state is much better defined and it lies in a background lower than for 21.23 eV. Figure 5.9 shows the state dispersion along $\bar{\Gamma}\bar{X}$ direction for a photon energy of 20 eV. The width of this state is 50 meV and its binding energy at the \bar{X} point is -75 meV.

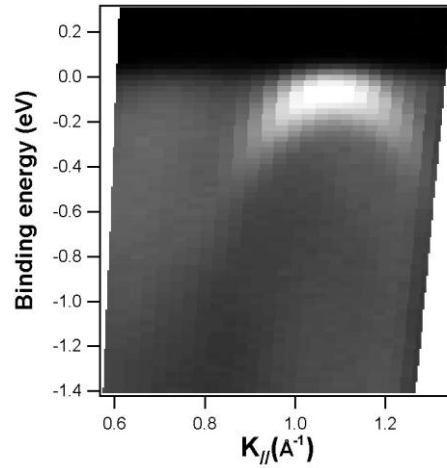


Figure 5.9 Dispersion along $\bar{\Gamma}\bar{X}$ of the state found around the \bar{X} point. The measurement has been performed with a photon energy of 20 eV, corresponding to the maximum cross section of this state.

In the following paragraphs we expose several arguments supporting that the state displayed in Figure 5.9 has a surface character. Contrary to the bulk states, a surface state is not dispersing with the photon energy, meaning that it is staying at the same binding energy independently of the photon energy value. Figure 5.10 shows photon energy EDCs acquired at the \bar{X} point. The black arrow is marking the position of the state from Figure 5.9. There is no observable dispersion, so the photon energy scans at the \bar{X} point bring a first evidence in favor that the state close to the Fermi level at the \bar{X} point is a surface state. Another comment can be made regarding the photon energy scans at the \bar{X} point of the Pt(110)-(1×2) surface. A second non dispersive band is observed at -0.4 eV at the \bar{X} point, marked with a grey arrow. At the time of the measurements, it was thought to be a bulk band, therefore no additional information was acquired to distinguish its origin. There are two dispersive bands in the photon energy scans from Figure 5.10, the d bands number 4 (the yellow dashed line) and number 3 (blue dashed line). From the tight binding model, these two bands should appear at a higher binding energy.

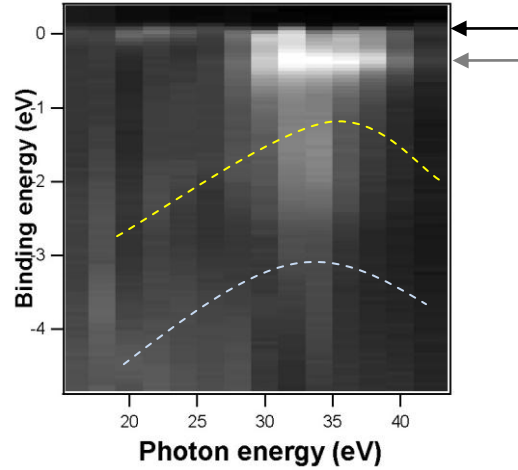


Figure 5.10 Photon energy scans at the \bar{X} point of Pt(110)-(1 \times 2) surface. The arrows are indicating the position of two non-dispersing states close to the Fermi level. Dashed lines correspond to the position of bulk bands.

Another strong argument supporting that the state observed near the Fermi level at the \bar{X} point has a surface character is its dispersion along other k_{\parallel} directions. By exhaustively mapping this state in reciprocal space, a comparison with the expected evolution of bulk Pt bands can be made and a bulk origin can be discarded. Furthermore, if the observed state has a surface character, it has to follow the surface periodicity, in this case a (1 \times 2) and not a (1 \times 1) symmetry. In order to check the above mentioned points, several k_{\parallel} cuts parallel with $\bar{\Gamma}\bar{X}$ have been scanned. From these scans, the Fermi contour has been rebuild. Also, the dispersion along $\bar{X}\bar{S}$ direction has been measured for a clearer description of the state observed at the \bar{X} point. A sketch showing which directions have been measured together with the (1 \times 1) and (1 \times 2) Brillouin zones is drawn in Figure 5.11. The constant k_{\parallel} cuts parallel with $\bar{\Gamma}\bar{X}$ are represented with green lines and the $\bar{X}\bar{S}$ direction with a blue line.

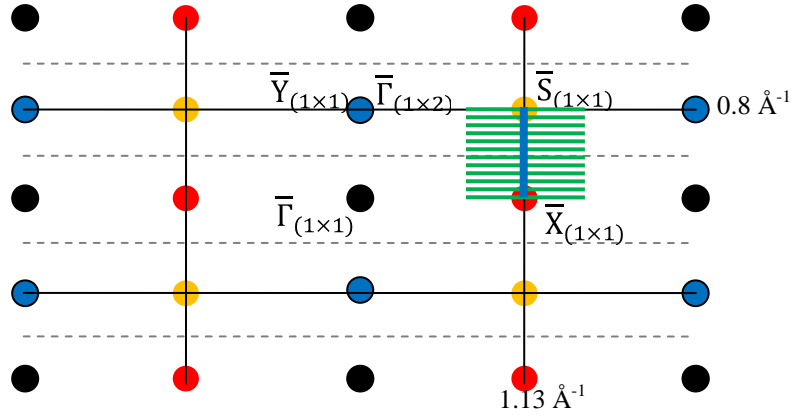


Figure 5.11 The Brillouin zone and symmetry points of Pt(110) (1 \times 1) and (1 \times 2) surfaces. The lines denote BZ boundaries (black for the (1 \times 1) structure and dashed grey for the (1 \times 2) structure). The green lines are lines of constant $k_{||}$ cuts parallel with $\bar{\Gamma}\bar{X}$ direction. The blue line indicates the $\bar{X}\bar{S}$ direction.

The results of the scans whose directions are parallel with the $\bar{\Gamma}\bar{X}$ direction are shown in Figure 5.12. The left scan in Figure 5.12 contains the \bar{X} point and the one in the right contains the \bar{S} point. Four scans of intermediate constant $k_{||y}$ with the value displayed on top of the scans are also plotted in Figure 5.12.

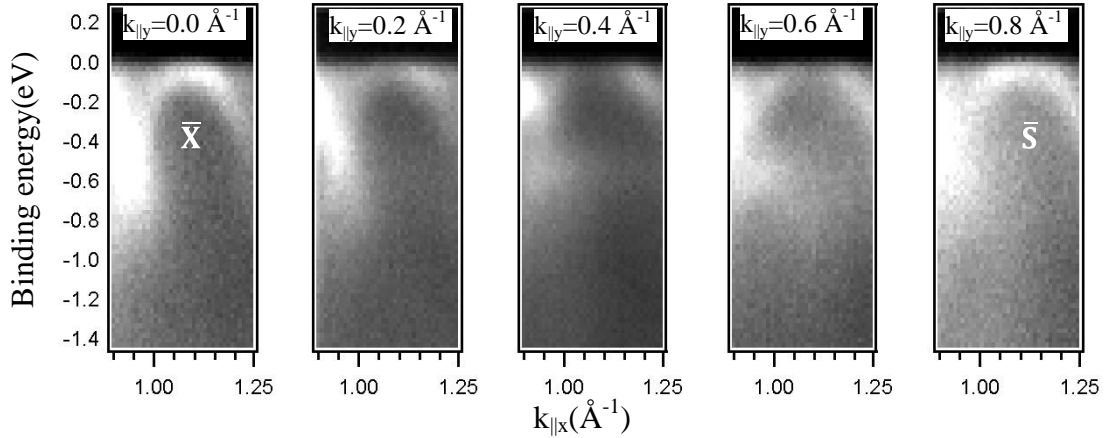


Figure 5.12 Dispersion along $k_{||}$ lines parallel with the $\bar{\Gamma}\bar{X}$ direction. The value of the constant $k_{||y}$ is specified on top of each scan

As shown in Figure 5.12, the \bar{X} point state keeps its reverse parabolic dispersion when scanning lines parallel with $\bar{\Gamma}\bar{X}$ direction of increasing $k_{||y}$ value. The position of the point of maximum binding energy of this parabola is changing with the $k_{||y}$ value and it follows the $\bar{X}\bar{S}$ direction. At the \bar{X} and \bar{S} points, the reverse parabola reaches the lowest binding energies, and at the mid point between \bar{X} and \bar{S} ($k_{||y}=0.4 \text{ \AA}^{-1}$) it reaches

the maximum binding energy. This behavior can be seen clearly in Figure 5.13, which shows the band dispersion along $\bar{X}\bar{S}$ direction. A small deviation from the $\bar{X}\bar{S}$ direction could not be avoided due to the experimental measurement geometry, making that the k_{\parallel} direction did not go exactly to the \bar{S} point. Nevertheless, a “positive” parabolic dispersion is observed at both \bar{X} and \bar{S} points.

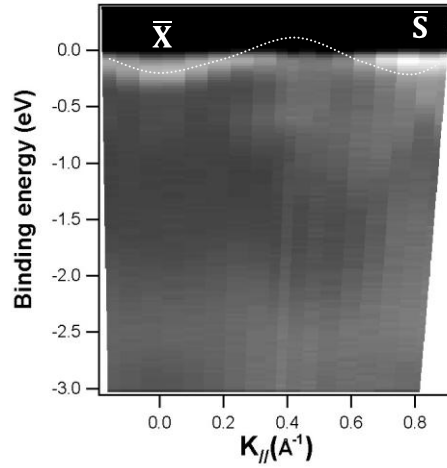


Figure 5.13 Band dispersion of Pt(110)-(1×2) surface along $\bar{X}\bar{S}$ direction using a photon energy of 21.2 eV.

A comprehensive description of Fermi level behaviour of the state observed at the \bar{X} point is given also by the Fermi surfaces shown in Figure 5.14, measured with a photon energy of 21.2 eV (right) and 60 eV (left).

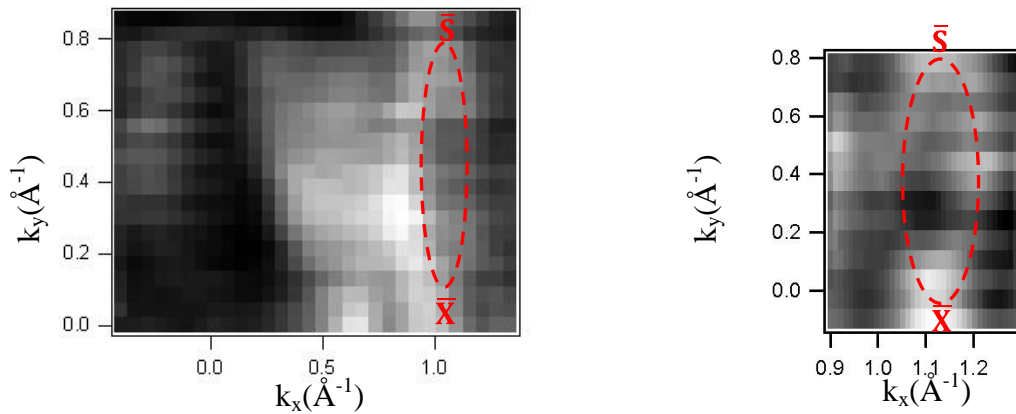


Figure 5.14 Fermi surfaces of the Pt(110)-(1×2) surface for a photon energy of 60 eV (left) and 21.2 eV (right).

All the experimental information gathered for the presumed surface state observed initially at the \bar{X} point is leading at this point to a clear description of this state. In a

$E(k_{||x}, k_{||y})$ description, as illustrated in Figure 5.15 and based on the experimental data shown before, the state is defining a continuous surface for which the \bar{X} and \bar{S} points are saddle points. The surface in the neighborhood of the \bar{X} and \bar{S} points is lying on different sides of the surface tangent. Along the $\bar{X}\bar{S}$ direction the surface is curved *up* while along the $\bar{\Gamma}\bar{X}$ direction the surface is curved *down*.

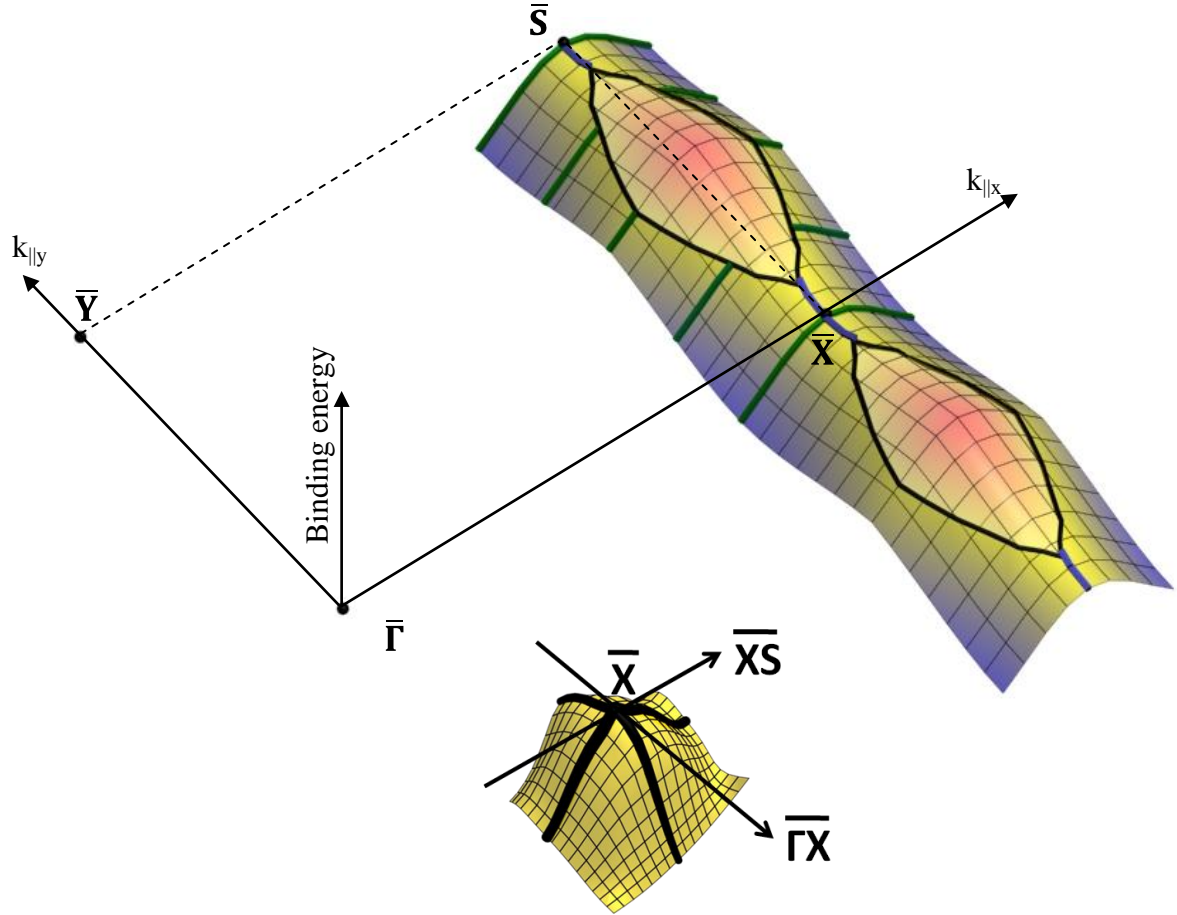


Figure 5.15 Top: $E(k_{||x}, k_{||y})$ description of the observed state. The green lines corresponds with the experimental data shown in Fig 5.11. The blue line corresponds to the $\bar{X}\bar{S}$ dispersion data shown in Figure 5.12. Bottom: Band dispersion at \bar{X} point of a d-bulk band.

The fact that at the \bar{X} point the state shows a saddle point behavior discards a d-like bulk origin. The projections or the cuts of the bulk d-bands on the (110) surface are creating pocket-like shaped surfaces, showing reversed parabolas at the \bar{X} point, both along $\bar{\Gamma}\bar{X}$ and $\bar{X}\bar{S}$ directions (ref th-exp) and not saddle surfaces. The fact that the observed state is symmetrical at the \bar{X} and \bar{S} points indicates that the state follows the (1×2) superstructure symmetry.

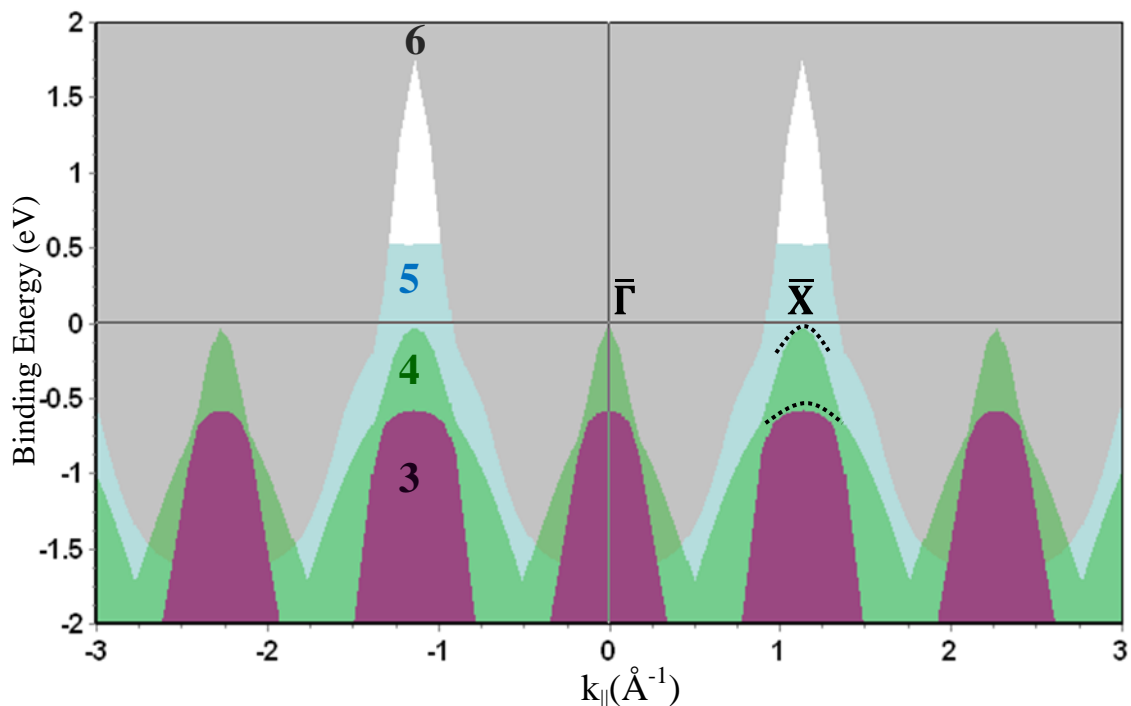


Figure 5.16 Pt(110) color specific band projection along $\bar{\Gamma}\bar{X}$ direction. Band number comes from a tight binding model based on an spd basis. The bands 3 and 4 are on purpose plotted 0.55 eV lower than the calculation of the tight binding model to reproduce relativistic calculations.

A great help in identifying the origin of the state observed at the \bar{X} point is given by the bulk band projection along $\bar{\Gamma}\bar{X}$ direction of Pt(110) surface (Figure 5.16). The bands 3 and 4 are on purpose plotted 0.55 eV lower than the calculation of the tight binding model to reproduce relativistic calculations. We assign the state observed at the \bar{X} point to a resonance that stays on top of band number 4. An extra state exists on top of band 3, detected in the experiment as the non dispersive band at -0.6 eV in Figure 5.10.

The last argument supporting that the state observed at the \bar{X} point near the Fermi level has a surface character is based on the surface sensitivity of a surface state. If the Pt(110) surface is not annealed after the sputtering, it shows a (1×1) LEED corresponding to a less well ordered structure. Since the surface quality after ion sputtering is by far not so good as after an annealing treatment, it is expected that the intensity of any surface state to be strongly reduced.

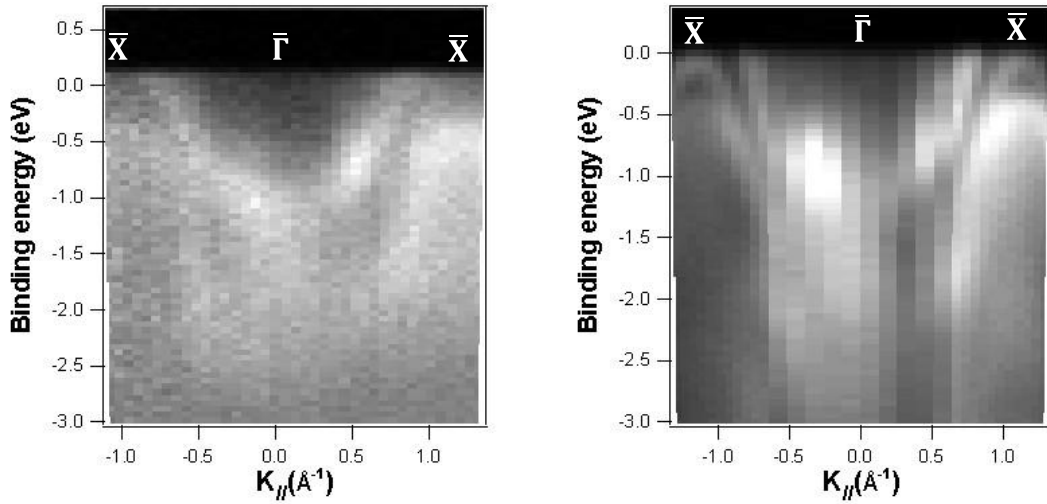


Figure 5.17 Left: Band dispersion of sputtered and not annealed Pt(110) surface along $\bar{\Gamma}\bar{X}$ direction measured at a photon energy of 60 eV. Right: Same type of scan but of the annealed surface.

Figure 5.17 shows at left the band dispersion of a sputtered and not annealed Pt(110) surface along $\bar{\Gamma}\bar{X}$ direction. One can observe that the state at the Fermi level that is visible at the \bar{X} point for the annealed surface (Figure 5.17 right) is no longer present for the disordered surface.

The arguments presented in this subchapter are leading to the conclusion that the reverse parabolic state observed initially at the \bar{X} point presents a surface character. The absence of an absolute gap in the k region where this state is dispersing indicates that this state is a surface resonance.

5.3. Electronic structure of Br/Pt(110) system

The major interest of studying the Br/Pt(110) system comes from the hypothesis formulated in reference (62) that the (3×1) phase of this system results from the stabilization of a CDW. It has been stated that an extremely small amount of Br (<0.005 ML) deposited at room temperature on the $c(2\times 2)$ phase causes a spectacular change in the STM images. A subsequent annealing results in a (3×1) phase visible in the LEED pattern. Rather than a classical Peierls CDW transition, the CDW transition is obtained by affecting the surface stability of the $c(2\times 2)$ phase after slightly modifying the adsorbate coverage (61). Angle resolved photoemission data have been used to confirm a Peierls nesting of the Fermi surface for the (3×1) phase. The goal of the ARUPS study of the (3×1) phase system was to extend the investigation of the electronic structure of this system. Recent data published during the time of writing of this thesis suggest the existence of two (3×1) phases (66). A “proper” (3×1) phase would be obtained at a Br coverage of 0.66 ML and a (3×1) phase that is a fluctuating (3×2) CDW phase is observed at 50 K for a coverage close to 0.5 ML. In this work, only the “proper” (3×1) phase has been investigated. The ARUPS results of the “proper” (3×1) phase have been employed in reference (61) to argue that the (3×1) structure is a CDW phase.

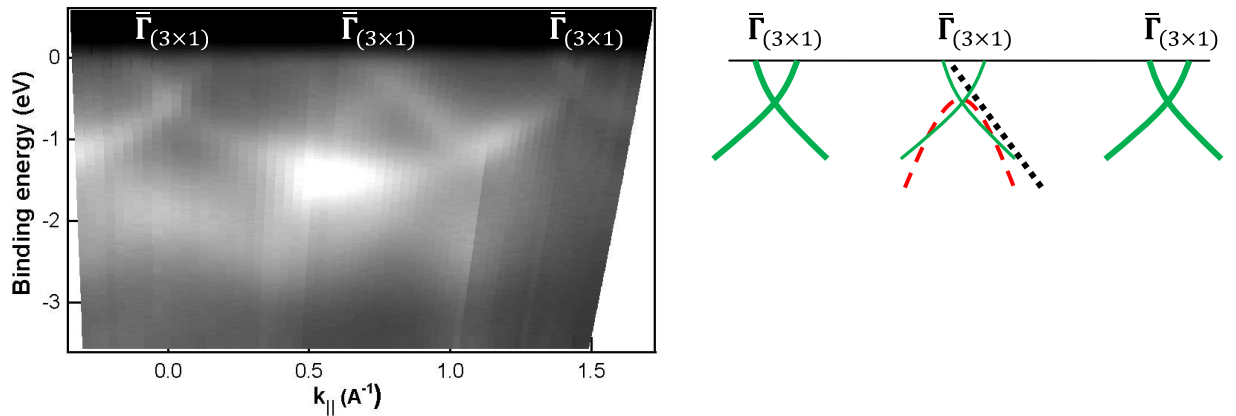


Figure 5.18 Left: experimental band dispersion along $\bar{\Gamma}\bar{X}$ direction of the (3×1) phase of Br/Pt(110) system for a photon energy of 21.2 eV. Right: Illustration of the bands observed in the left side. The color of the lines and their interpretation is explained in the text.

The band dispersion of Br/Pt(110)- (3×1) surface along $\bar{\Gamma}\bar{X}$ direction for a photon energy of 21.2 eV is presented in Figure 5.18. The experimental data agree well with the data published in ref. B. In the experimental grayscale data shown in the left side, three

$\bar{\Gamma}$ points of the (3×1) structure are covered by the scan. The features from the central $\bar{\Gamma}$ point at a k_{\parallel} value of 0.75 \AA^{-1} have been interpreted in ref (61) as a backfolded band exposing a gap at the Fermi level, as it is shown in the right side of the Figure 5.18 with a red dashed line. The origin of this band has been extrapolated from the experimental and theoretical $c(2 \times 2)$ electronic structure (36). The $c(2 \times 2)$ structure shows at a $k_{\parallel}=0.75 \text{ \AA}^{-1}$ along $\bar{\Gamma}\bar{X}$ direction a crossing band (marked with a black dashed line in the right side of Figure 5.18). The k_{\parallel} value of crossing coincides with the nesting vector needed to produce a CDW with three fold periodicity (59). The experimental gap opened by the proposed backfolded band was assumed to be opening at the Fermi level, resulting in a lowering of the electronic energy, which would be the driving force to stabilize the (3×1) structure. Exactly this interpretation of the bands shown in Figure 5.18 is going to be brought under debate in this subchapter of the thesis. Moreover, additional ARUPS data are going to be presented and analyzed.

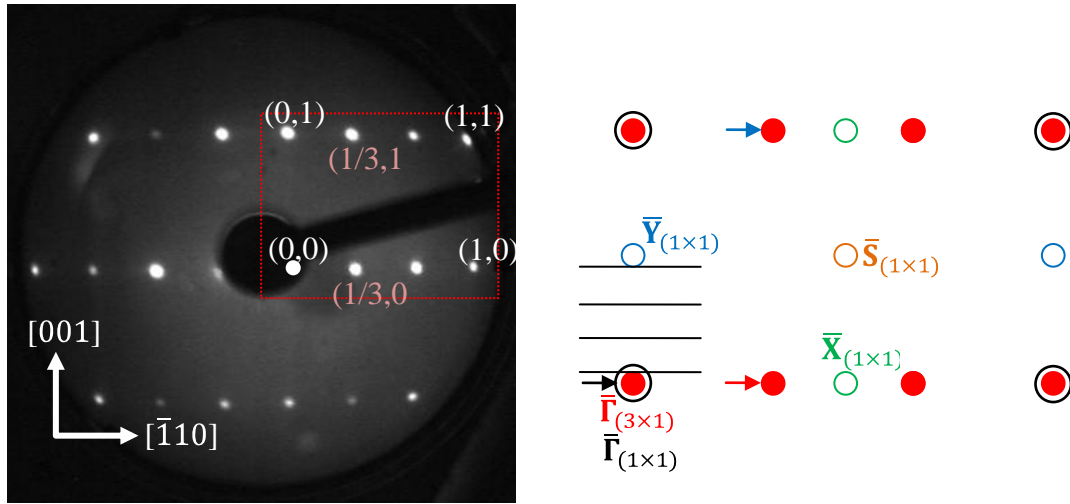


Figure 5.19 Left: LEED pattern of the Br/Pt(110)- (3×1) phase. Right: Illustration showing important symmetry points of the (1×1) and (3×1) structure. The arrows are indicating three equivalents $\bar{\Gamma}_{(3 \times 1)}$ points of interest for the discussion in the text. Black lines denotes k_{\parallel} directions shown in Figure 5.19.

The $\bar{\Gamma}_{(3 \times 1)}$ point along $\bar{\Gamma}\bar{X}_{(1 \times 1)}$ direction at a value of $k_{\parallel}=0.75 \text{ \AA}^{-1}$ (marked with a red arrow in the right side of Figure 5.19) is staying in a k_{\parallel} region where the bulk Pt d-band also crosses the Fermi level, as it was shown in the previous subchapter in Figure 5.6. In the right side of Figure 5.18, this band is represented with a black dashed line. The fact that the bulk Pt d band is at close value of k_{\parallel} of 0.75 \AA^{-1} can explain why in this k_{\parallel} region the bands are staying in a rather high and diffuse background for the (3×1) structure, leaving space for unclear interpretations. From the point of view of the

electronic structure of the (3×1) phase, the other two $\bar{\Gamma}_{(3 \times 1)}$ points at $k_{\parallel}=0 \text{ \AA}^{-1}$ and $k_{\parallel}=1.5 \text{ \AA}^{-1}$ are equivalent with the one at $k_{\parallel}=0.75 \text{ \AA}^{-1}$. A significant difference is that the bands can be clearly distinguished at the $\bar{\Gamma}_{(3 \times 1)}$ point at $k_{\parallel}=0 \text{ \AA}^{-1}$ (normal emission, marked with a black arrow in the right side of Figure 5.19). What can be clearly observed at the $\bar{\Gamma}_{(3 \times 1)}$ point at $k_{\parallel}=0 \text{ \AA}^{-1}$ is the fact that there are two folded bands exposing a gap that is not at the Fermi level. The same can be observed at the $\bar{\Gamma}_{(3 \times 1)}$ point at a $k_{\parallel}=1.5 \text{ \AA}^{-1}$ in Figure 5.18 but with less clarity. In the left side of Figure 5.18, the bands that are observed with clarity have been drawn with a bold green line. Simply translating those lines in the $\bar{\Gamma}_{(3 \times 1)}$ point at $k_{\parallel}=0.75 \text{ \AA}^{-1}$, one can understand the experimental features as a band gap opening, but not at the Fermi level (drawn with thin green lines in the right side of Figure 5.18 at a $k_{\parallel}=0.75 \text{ \AA}^{-1}$).

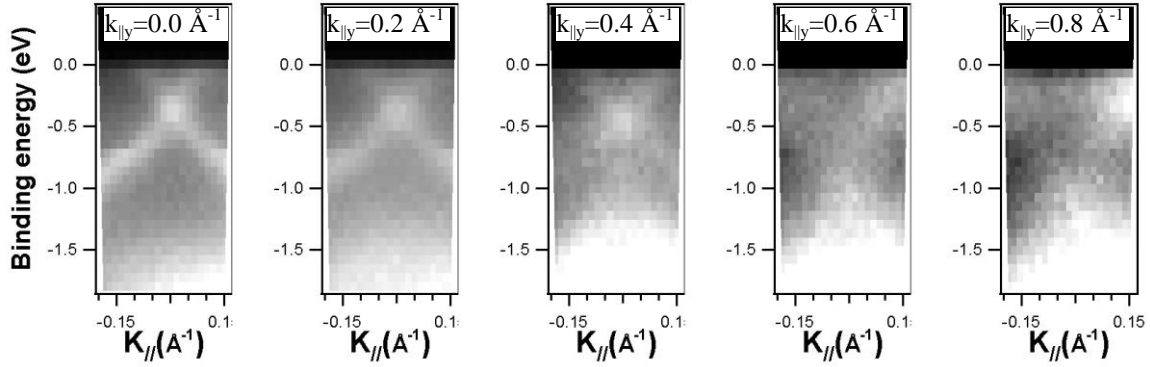


Figure 5.20 Band dispersion of Br/Pt(110)- (3×1) phase along k_{\parallel} directions parallel with $\bar{\Gamma}\bar{X}$ direction. The value of the k_{\perp} is marked on top of each scan.

The clearer situation of the new bands observed for the (3×1) structure comes from the EDC spectra for normal emission. The evolution of the bands along k_{\parallel} directions different from high symmetry directions can be understood by scanning k_{\parallel} directions parallel with $\bar{\Gamma}\bar{X}$ direction, starting from the $\bar{\Gamma}_{(3 \times 1)}$ point at $k_{\parallel}=0 \text{ \AA}^{-1}$ (marked with black lines in Figure 5.19). The result of these measurements is shown in Figure 5.20. As it can be observed, the evolution of the scans is showing that the gap never reaches the Fermi level, moreover, the binding energy value goes from -0.35 eV at a $k_{\perp}=0 \text{ \AA}^{-1}$ to a value of -0.7 eV at a $k_{\perp}=0.56 \text{ \AA}^{-1}$, never exposing the gap at the Fermi level. Another clarifying measurement to decide whether the observed bandgap is at the Fermi level is given by constant energy surfaces measurements.

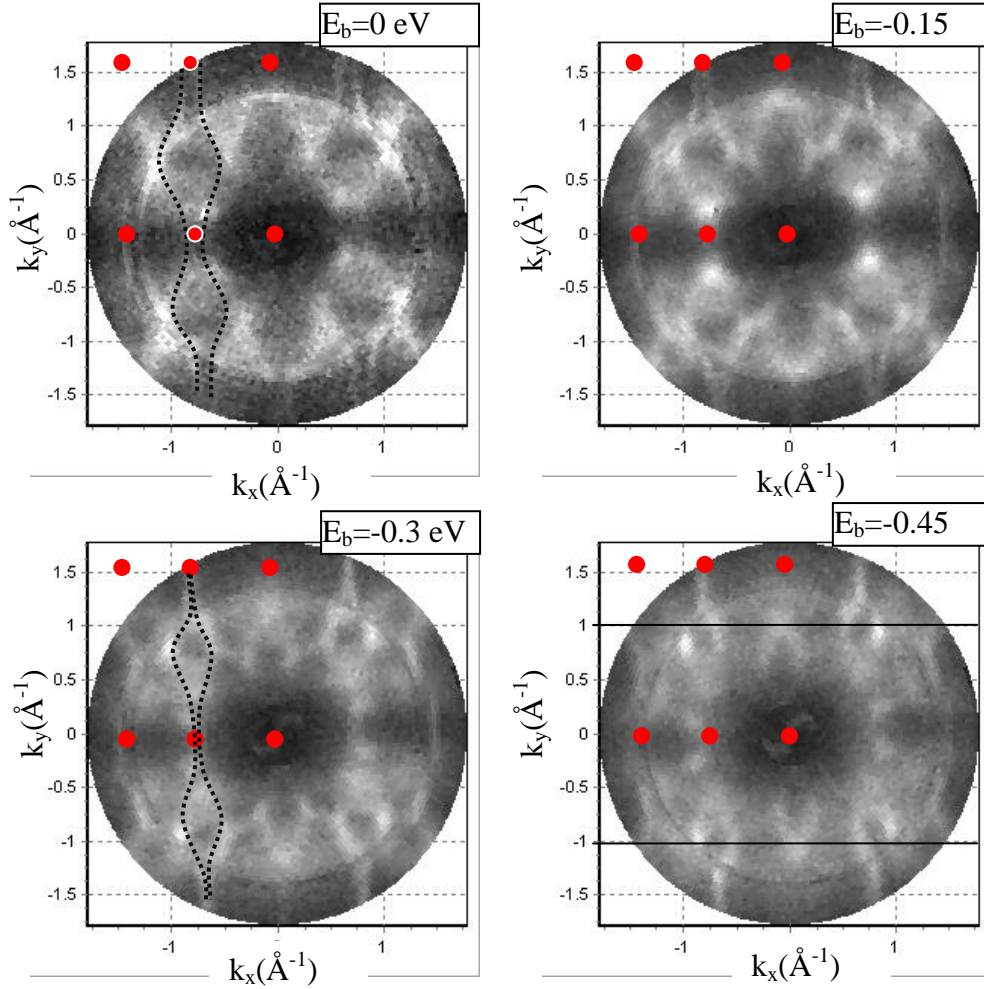


Figure 5.21 Constant energy maps of the Br/Pt(110)-(3×1) phase. The constant binding energy value is displayed for each subfigure. The red points are the $\bar{\Gamma}_{(3\times 1)}$ symmetry points.

The constant energy maps shown in Figure 5.21 present a high degree of complexity. At a first sight, an apparent $\times 3$ symmetry is observed along $[\bar{1}10]$ direction (k_x in Figure 5.21). By carefully looking at the map at $E_B = -0.45$ eV, one can see that the ellipses along the $\bar{\Gamma}\bar{Y}_{(1\times 1)}$ line are not intersected at the same position as the ellipses from the $\bar{X}\bar{S}_{(1\times 1)}$ line. Another important observation is that along the $\bar{\Gamma}\bar{X}$ line at the Fermi level a $k_{\parallel y} = 1.6 \text{ \AA}^{-1}$, a sharp state marked with a black dashed line is much better defined than the same state along the $\bar{\Gamma}\bar{X}$ direction at $k_{\parallel y} = 0 \text{ \AA}^{-1}$. When decreasing the binding energy value, it can be seen that the marked contour collapses at $E_b = -0.3$ eV into ellipses. The two $\bar{\Gamma}_{(3\times 1)}$ points enclosed by the black dashed contour are equivalent, but the energy map close to the one with $k_{\parallel y} = 1.6 \text{ \AA}^{-1}$ is much better contrasted. This agrees with the fact that at each $\bar{\Gamma}_{(3\times 1)}$ point the electronic structure presents a parabolic band crossing the Fermi level. From the dispersion curves showed in Figure 5.18 and Figure 5.20 it

can be stated that a second folded reverse parabolic band exists below the crossing parabolic state. At the intersection of these two states a gap opens, but this gap is not at the Fermi level as suggested in ref. [p1]. The fact that the open gap is not at the Fermi level agrees with the last hypothesis that the (3×1) phase of Br/Pt(110) at a coverage of 0.66 ML is not a CDW of the $c(2\times 2)$ structure (66).

5.4. Conclusions

The experimental electronic structure of the (110) face of Pt agrees satisfactory with the existing theoretical models. The dispersion of the band number 6 (sp-band) and band number 5 (d-band) of the tight binding model can be clearly observed in the constant energy maps and band dispersion measurements. A lower experimental binding energy value of the d bands compared with a tight binding model indicates a better agreement of Pt band calculations when including relativistic effects. A rather diffuse band has been observed for the Pt(110)- (1×2) clean surface measuring with a He discharge lamp at the \bar{X} point. This state is clearly visible using synchrotron polarized radiation and it has a maximum cross section at a photon energy of 20 eV. This state is not dispersing with the photon energy. An exhaustive mapping of this state in the k-space is excluding the possibility that this state is a bulk state. The facts that this state follows the (1×2) periodicity and it is surface quality sensitive are leading to the conclusion that the observed state is a surface state. The saddle point behaviour of this state in the \bar{X} and \bar{S} symmetry points indicates that possibly it is contributing to the surface stability of the (1×2) structure. The electronic structure of the Br/Pt(110)- (3×1) structure indicates an opening of a gap of the bands but not at the Fermi level. This fact agrees well with the latest hypothesis formulated about the surface properties of the Br/Pt(110) system.

Conclusiones generales

En la implementación del modelo de “tight binding”, el calculo simbólico de los elementos de matriz ha hecho posible una óptima implementación, fuera de cualquier error posible. El nuevo algoritmo desarrollado para el cálculo de superficies de energía constante, basado en algunas particularidades de la estructura electrónica, ha resultado ser 3 millones de veces más rápido que los existentes previamente. Esa velocidad se debe también al uso de fundamentos de simetría y de librerías de diagonalización de matrices específicamente compiladas para los procesadores usados. Se han escrito dos programas llamadas FLAN (Fermi Level ANalyzer) y ELAN (Energy Level ANalyzer) con una interfase visual muy intuitiva. FLAN ha sido pensado para calcular cortes de energía constante para diferentes valores de energía de fotón y también para el cálculo de proyección de bandas de volumen partiendo de superficies de Fermi precalculadas. ELAN se ha escrito para el cálculo de superficies de energía constante de cualquier valor. Además, incluye la posibilidad de calcular la dispersión y proyección de bandas a lo largo de cualquier dirección del momento paralelo a la superficie, y también de simular el proceso de fotoemisión teniendo en cuenta aproximaciones simples del estado inicial y final. Para la obtención de los mapas de proyección, se ha hecho uso del poder de calculo de la tarjeta grafica del ordenador, optimizando al máximo el tiempo en que se consiguen. Se presentan además dos algoritmos nuevos para obtener isosuperficies.

En el sistema Pb/Cu(001) se ha identificado un estado que aparece en el gap del punto M de superficie. El comportamiento de este estado al largo de la dirección GM de superficie al incrementar el recubrimiento se explica como un llenado progresivo de esta banda de superficie. Se ha observado un doblado de este estado para dos de las estructuras observadas, debido a la existencias de puntos de simetría de estas estructuras a lo largo de la dirección GM de superficie. En el caso de la estructura $c(4 \times 4)$, se observa una gran variedad de estados en el gap del punto M de superficie, que se pueden explicar teniendo en cuenta el carácter tipo electrones libres del estado . En otras direcciones de simetría para la estructura $c(4 \times 4)$, se ha observado un gap al nivel de Fermi que probablemente interviene en la estabilidad de la estructura. Finalmente, los datos de fotoemisión angular establecen que la estructura electrónica desempeña un papel importante en la estabilización de la fase de estructura $c(5\sqrt{2} \times \sqrt{2})R45^\circ$.

La estructura electrónica experimental de la cara (110) del Pt muestra un acuerdo satisfactorio con los modelos teóricos. Para las bandas de tipo d, los modelos teóricos que tienen en cuenta efectos relativistas se ajustan mejor los datos de

fotoemisión resuelta en ángulo. Se han presentado tres argumentos en favor de que un nuevo estado alrededor del punto X de superficie sea un estado de superficie. Los nuevos datos de la estructura electrónica del sistema Br/Pt(110) indican la apertura de un gap, pero en el nivel de Fermi como se había postulado. Este hecho está de acuerdo con las últimas hipótesis formuladas sobre la naturaleza de este sistema.

Bibliography

1. *Photoemission spectroscopy - from early days to recent applications*. **Friedrich Reinert, Stefan Huefner**. 2005, New Journal of Physics, Vol. 7, p. 97.
2. *Angle-Resolved Photoemission as a Tool for the Study of Surfaces*. **E. W. Plummer, W. Eberhardt**. 1982, Advances in Chemical Physics, Vol. 49, p. 533.
3. **G. V. Hansson, R. I. G. Uhrberg**. *Angle-Resolved Photoemission. Theory and Current Applications*. [ed.] S. D. Kevan. Amsterdam : Elsevier, 1992.
4. **Pendry, J. B.** *Photoemission and the electronic properties of surfaces*. [ed.] B. Fitton, R. F. Willis B. Feuerbacher. New York : Wiley, 1978.
5. *Angle-resolved photoemission studies of the cuprate superconductors*. **Damascelli Andrea, Hussain Zahid, Shen Zhi-Xun** . 2003, Rev. Mod. Phys., Vols. 75, No. 2, pp. 473-541.
6. *Surface magnetism of Gd(0001) films: Evidence for an unexpected phase transition*. **Vescovo E., Carbone C., Rader O.** . 1993, Phys. Rev. B, Vols. 48, No. 10, pp. 7731-7734.
7. **Thiry, P.** thesis. Paris : Université de Paris-Sud.
8. **Ashcroft N.W., Mermin N.D.** *Solid State Phys.* 1988.
9. *Photoemission spectra and band structures of d-band metals. VIII. Normal emission from Cu(111)*. **Smith N. V., Benbow R. L., Hurych Z.** . 1980, Phys. Rev. B, Vols. 21, No. 10, pp. 4331-4336.
10. *Angular Dependence of X-Ray-Photoemitted Valence-Electron Spectra from Single-Crystal Gold*. **Baird R. J., Wagner L. F., Fadley C. S.** 1976, Phys. Rev. Lett., Vols. 37, No. 2, pp. 111-114.
11. *A simple controllable source for dosing molecular halogens in UHV*. **Spencer ND, Goddard PJ, Davies PW, Kitson M., Lambert RM.** 1983, Journal of Vacuum Science and Technology A: Vacuum Surfaces and Films, Vol. 1, p. 1554.
12. *Tight-Binding parameters for the Elements*. **Michael J. Mehl Dimitrios A. Papaconstantopoulos**. <http://cst-www.nrl.navy.mil/bind/>.
13. *Simplified LCAO Method for the Periodic Potential Problem*. **Slater J. C., Koster G. F.** 1954, Phys. Rev., Vols. 94, No. 6, pp. 1498-1524.
14. *Tight-binding parametrization of first-principles results*. **M. Mehl, D. Papaconstantopoulos**. 1998, Topics in Computational Materials Science Ch. V, pp. 169-213.
15. *The Slater-Koster tight-binding method: a computationally efficient and accurate approach*. **D A Papaconstantopoulos, M J Mehl**. 2003, Journal of Physics: Condensed Matter, Vols. 15, No. 10, pp. R413-R440.
16. *Näherungsmethode zur Lösung des quantenmechanischen Mehrkörperproblems*. **Fock, V.** 1930, Zeitschrift für Physik A Hadrons and Nuclei, Vols. 61, No. 1, p. 126.
17. *Electronic Structure of the 3d Transition-Metal Monoxides. I. Energy-Band Results*. **Mattheiss L. F.** 1972, Phys. Rev. B, Vols. 5, No. 2, pp. 290-306.
18. **Papaconstantopoulos, Dimitrios A.** *Handbook of the Band Structure of Elemental Solids*. s.l. : Plenum Press , 1986.

19. *General expressions for reducing the Slater-Koster linear combination of atomic orbitals integrals to the two-center approximation.* **Sharma R. R.** 1979, Phys. Rev. B, Vols. 19, No. 6, pp. 2813-2823.
20. **Wolfram Research, Inc.** *Mathematica Edition: Version 5.2.* Champaign, Illinois : Wolfram Research, Inc., 2005.
21. *Energy Band Structure of Copper.* **Burdick Glenn A.** 1963, Phys. Rev., Vols. 129, No. 1, pp. 138-150.
22. *A database of fermi surface in virtual reality modeling language (vrml).* **T.-S. Choy J. Naset J. Chen S. Hershfield, C. Stanton.** 2000, Bulletin of The American Physical Society, Vols. 45, No. 1, p. L36 42.
23. **Intel.** *Intel® Math Kernel Library (Intel® MKL).*
24. *Marching Cubes: A High Resolution 3D Surface Construction Algorithm.* **Computer Graphics. Lorensen, William and Harvey E. Cline.** SIGGRAPH 87 Proceedings. Vols. 21, No. 4, p. 163.
25. **Vaisman, Izu.** *Analytical geometry.* s.l. : World Scientific, 1997.
26. *A Novel Direct Method of Fermi Surface Determination Using Constant Initial Energy Angle-Scanned Photoemission Spectroscopy.* **Lindroos M., Bansil A. .** 1996, Phys. Rev. Lett., Vols. 77, No. 14, pp. 2985-2988.
27. **Borland.** *Delphi® 2007 for Win32®.*
28. **Software, Steema.** *TeeChart for Delphi 2007.*
29. **Davletov, Khamza.** *TOGDraw component for OpenGL.*
30. **Inc., Silicon Graphics.** *OpenGL.*
31. **E. Bauer, in: V. Schommers, P. von Blanckenhagen.** *Structure and Dynamics of Surfaces II.* Berlin : Springer, 1987.
32. *Reversible structural phase transitions in semiconductor and metal/semiconductor surfaces.* **Mascaraque A., Michel E.G.** 2002, Journal of Physics Condensed Matter, Vol. 14, pp. 6005-6035.
33. *Ordered structures and phase transitions in adsorbed layers.* **Persson, B.N.J.** 1-3, 1992, Surface Science Reports, Vol. 15, pp. 1-135.
34. **E. Tosatti, E. Bertel, M. Donath.** *Electronic Surface and Interface States on Metallic Systems.* Singapore : World Scientific, 1995.
35. *Instability and Charge Density Wave of Metallic Quantum Chains on a Silicon Surface.* **Yeom H. W., Takeda S., Rotenberg E., Matsuda I., Horikoshi K., Schaefer J., Lee C. M., Kevan S. D., Ohta T., Nagao T., Hasegawa S. .** 1999, Phys. Rev. Lett., Vols. 82, No. 24, pp. 4898-4901.
36. *Charge-Density Waves in Self-Assembled Halogen-Bridged Metal Chains.* **Swamy K., Menzel A., Beer R., Bertel E. .** 2001, Phys. Rev. Lett., Vols. 86, No. 7, pp. 1299-1302.
37. *Fermi Gap Stabilization of an Incommensurate Two-Dimensional Superstructure.* **F. Schiller, J. Cordon, D. Vyalikh, A. Rubio, J. E. Ortega.** 2005, Physical Review Letters, Vols. 94, No. 1, p. 016103.
38. **Gruner, G.** *Density Waves in Solids.* Reading,MA,USA : Addison-Wesley, 1994.
39. *Leed studies of the first stages of deposition and melting of.* **Henrion J., Rhead G. E.** 1972, Surface Science, Vols. 29, No. 1, pp. 20-36.
40. *LEED studies of lead on copper (100).* **Hoesler W., Moritz W.** 1982, Surface Science, Vols. 117, No. 1-3, pp. 196-203.
41. *Influence of the scattering potential model on low energy.* **Hosler W., Moritz W., Tamura E., Feder R.** 1986, Surface Science, Vols. 171, No. 1, pp. 55-68.
42. *LEED analysis of a dense lead monolayer on copper (100).* **Hosler W., Moritz W.** 1986, Surface Science, Vols. 175, No. 1, pp. 63-77.

43. *Structure and melting of lead overlayers on Cu(100) studied with thermal-energy atom scattering.* **Sánchez Alejandro, Ferrer Salvador.** 1989, Phys. Rev. B, Vols. 39, No. 9, pp. 5778-5786.
44. *Growth and structural characterization of a lead overlayer on Cu(100).* **Wei Li, J.-S. Lin, M. Karimi, G. Vidali.** 1991, Journal of Vacuum Science and Technology A: Vacuum Surfaces and Films, Vols. 9, No. 3, pp. 1707-1711.
45. *Surfactant-Induced Suppression of Twin Formation During Growth of fcc Co/Cu Superlattices on Cu(111).* **Camarero J., Spendeler L., Schmidt G., Heinz K., de Miguel J. J., Miranda R. .** 1994, Phys. Rev. Lett., Vols. 73, No. 18, pp. 2448-2451.
46. *A channeling study of lead submonolayers deposited onto Cu(100).* **Robert S., Cohen C., L'Hoir A., Moulin J., Schmaus.** 1996, Surface Science, Vols. 365, No. 2, pp. 285-296.
47. *Surface alloying and superstructures of Pb on Cu(100).* **Nagl C., Platzgummer E., Haller O., Schmid M., Varga.** 1995, Surface Science, Vols. 331-333, No. Part 1, pp. 831-837.
48. *An STM study of the adsorption of Pb on Cu(100): formation of an ordered surface alloy.* **Robert S., Gauthier S., Bocquet F., Rousset S., Duvault.** 1996, Surface Science, Vols. 350, No. 1-3, pp. 136-144.
49. *Surface morphology changes during Pb deposition on Cu(1 0 0):.* **Plass R., Kellogg G. L.** 2000, Surface Science, Vols. 470, No. 1-2, pp. 106-120.
50. *Mesoscopic scale observations of surface alloying, surface phase transitions, domain coarsening, and 3d island growth.* **Kellogg G. L., Plass R.** 2000, Surface Review and Letters, Vols. 7, No. 5-6, pp. 649-655.
51. *Fermi Surface Nesting and Structural Transition on a Metal Surface: In/Cu(001).* **Nakagawa T., Boishin G. I., Fujioka H., Yeom H. W., Matsuda I., Takagi N., Nishijima M., Aruga T. .** 2001, Phys. Rev. Lett., Vols. 86, No. 5, pp. 854-857.
52. *Evolution of geometric and electronic structure in ultrathin In films on Cu(001).* **Nakagawa T., Mitsushima S., Okuyama H., Nishijima M., Aruga T. .** 2002, Phys. Rev. B, Vols. 66, No. 8, p. 085402.
53. *Dual nature of a charge-density-wave transition on In/Cu(001).* **Nakagawa T., Okuyama H., Nishijima M., Aruga T., Yeom H. W., Rotenberg E., Krenzer B., Kevan S. D.** 2003, Phys. Rev. B, Vols. 67, No. 24, p. 241401.
54. *Fermi surface gapping and nesting in the surface phase transition of Sn/Cu(100).* **J. Martinez-Blanco, V. Joco, H. Ascolani, A. Tejeda, C. Quiros, G. Panaccione, T. Balasubramanian, P. Segovia, E. G. Michel.** 2005, Physical Review B (Condensed Matter and Materials Physics), Vols. 72, No. 4, p. 041401.
55. *Surface Peierls transition on Cu(001) covered with heavier p-block metals.* **Tetsuya, Aruga.** 2006, Surface Science Reports, Vols. 61, No. 6, pp. 283-302.
56. *First-principles identification of quasi-two-dimensional Fermi surface nesting on a metallic c(2x2)-In/Cu(001) surface.* **Gao Xing, Zhou Yu-mei, Wu Si-cheng, Wang Ding-sheng.** 2002, Phys. Rev. B, Vols. 66, No. 7, p. 073405.
57. *Surface phase transition and electronic structure of c(5√2x√2).* **Joco V., Martinez-Blanco J., Segovia P., Balasubramanian.** 2006, Surface Science, Vols. 600, No. 18, pp. 3851-3855.
58. *Halogen adsorption on solid surfaces.* **Jones Robert G.** 1988, Progress in Surface Science, Vols. 27, No. 1-2, pp. 25-160.
59. *Halogen-metal interaction: bromine on Pt(110).* **Swamy Krishna, Hanesch Paul, Sandl Peter, Bertel Erminald.** 2000, Surface Science, Vols. 466, No. 1-3, pp. 11-29.

60. *Evidence for a Peierls Distortion or a Kohn Anomaly in One-Dimensional Conductors of the Type $K_2Pt(CN)_4Br_{0.30} \cdot xH_2O$* . **Comes R., Lambert M., Launois H., Zeller H. R.** 1973, Phys. Rev. B, Vols. 8, No. 2, pp. 571-575.
61. *(3×1) -Br/Pt(110) structure and the charge-density-wave-assisted $c(2 \times 2)$ to (3×1) phase transition.* **C. Deisl, K. Swamy, N. Memmel, E. Bertel, C. Franchini, G. Schneider, J. Redinger, S. Walter, L. Hammer, K. Heinz.** 2004, Physical Review B (Condensed Matter and Materials Physics), Vols. 69, No. 19, p. 195405.
62. *Charge-Density Waves in Self-Assembled Halogen-Bridged Metal Chains.* **Swamy K., Menzel A., Beer R., Bertel E.** 2001, Phys. Rev. Lett., Vols. 86, No. 7, pp. 1299-1302.
63. *Correlation in low-dimensional electronic states on metal surfaces.* **A Menzel, Zh Zhang, M Minca, Th Loerting, C Deisl, E Bertel.** 2005, New Journal of Physics, Vol. 7, p. 102.
64. *The Pt(110) surface studied by STM and RHEED.* **Kuntze J., Huck M., Rauch T., Bomermann J., Speller.** 1996, Surface Science, Vols. 355, No. 1-3, pp. L300-L304.
65. *Band structure of platinum from angle resolved photoemission experiments.* **Leschik G., Courths R., Wern H., Hufner S., Eckardt.** 1984, Solid State Communications, Vols. 52, No. 2, pp. 221-225.
66. *Fluctuations and Phase Separation in a Quasi-One-Dimensional System.* **Enrico Dona, Thomas Loerting, Simon Penner, Mariana Minca, Alexander Menzel, Erminald Bertel, Johannes Schoiswohl, Steven Berkebile, Falko P. Netzer, Rinaldo Zucca, Josef Redinger.** 2007, Physical Review Letters, Vols. 98, No. 18, p. 186101.
67. *Temperature dependence of the charge-density-wave energy gap on In/Cu(001).* **S. Hatta, H. Okuyama, M. Nishijima, T. Aruga.** 2005, Physical Review B (Condensed Matter and Materials Physics), Vols. 71, No. 4, p. 041401.